博士論文

Exploration of novel quantum transport phenomena in magnetic Dirac materials with Bi square net

(ビスマス正方格子をもつ磁性ディラック電子系における新奇な量子輸送現象の開拓)

増田 英俊

Contents

Chapter 1

Introduction

1.1 Preface

Magnetic conductors show variety of unique and versatile magnetotransport phenomena. The ferromagnet / metal / ferromagnet tunnel junction system shows a giant magnetoresistive effect (GMR), in which the resistance greatly modulated by controlling the magnetic structure by an external magnetic field at room temperature. In ferromagnetic metals, spin-polarized conduction electrons undergo spin-dependent scattering, arising the anomalous Hall effect. Colossal magnetoresistance (CMR) effects are observed in strongly correlated Mn oxides, in which the resistivity is tuned by several orders of magnitude due to the metal-insulator transition induced by an external magnetic field. These phenomena have been one of the major subject in the field of condensed matter physics for many years. Furthermore, these phenomena are applied to magnetic memory devices, arising the field of spintronics.

Dirac materials, on the other hand, are of particular interest in recent years. The discovery of the half-integer quantum Hall effect in graphene in 2005 triggered the research on variety of Dirac materials. Now variety of materials, such as topological insulator surface states, an organic conductor and 3-dimensional Dirac semimetals, are discovered and intensively studied both theoretically and experimentally. Dirac materials have linear energy-momentum dispersion relations near the Fermi level and the conducting carriers can be regarded as a relativistic particle of mass zero. Backscattering of carriers is suppressed by the coupling of the momentum and (pseudo-)spin, leading to exceptionally high mobilities. Furthermore, peculiar magnetic transport phenomena such as half-integer quantum Hall effect and giant linear magnetoresistance are observed due to the nontrivial Berry phase contribution and the unique Landau level structures in the magnetic field. The mechanisms of these phenomena and the topological nature of the electronic structure are of interest from the viewpoint of basic physics. Furthermore, applications to high-speed/energy-saving devices and spintronic devices are expected utilizing the high mobility and peculiar magnetotransport phenomena.

In this way, both the magnetic conductors and the Dirac materials show unique

and versatile magnetotransport phenomena. Therefore the magnetic Dirac materials which host both magnetic orders and Dirac fermions are expected to show even more interesting magnetotransport phenomena. In this point of view, magnetic topological insulators are extensively studied, leading to the observation of the quantized anomalous Hall effect. More recently, Weyl semimetal phases with magnetic orders are discovered, exemplified by Mn_3Sn and pyrochlore-type iridium oxides showing peculiar magnetotransport properties such as the anomalous and topological Hall effects. Furthermore, Field-induced Weyl phases are also sought in semimetals/semiconductors with local magnetic moments such as GdPtBi and $EuTiO_3$. However, only few materials are identified as magnetic Dirac materials, mainly due to the difficulty in material development. Since the Dirac electronic structures strongly depend on the symmetry of crystals in many systems, Dirac fermions are lost, especially in bulk crystals, by chemical substitutions to magnetic elements. Also, the carrier mobility of the magnetic Dirac materials known to date are relatively low compared to those of nonmagnetic Dirac materials. Since the high carrier mobility is one of the most important feature of Dirac materials, magnetic Dirac materials with a high carrier mobility is desired.

From this point of view, we focused on the multilayered Dirac materials with Bi square net. These systems has a layered crystal structure consists of an alternate stack of a conduction layer of Bi square net hosting two-dimensional Dirac fermion and a magnetic insulating layer hosting magnetic elements. Since quasi-two-dimensional Dirac fermions are arising from the Bi square net, we can develop a variety of magnetic layers by chemical substitutions while keeping the Dirac-like band structure responsible for the high carrier mobility in these system. In $SrMnBi_2$, the prototypical Dirac materials with Bi square net, the transport of the Dirac fermion is hardly affected by the Mn magnetic order. In this study, we focused on $EuMnBi_2$ hosting magnetic $Eu^{2+}(S = 7/2)$. In this system, since the magnetic Eu site is adjacent to the Bi square net hosting Dirac fermions, the magnetic order of Eu is expected to strongly influence the conduction of the Dirac fermions. We made detailed measurements of magnetic and transport properties in this system and revealed an interesting magnetotransport phenomena in which the quantum transport of the Dirac fermions strongly coupled with the antiferromagnetic order of Eu. Furthermore, the carrier mobility of $EuMnBi_2$ reaches $\sim 14,000$ cm^2/Vs, which is outstandingly high among other magnetic Dirac materials. This research realized the novel magnetic transport phenomenon by the coupling of the magnetic order and the quantum transport of Dirac fermions for the first time in bulk compounds and furthermore shows a new guideline for realizing the magnetic Dirac electron system.

1.2 Quantum transport phenomena in Dirac materials

In this section, we overview the recent researches on the Dirac materials or Dirac fermion systems in solids.

Dirac materials

The materials group called Dirac materials includes a wide range of materials, such as graphene, Bi_2Te_3, Cd_3As_2, organic conductor $\alpha-(ET)_2I_3$, correlated metal Mn_3Sn. They share a fundamental similarity in their momentum-energy dispersion near the Fermi level and therefore exhibit a variety of interesting physical properties common to mani Dirac materials.

The transport properties of many metals and semiconductors are governed by electron carriers formed at the bottom of the conduction band and hole carriers formed near the top of the valence band. If the energy dispersion near the Fermi level is approximated as $E_n(\boldsymbol{k}) \simeq E_c + \frac{\hbar^2}{2m^*}\boldsymbol{k}^2$, the motion of the carrier behave as a free particle obeying the Schrödinger equation with a mass of m^*.

In the Dirac materials, on the other hand, the band structure near the Fermi level show a linear energy-momentum dispersion as shown in Fig. 1.1(c), which is approximated as $E = \hbar v_F |\boldsymbol{k}|$. In this case, the conducting carriers obey the Dirac equation for the zero-mass particle, whose Hamiltonian is given as

$$H_D = \begin{pmatrix} mc^2 I & c\boldsymbol{\sigma}\cdot\boldsymbol{p} \\ c\boldsymbol{\sigma}\cdot\boldsymbol{p} & -mc^2 I \end{pmatrix} \tag{1.1}$$

, where $\boldsymbol{\sigma}$ is the Pauli matrices and I is the unit matrix. Therefore in the Dirac materials, conducting carriers are regarded as zero-mass relativistic particles obeying the Dirac equation with the Fermi velocity v_F in the place of the speed of light c.

graphene

Graphene is the most common and simple, ideal system among the Dirac materials. Graphene is a two-dimensional material where the carbon atoms are assembled into a honeycomb lattice as shown in Fig. 1.1. The sp^2 hybrid orbital is responsible for the bond between carbon atoms and the state near the Fermi level is derived from the remaining p_z orbital. The honeycomb lattice hosts two equivalent sublattices (denoted as A and B in Fig. 1.1[a]) in the unit cell, and correspondingly there are two equivalent points in the Brillian zone, K and K'. Taking the p_z orbitals on the sublattices A and B as the bases, the tight-binding Hamiltonian for the electrons in graphene has the form

$$H = \begin{pmatrix} 0 & -t\sum_{l=1}^{3} e^{i\boldsymbol{k}\cdot\boldsymbol{\delta}_l} \\ -t\sum_{l=1}^{3} e^{-i\boldsymbol{k}\cdot\boldsymbol{\delta}_l} & 0 \end{pmatrix} \tag{1.2}$$

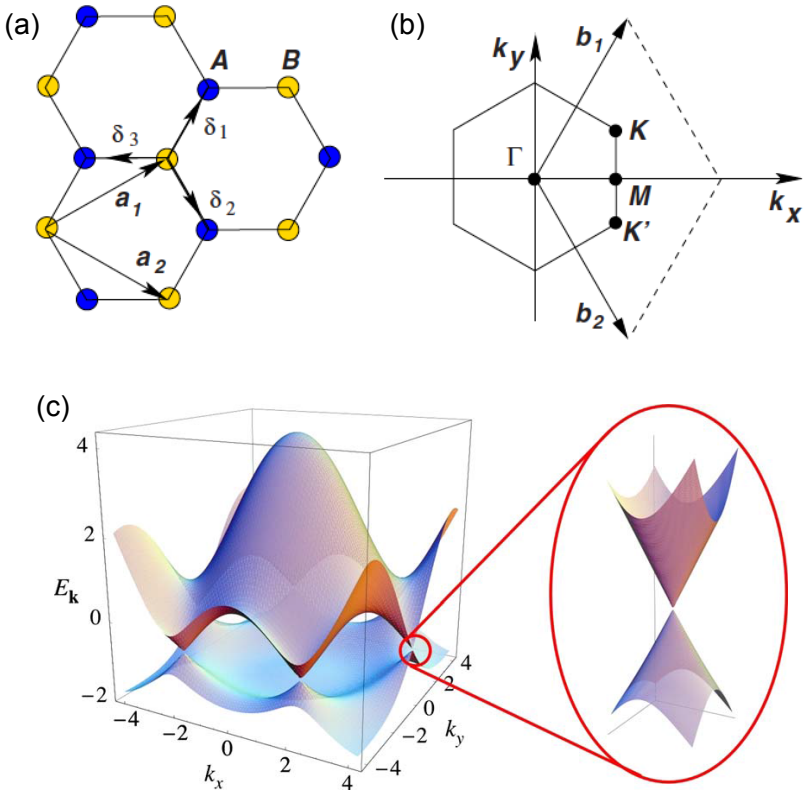

Fig. 1.1 (a) crystal structure, (b) Brillouin zone, and (c) band structure of graphene[2]. A and B denote the two sublattices in the unit cell. $\boldsymbol{a}_{1,2}$ are the unit cell vectors, $\boldsymbol{b}_{1,2}$ are the reciprocal lattice vectors and $\boldsymbol{\delta}_{1,2,3}$ are the nearest-neighbor vectors.

, where t is the nearest-neighbor hopping energy and $\delta_l (l = 1, 2, 3)$ are the nearest-neighbor vectors (Fig. 1.1[a]). The full band structure is shown in Fig. 1.1[c]), with a zoom in of the band structure near the K point. This energy dispersion and the effective Hamiltonian are obtained by expanding 1.2 close to the K point as follows:

$$E(\boldsymbol{k}) = \pm v_F \left|\boldsymbol{k}\right|, v_F = \frac{\sqrt{3}at}{2\hbar} \tag{1.3}$$

$$H = \hbar v_F \begin{pmatrix} 0 & k_x - ik_y \\ k_x + ik_y & 0 \end{pmatrix} \tag{1.4}$$

, which is equivalent to the Weyl equation in two dimension.

It should noted that the degree of freedom in Eq. 1.4 arises from the two sublattices A and B in the unit cell, rather than the spin degree of freedom in the original Weyl equation. This degree of freedom is called pseudospin. Also, the zero gap state arise from the equivalence of the two sublattices.

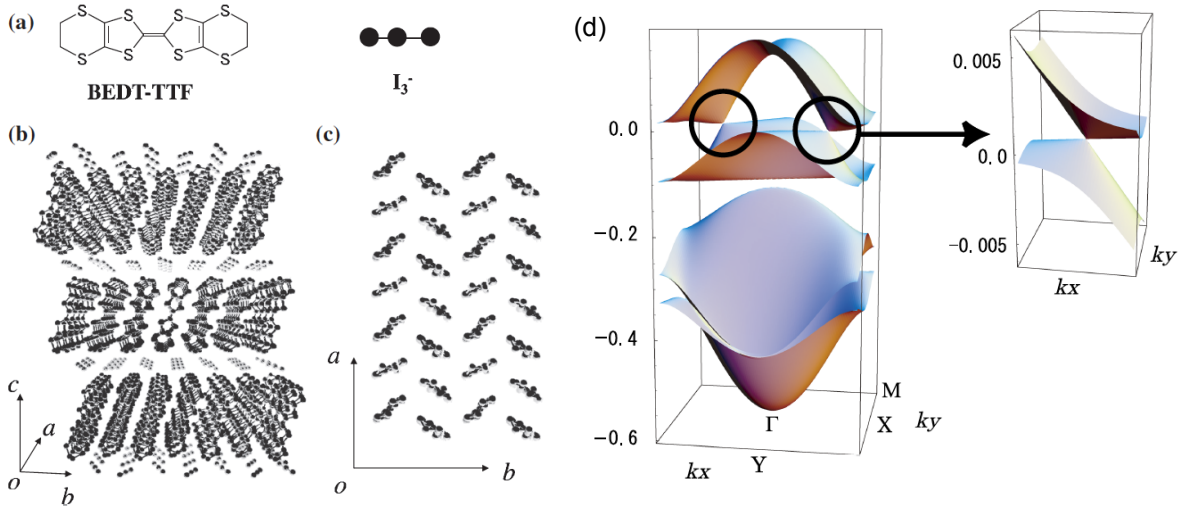

Fig. 1.2 (a) The ET molecule and the I_3^- molecule. (b) The crystal structure of $\alpha - ET_2I_3$. (c) Crystal structure of the conducting ET layer vied from the c axis. (d) Calculated band structure in the metallic phase of $\alpha - ET_2I_3$.[3]

Organic conductor $\alpha - (BEDT)_2I_3$

The organic molecular crystal $\alpha - (BEDT)_2I_3$ (abbreviated as $\alpha - ET_2I_3$ in the following) Is a layered material consisting of the conducting layers composed of ET molecules and the insulating layers composed of I_3^- molecules as shown in Fig. 1.2 (a-c).[3]. This material becomes a insulator below 135 K at ambient pressure due to the charge ordering. Under a pressure of above 1.5 GPa, the insulating phase is suppressed and the system remain metallic at all temperatures.

The band structure in the metallic phase along the in-plane direction is shown in Fig. 1.2(d), with a zoom in near the Fermi level showing a tilted Dirac cone. The Dirac energy dispersion in this system arise from an accidental closing of the gap.

In $\alpha - ET_2I_3$, the Fermi level is fairly close to the Dirac point because the natural doping of the carriers by the chemical defect is relatively small. As a result, a relatively weak magnetic field realizes the quantum limit where the Landau zero mode dominates the transport properties, arising peculiar magnetotrnsport properties as described in Sec. 1.2.

Topological insulators

The surface states of the topological insulators (TIs) are also known to host Dirac fermion state[4, 5, 6]. Topological insulators are insulating in bulk; However, as shown in Fig. 1.3(a,b), TIs host metallic surface states with Dirac-like linear energy dispersions arising from the topological nature of the bulk insulating band structure. Furthermore, the spin degeneracy is lifted in the surface Dirac state and the spin is

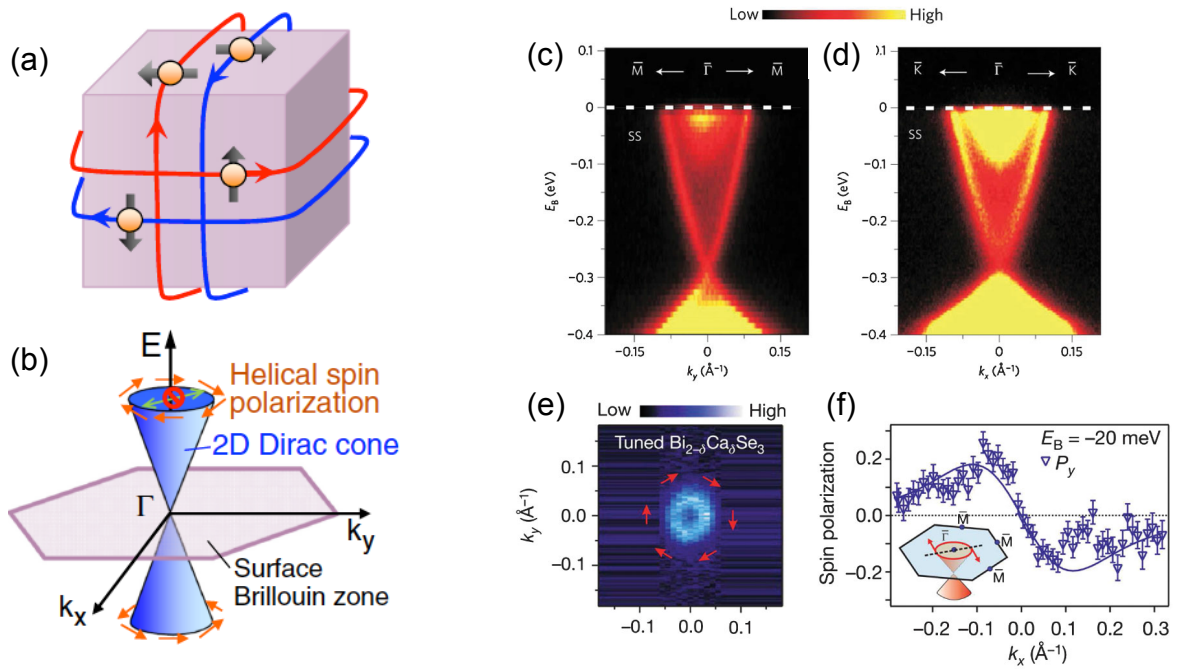

Fig. 1.3 (a) Real-space and (b) reciprocal lattice space picture of the surface Dirac state of 3-dimensional topological insulators[5]. (c-f) Surface Dirac states of a 3-dimensional topological insulator Bi_2Te_3 as probed by ARPES measurements.

locked perpendicular to the momentum (Fig. 1.3[a,b]), as is called as "helical spin polarization". This helical spin polarization suppress the back scattering, arising high mobility of the electron. Furthermore, when a current is applied to the surface state, a spin Hall effect is observed in which spin polarization appears in a direction perpendicular to the surface state, which imply the spintronic applications.

Several compounds, such as $(Bi,Sb)_2(Te,Se)_3$ and $Bi_{1-x}Sb_x$, have been experimentally identified as 3-dimensional topological insulators by ARPES measurements (Fig. 1.3c-e). Recently transport properties of the surface Dirac states, such as quantum Hall effect[7], are of particular interest. In these researches, bulk conduction is effectively suppressed by finely tuning the chemical composition of the thin film samples, enabling the surface states to dominate the transport properties.

3-dimensional Dirac semimetal

Contrary to the (quasi-) two-dimensional systems such as graphene, surface of the topological insulators and $\alpha-ET_2I_3$, several materials such as Cd_3As_2[8, 9], Na_3Bi[10, 11], Ca_3PbO[12, 13] are known to host three-dimensional Dirac fermion, where the energy-momentum dispersion is linear to all the three directions.

In Cd_3As_2, three-dimensional Dirac fermion state is realized by the band inversion mechanism explained as follows. Cd_3 As_2 crystallizes in a complex crystal structure

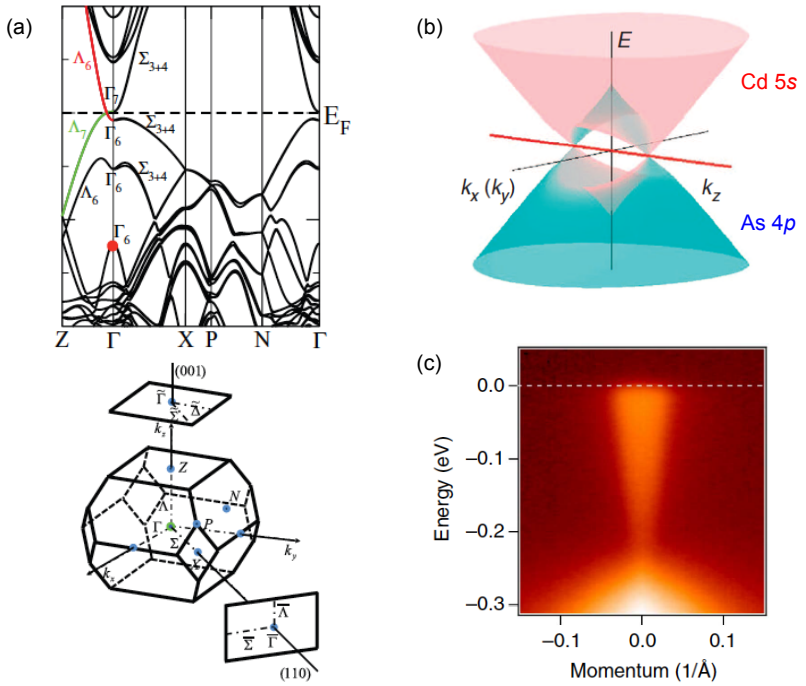

Fig. 1.4 Three-dimensional Dirac fermion state in Cd_3As_2. (a) Calculated band structure and Brillouin zone of Cd_3As_2[8]. (b) Schemetic description of the three-dimensional Dirac fermion state in Cd_3As_2[9]. Red and blue colors denote Cd $5s$ and As $4p$ characters, respectively, and the red line is the axis of the four-fold rotational symmetry. (c) Three dimensional Dirac semimetal state observed by ARPES.

with 32 atoms in a unit cell[14], which host four-fold rotational symmetry. This system can be regarded as an ionic crystal and the As $4p$ orbital and the Cd $5s$ orbital form the valence and conduction bands, respectively. However the valence and conduction are inverted around a specific point in the Brillouin zone as depicted in Fig. 1.4(a). The inverted bands are hybridized to open a gap; however, the band hybridization is prohibited and the gap is closed along the axis of the four-fold rotational symmetry. As a result, the Dirac point appears on the axis of the four-fold rotational symmetry as depicted in Fig. 1.4(a).

The band inversion mechanism similar to that in Cd_3As_2 is also responsible for the three-dimensional Dirac fermion in Na_3Bi and Ca_3PbO. However, the Dirac semimetal band in Ca_3PbO is slightly gapped by the spin-orbit coupling.

Weyl semimetal

Dirac fermions in graphene, $\alpha-ET_2I_3$ and three-dimensional Dirac semimetals are spin-degenerate. Weyl semimetals host linear energy dispersion similar to Dirac semimetals; however, the energy bands in Weyl semimetals are spin non-degenerate[1,

116]. One of the most striking features of Weyl semimetals is the topological stability of the Weyl point. The Berry flux piercing any surface enclosing the Weyl point is exactly quantized to $2\pi C$, where C is the chirality; the Weyl points behave as the source or sink of the Berry flux. As a result, Weyl points are stable and can be eliminated only by the pair annihilation.

The spin degeneracy must be lifted in Weyl semimetals. Therefore the broken space- or time-inversion symmetry is required to realize Weyl semimetals to lift up the spin degeneracy. Several Weyl semimetal phases with broken space-inversion symmetry have been predicted and discovered so for. TaAs and related compounds were predicted to be Weyl semimetals[15], and ARPES signatures of the Weyl state have been observed[16]. Recently, a few Weyl semimetals with broken time-reversal symmetry, such as Mn_3Sn and pyrochlore $R_2Ir_2O_7$, are discovered.

Transport properties of Dirac materials

Dirac materials are of particular interest mainly for their unusual transport properties, especially under magnetic field. Her, we overview the nontrivial transport phenomena in Dirac materials.

Suppression of backscattering

Many Dirac materials are reported to show exceptionally high carrier mobility. Mobility in high-quality graphene samples reach 2×10^4 cm^2/Vs; Cd_3As_2 also shows ultrahigh mobility up to 9×10^6 cm^2/Vs[17, 18]. These high mobilities make Dirac materials promising for future electronic applications.

One of the origin of the high mobility in Dirac materials is that the backscattering is suppressed in Dirac fermions. In Dirac fermion systems, the momentum is coupled to the (pseudo-)spin. Therefore back scattering of Dirac fermions require simultaneous flip of the (pseudo-)spin. Therefore backscattering by a impurity is forbidden unless the impurity potential conserves (pseudo-)spin.

Scattering probability of the Dirac fermion in graphene by a one-dimensional potential barrier have been calculated. The result shows effective suppression of the backscattering[19], leading to the ultrahigh mobility in graphene. In Cd_3As_2 the transport scattering time τ_{tr} is approximately four orders of magnitude larger than the quantum scattering time τ_Q[18], experimentally signifying the suppression of backscattering.

Landau levels

Another striking feature of the Dirac fermion is the nontrivial Landau level structure. Under a strog magnetic field, two-dimensional Dirac fermion with the energy dispersion $E = \hbar v_F |\boldsymbol{k}|$ is Landau quantized as

$$E_0 = 0, E_{\pm n} = \pm v_F \sqrt{2eB\hbar n}, n = 1, 2, 3, \ldots \tag{1.5}$$

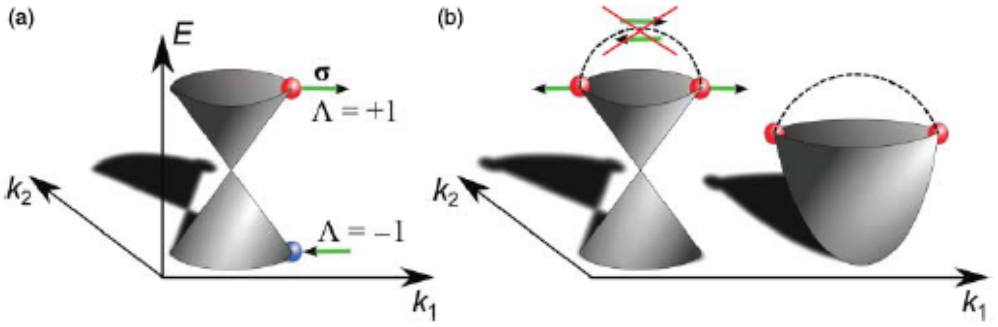

Fig. 1.5 (a) The energy-momentum dispersion of Dirac fermions showing the momentum(k)-pseudospin σ coupling. (b) Forbidden back scattering of Dirac fermions.[1]

Here, v_F is the Fermi velocity and e is the elementary charge. This Landau level has three major features:

- Landau levels are nonuniform as $E_n \propto \sqrt{n}$: Landau level spacing is larger for small n.
- Landau level spacing is proportional to $\sqrt{B}$, rather than B as in the case in normal metals. As a result, a large Landau level spacing is achieved by a relatively weak magnetic field.
- Landau zero mode appears at the Dirac point, irrespective of the magnitude of the magnetic field.

These feature are clearly observed in the quantum Hall effect in graphene shown in Fig. 1.6(a) [20, 21]. The Hall conductivity in graphene is quantized into half-integer values as $\sigma_{xy} = 4\frac{e^2}{h}\left(n + \frac{1}{2}\right)$. This unusual quantum Hall effect is the consequence of the peculiar Landau levels due to the nontrivial Berry's phase of the Dirac fermion. Furthermore, the quantum Hall effect is observed even at room temperatures as shown in Fig. 1.6(b)[22]. This is because the spacing between the $n = 0$ and $n = 1$ Landau levels is exceptionally large because $E_n \propto \sqrt{B}$.

In the quasi-two-dimensional Dirac fermion system $\alpha{-}ET_2I_3$, the Fermi level is located close to the Dirac point. Under a magnetic field, $n = \pm 1$ Landau levels rapidly leave away from the Fermi level in proportion to $\sqrt{B}$. As a result the quantum limit, where only the Landau zero mode contribute to the transport, is realized by a relatively weak magnetic field of 0.1 T. Therefore the magneto-transport properties of $\alpha{-}ET_2I_3$ is well understood in terms of the Landau zero mode. Figure 1.7 shows the magnetic field dependence of the interlayer resistance of $\alpha{-}ET_2I_3$. In the magnetic field range from 0.5 T to 3 T the interlayer resistivity is proportional to the inverse of the magnetic field ($R_{zz} \sim 1/B$). This behavior can be understood by a model in which the carriers on the conductive layer tunnel across the insulating layer.

In this model, the interlayer conductivity is proportional to the density of states

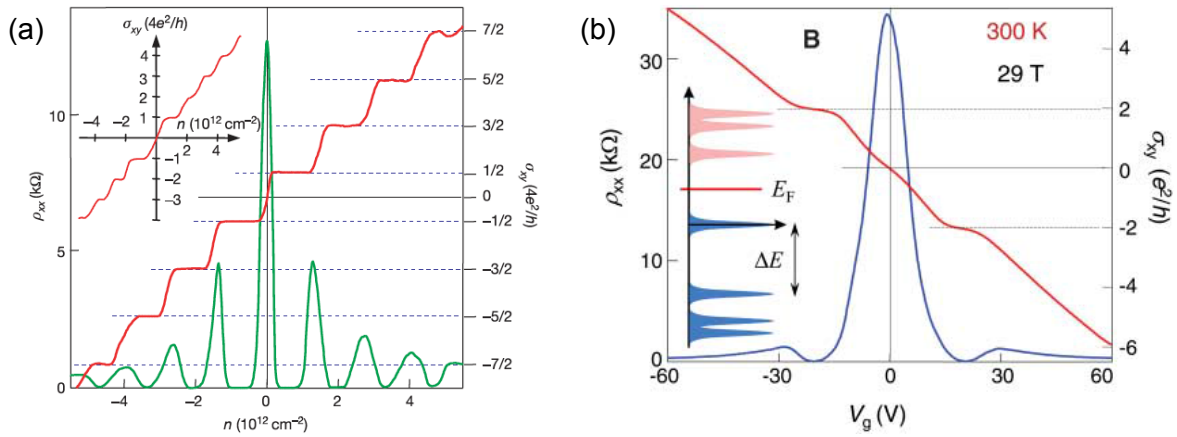

Fig. 1.6 (a) Half-integer quantum Hall effect in graphene[20]. (b) Quantum Hall effect at 300 K, 29 T[22].

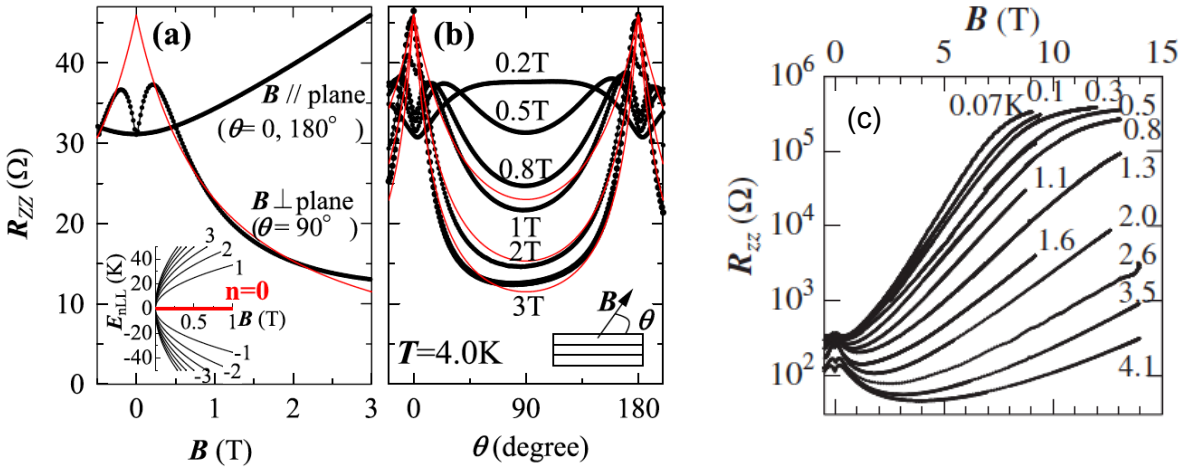

Fig. 1.7 (a) Magnetic field dependence of the interlayer resistivity R_{zz} in $\alpha-ET_2I_3$. The red line is the theoretical result by Osada[23]. (b) Angular dependence of R_{zz} for selected magnetic field. (c) Magnetic field dependence of R_{zz} at high field, low temperature regime. [3]

at the Fermi level and the tunneling probability between the layers. The tunneling probability is independent of magnetic field since the conducting direction is parallel to the magnetic field. The density of states is proportional to the degeneracy factor of the Landau zero mode and hence to the magnetic field B. Therefore it is expected that the interlayer conductivity is proportional to magnetic field ($\sigma_{zz} \propto B$) and the interlayer resistivity R_{zz} is inversely proportional to magnetic field ($\sigma_{zz} \propto 1/B$). Based on the above model, Osada[23] calculated the magnetic field/angle dependence of the interlayer resistivity and obtained results that agree well with the experimen-

tal result. At higher magnetic field, the density of states decreases due to Zeeman splitting of the zero mode and the interlayer resistivity decreases exponentially as $R_{zz} \propto 1/|B| \exp(g\mu_B B/2k_B T)$ (Fig. 1.7 c). More recently, unusual transport properties such as the giant Nernst effect is reported[24].

1.3 Magnetic Dirac materials

As mentioned in the previous sections, the Dirac fermion systems exhibits novel transport characteristics, such as suppression of back scattering and linear magnetoresistance, especially in a magnetic field. In this section, we first describe that various and interesting magnetotransport phenomena are observed in the magnetic conductors Recent studies on magnetic topological insulators and pyrochlore type iridium oxides are described from the viewpoint of exploring novel magnetic transport properties by combination of magnetic transport properties of Dirac electron system and magnetic transport characteristics of magnetic materials.

Magnetic conductors and spintronics

Since the discovery of giant magnetoresistance (GMR) phenomena, the unique magnetic conduction properties exhibited by magnetic materials have been discovered one after another and attracted attention[25, 26]. From the viewpoint of basic physics, it became clear that the degree of freedom of spin of electrons can not only give degeneracy degree 2 but also play an important role in electric conduction properties. As a result, the conduction characteristics of the system can be changed by controlling the magnetic order by the external magnetic field, and various magnetic conduction phenomena have been reported so far. From the application point of view, it is possible to electrically read the magnetic memory, and a new field called spintronics, such as the GMR element being applied to the reading head of the hard disk, was opened.

The simplest and representative example of spin-dependent conduction characteristics is the tunnel magnetoresistive effect observed in ferromagnetic / nonmagnetic insulator / ferromagnetic tunnel junction system[26]. As shown in Fig. 1.8 (a, b), it is possible to realize two ways, that the magnetization of the ferromagnetic layer sandwiching the insulator layer becomes parallel and antiparallel. In the process of electron tunneling through the insulating layer, no spin flip occurs and $\uparrow$ spin and $\downarrow$ spin are considered to shift to the same state, respectively. Spin polarization of each layer is given as $P_{1,2} = \frac{N_M - N_m}{N_M + N_m}$ using the number of electrons of major and minor spins N_M, N_m, reflecting the density of states at the Fermi level. Therefore, letting the resistances in the parallel state and antiparallel state be R_p and R_{ap}, the magnetoresistive ratio is

$$\frac{R_{ap} - R_p}{R_p} = \frac{2P_1 P_2}{1 - P_1 P_2} \tag{1.6}$$

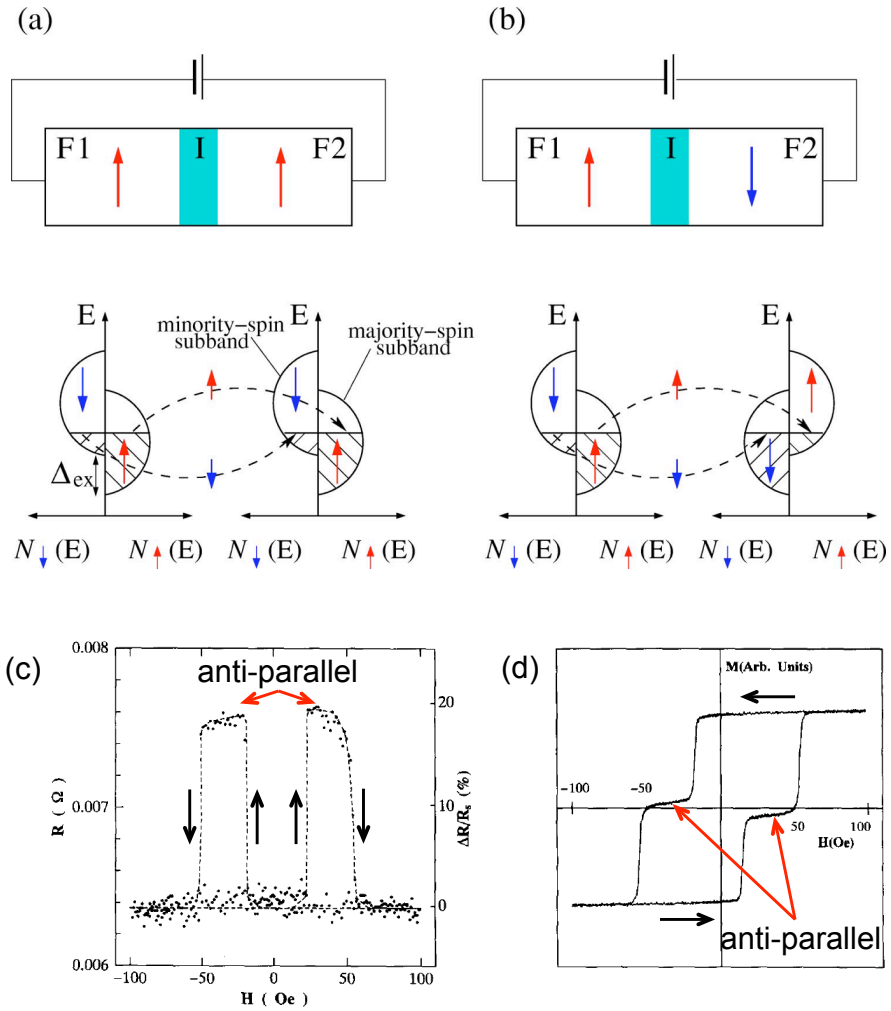

Fig. 1.8 Schematic diagrams of ferromagnet / insulator / ferromagnet tunnel junction and the density of states in (a) parallel state and (b) antiparallel states[26]. (c) Tunneling magnetoresistance curve and (d) magnetization curve of $Fe/Al_2O_3/Fe$ junction at room temperature[27]. The region where the magnetization is close to zero corresponds to the antiparallel state, and the tunnel magnetic resistance of $\sim 20\%$ is observed. The black arrow represents a sweep direction of the magnetic field and the red arrow represents a magnetic field region where an antiparallel state is realized.

Thus TMR is an effect reflecting a phenomenon in which the number of electrons is biased due to spin in the ferromagnetic state. Experimentally, sharp changes in magnetoresistance reaching $\sim$ 20% at room temperature have been reported (Fig. 1.8 c, d). Such a unique magnetoresistance phenomenon is made possible only by using the spin degree of freedom of a ferromagnetic material, and is representative of various magnetoresistance phenomena using a magnetic conductors.

Since the discovery of TMR, many unique and versatile magnetotransport phenomena in magnetic materials have been reported. In ferromagnetic metal / paramagnetic metal / ferromagnetic metal junction system giant magnetoresistive effect (GMR) is observed at room temperature by the similar principle as in TMR. This phenomenon is a typical example of spin-dependent conduction and applied to a reading head of a magnetic memory, arising a new field called spintronics[25]. Anomalous Hall effects in ferromagnets are old phenomena known for over 100 years. However the mechanism of the Anomalous Hall effects have been extensively studied until quite recently[28]. Some strongly correlated Mn oxides exhibit colossal magnetoresistance effect (CMR) in which the resistivity varies over several orders of magnitude due to the metal-insulator transition induced by an external magnetic field[29]. These examples are only a part of the peculiar magnetotransport phenomena observed in magnetic conductors.

Magnetic topological insulators

As mentioned in the previous sections, magnetic conductors exhibit variety of magnetotransport phenomena due to the magnetic order tuned by the external magnetic field. On the other hand, as mentioned in Sec. 1.2, Dirac materials themselves show peculiar magnetotransport phenomena. Therefore magnetic Dirac materials hosting both magnetic order and Dirac fermions are expected to exhibit further interesting magnetotransport phenomena. Representative of these magnetotransport phenomena is the quantized anomalous Hall effect in magnetic topological insulators.

As mentioned in Sec. 1.2, topological insulators host Dirac fermion state localized on the surface. Since this surface Dirac state originates from the topology of the bulk insulating electronic structure and is protected by the time reversal symmetry, the Dirac state is gapped when a magnetic order breaks the time reversal symmetry. Yu et al. theoretically predicted for the topological insulator (Bi, Sb)$_2$(Te, Se)$_3$ doped with transition metal elements, that this gapped state hosts quantized anomalous Hall state[30]. The doped transition metal develops ferromagnetic order by the mechanism originating from van Vleck paramagnetism and arises finite anomalous Hall conductivity even at zero magnetic field. Furthermore, the anomalous Hall conductivity is quantized due to the two-dimensional nature of the surface state Thus the quantized Hall resistance is observed even at the zero magnetic field. The predicted quantized anomalous Hall effect was experimentally observed in Cr_x(Bi, Sb)$_{2-x}$Te$_3$ (Fig. 1.9)[31, 33] and subsequently in V-doped (Bi, Sb)$_{2-x}$Te$_3$[32].

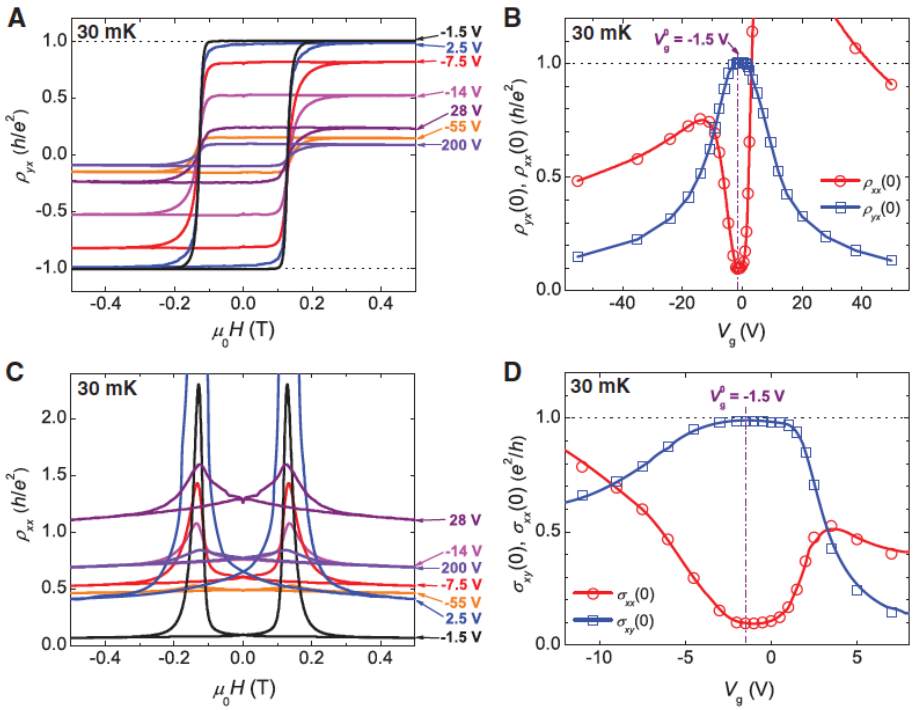

Fig. 1.9 Experimental observation of quantized anomalous Hall effect. Magnetic field dependence of (A) Hall resistivity ρ_{yx} and (B) longitudinal resistivity ρ_{xx}. (C) Gate voltage dependence of Hall resistivity and longitudinal resistivity in zero magnetic field. (D) Gate voltage dependence of hole conductivity σ_{xy} and longitudinal conductivity σ_{xx}.

Magnetic Weyl semimetals

Magnetic order can lift the spin degeneracy of electronic bands and possibly realize Weyl semimetal phases with broken time reversal symmetry. The Weyl semimetal phase was first predicted for pyrochlore-type iridium oxides $R_2Ir_2O_7$ (R = rare earth atom) showing all-in-all-out type antiferromagnetic order[116]. The physical properties vary systematically depending on the ionic radii of the R site, i.e. the strength of electron correlation; $Pr_2Ir_2O_7$ is nonmagnetic metal at all temperatures, while (Eu, Nd)$_2Ir_2O_7$ show magnetic order and become insulating at low temperatures. Weyl semimetal phase is theoretically predicted depending on the strength of correlation[34]. However, Weyl semimetal phase is not experimentally confirmed so far, possibly because the Weyl phase is realized only in a narrow temperature range just below the magnetic ordering temperature[116].

More recently, Mn_3Sn was also shown to be a Weyl semimetal with broken time reversal symmetry[80]. Mn_3Sn shows extremely large anomalous Hall effect even at the room temperature as shown in Fig.1.10[84]. Recently, this large anomalous Hall

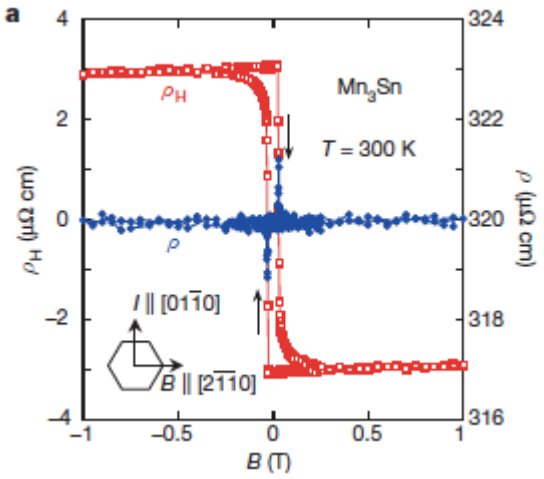

Fig. 1.10 Giant anomalous Hall effect in Mn_3Sn at 300 K[84].

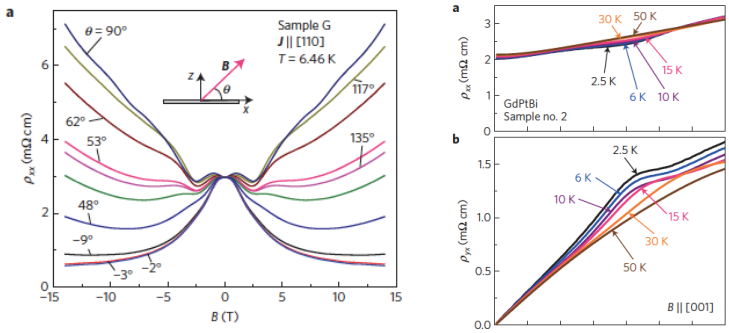

Fig. 1.11 The negative magnetoresistance due to the chiral anomaly[81] (left) and Hall resistivity showing anomalous contribution at $B \sim 4$ T[82] (right) in GdPtBi.

signal was suggested to arise from the Weyl fermion state[80]. Hence, this large anomalous Hall effect is one example of the peculiar magnetotransport phenomena observed in magnetic Dirac materials. Unfortunately, however, the carrier mobility in Mn_3Sn is as low as ~ 1 cm^2/Vs due to the correlation of the Mn $3d$ orbitals forming the Weyl semimetal states.

Furthermore, the Weyl semimetal phases induced by an external magnetic field are sought in semimetals hosting local magnetic moments, such as GdPtBi[81, 82], $EuTiO_3$[83] and $\alpha-EuP_3$. There, the spin degeneracy of the bands near the Fermi level is lifted by the exchange interaction with the local magnetic moments showing net magnetization. The spin non-degenerate bands host Weyl semimetal phase at some magnetization value, leading to peculiar magnetotransport properties such as the negative longitudinal magnetoresistance due to the chiral anomaly[83] and the anomalous Hall resistivity[82, 83] as shown in Figs. 1.11 and 1.12.

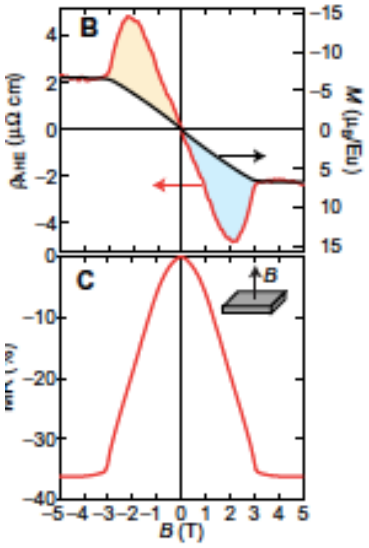

Fig. 1.12 The anomalous Hall effect arising from the field-induced Weyl points in $EuTiO_3$ thin film[83].

1.4 Dirac materials based on the Bi square net

Recently, a layered pnictide $SrMnBi_2$ was shown to host quasi-2-dimensional Dirac fermion by *ab initio* calculations, ARPES and magnetotransport measurements. This compound is the prototype is the materials group $AMBi_2$ (A = alkaline earth, rare earth metals, M = transition metals). Here we overview the recent studies on $SrMnBi_2$ and related compounds.

Dirac fermion in $SrMnBi_2$

Crystal and electronic structure

The crystal structure of $SrMnBi_2$ consists of a MnBi layer with edge-sharing $MnBi_4$ tetrahedrons and a two-dimensional (2D) Bi square net stacked with Sr atoms as shown in Fig. 1.13 (a)[38]. The space group belongs to $I4/mmm$ and the lattice constants are $a = 4.58(1)$ Å, $c = 23.13(3)$ Å. Sr^{2+} and Bi^{3-} in the MnBi layer form closed shell electron configuration. Mn^{2+} has a half filled $3d^5$ configuration with spin $S = 5/2$, which order antiferromagnetically below $T_N \sim 290$ K. Bi^{1-} ($6s^2 6p^4$) form covalent-type bonding with each other, forming the Bi square net layer.

Bi^{1-} ($6s^2 6p^4$) forms two covalent bonds in the usual Zintl concept, but Bi^{1-} in Bi square net has four nearest neighbor Bi^{1-} site. This is understood by the idea of hypervalent bonding[40]. For heavy elements such as Bi, the s orbital is drawn near the center due to the strong electrostatic attraction of the nucleus, while the p orbital

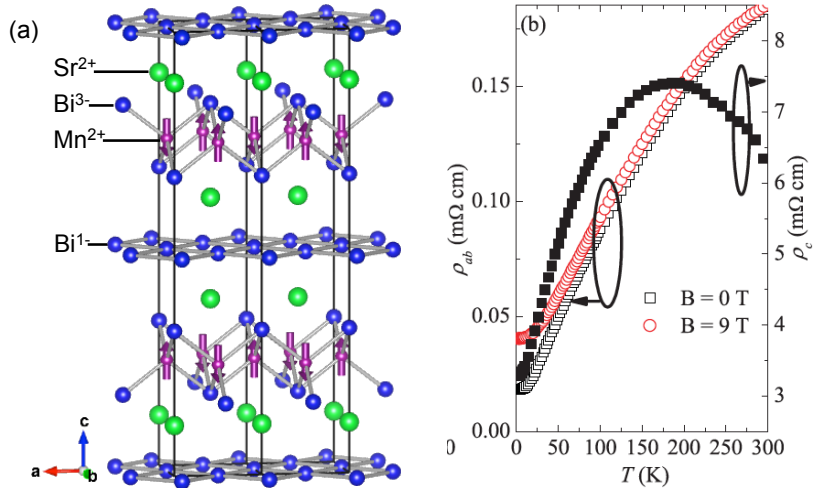

Fig. 1.13 (a) Crystal structure of $SrMnBi_2$. The magnetic structure of Mn site is according to ref. [45]. The solid line represents a unit cell. (b) Temperature dependence of in-plane resistivity and interlayer resistivity [39].

is elongated by the shielding effect of other inner nuclear electrons. This reduces the spatial overlap between the s orbital and the p orbital, making the $s-p$ hybridization weaker. As a result, in the Bi^{1-} square lattice, the s orbital and the p_z orbital form lone pairs, and the $p_{x,y}$ orbitals form covalent-type bonding to form a semi-metallic band.

Fig. 1.13 (b) shows the temperature dependence of in-plane resistivity and interlayer resistivity. The metallic behavior of the in-plane resistivity is derived from the semi-metallic band on the Bi square net. On the other hand, the interlayer resistivity is about 100 times larger than the in-plane resistivity and shows a nonmonotic temperature dependence with high-temperature non-metallic region and low-temperature metallic region. This temperature dependence is characteristic of quasi-2D systems showing a crossover from high-T incoherent to low-T coherent conduction. The existence of a thick ($\sim$ 1 nm) insulating layer made of Sr, Mn and Bi between the Bi square net causes strong anisotropy in the electronic characteristics.

Observation of the Dirac fermion

It is revealed in 2011 that semimetallic bands on the Bi square net form quasi-two-dimensional Dirac fermions. According to the first principle calculation, the Fermi surface of the Dirac fermion exists in the $\Gamma - M$ direction of the Brillouin zone (Fig. 1.14 a). The Dirac band has anisotropy within the in-plane direction, with the Fermi velocity along the $\Gamma - M$ direction is about 8 times larger than that in the perpendicular direction (Fig. 1.14 b). There are four equivalent Fermi surfaces corresponding to the four-fold rotational symmetry of the crystal. Existence of such Dirac fermions arising from the Bi square net was experimentally confirmed directly

by the ARPES measurements.

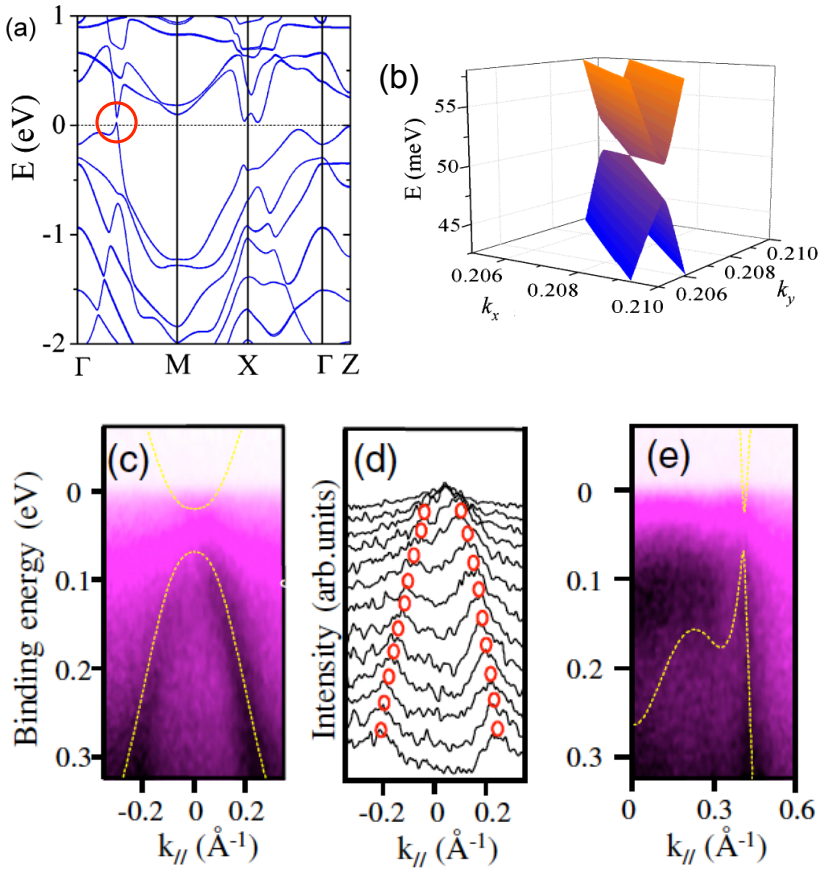

Fig. 1.14 (a) Band structure of $SrMnBi_2$ by first principles calculation. Red circle indicates Dirac point. (b) Schematic diagram of anisotropic Dirac electrons. (c-e) Band structure of Dirac electrons observed by ARPES.[41]

Transport properties

Quantum transport phenomena of $SrMnBi_2$ are studied at low temperatures and strong magnetic fields. The in-plane resistivity linearly increases with respect to the magnetic field along the c axis. A linear magnetoresistance is observed over a wide temperature range of up to 50 K and is thought to originate from Dirac fermions on the Bi square net[39]. Detailed analysis of quantum oscillation revealed the existence of finite Berry's phase and small cyclotron mass[41], which is consistent to the Dirac electronic structure. Recently it has been suggested that the four-fold symmetry of the valley is broken under the strong magnetic field of more than 15 T from the measurement of the angle dependence of the interlayer resistivity[73].

$SrMnBi_2$ hosts magnetic Mn atoms along with the Dirac fermion: $SrMnBi_2$ itself is a magnetic Dirac material, and therefore is of interest in terms of the coupling

between the magnetic order and the Dirac fermion. Guo et al. investigated two kinds of antiferromagnetic order of the Mn site (in-plane checkerboard type and ferromagnetic/antiferromagnetic interlayer coupling) by first-principle calculations, and revealed that the Dirac electronic structure is slightly modulated by the Mn antiferromagnetic order[45]. However, only slight anomaly is observed in the resistivity at the Mn antiferromagnetic ordering temperature, suggesting that the Mn magnetism shows only slight influence on the transport properties of the Dirac fermions.

Recent researches in related compounds

Basic physical properties of $EuMnBi_2$

After some time from the start of this research, the basic physical properties of $EuMnBi_2$ was reported [44]. Eu magnetic moments show antiferromagnetic order at $T_N \simeq 22$ K. Upon then, the in-plane resistivity shows clear anomaly, indicating that the transport properties of the Dirac fermion is sufficiently coupled to the Eu magnetism. Recent ARPES measurements revealed the existence of Dirac fermion in $EuMnBi_2$[65]. However details of the coupling between the Eu magnetic order and the Dirac fermion is unclear.

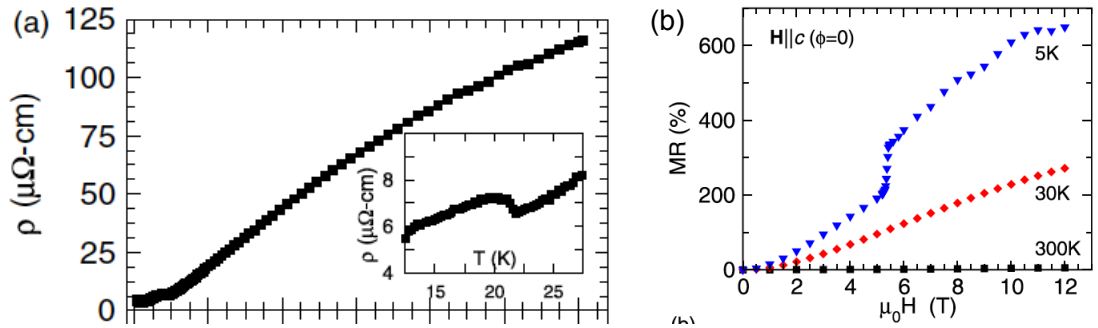

Fig. 1.15 (a) Temperature dependence of in-plane resistivity of $EuMnBi_2$. The inset is an enlarged view around $T_N \sim 22$ K. (b) Magnetic field dependence of magnetoresistance $MR = (\rho(H) - \rho(0))/\rho(0)$.

1.5 Purpose of this thesis

As we have seen, the back scattering of carriers is suppressed in the Dirac electron system, so high mobility is realized and it is expected to be applied to high-speed and energy-saving devices. Dirac electron systems themselves also exhibit peculiar quantum transport phenomena under low temperature and strong magnetic fields due to the feature that the presence of high mobility carriers and the quantum limit state can be easily realized. On the other hand, in magnetic materials, a unique magnetic transport phenomenon is observed due to the combination of magnetic order and

conduction properties, and a system exhibiting giant magnetoresistance is applied to spintronics. In a system having both Dirac electrons and magnetism, it is expected that a new novel magnetic transport phenomenon will be developed by the coupling of the quantum transport phenomenon and the magnetic structure of Dirac electrons, and it is expected to be applied to future electronic devices.

However, systems that combine magnetism and Dirac electrons are very limited at present. In topological insulator thin films doped with magnetic elements, attention has been drawn to the fact that quantum anomalous Hall effect accompanying ferromagnetic order is reported, but the subject of experimental research is almost $(Bi, Sb)_2(Te, Se)_3$ or thin-film multilayer structuring of the system doped with it, and the material variation is extremely poor. In the metallic phase of the pyrochlore type Ir oxide, the existence of Weil electrons is suggested, but no direct experimental evidence exists, and since a sample excellent in crystallinity is not obtained, quantum derived from Weil electron Transport phenomena have not been observed. In this way, research on a system having both magnetism and Dirac electrons is very limited, and the degree of freedom of material design is further poor.

From this viewpoint, in this research, we focused on the material group related to layered Dirac electron system $SrMnBi_2$. This system has Dirac electrons in the conductive layer Bi tetragonal lattice, while it contains Mn as a magnetic element in the insulating layer and is one of the Dirac electron systems with few magnetism. Dirac electrons are expected to be lost by the chemical substitution of Sr and Mn in the insulating layer, because the bismuth square lattice of the conductive layer is responsible for Dirac electrons. As a reinforcement of this speculation, the author has obtained results suggesting the existence of Dirac electrons in $(Ba, Sr)ZnBi_2$ which has the same structure in the past. From this, it is expected that by replacing Sr and Mn with magnetic elements, it is possible to introduce magnetism into the Dirac electron system and to explore a novel magnetic transport phenomenon.

Among them, $EuMnBi_2$ is expected to strongly influence the conduction of Dirac electrons, since magnetic Eu ions exist adjacent to the Bi square lattice. Abnormality of resistivity associated with antiferromagnetic transition and spin flop transition has been reported so far but its detailed behavior and mechanism have not been clarified at all.

In this research, we focused on $EuMnBi_2$ in particular, and conducted research for the following purposes.

- Detailed measurement of magnetic properties and transport properties over a strong magnetic field will be conducted to explore a novel magnetic transport phenomenon by combining the magnetism of Eu / Mn and the quantum transport phenomenon of Dirac electrons.
- Detailed analysis of magnetic transport phenomena, and directly track changes in electronic structure due to coupling with Eu / Mn magnetism.
- Through analysis of magnetic structures and comparison with similar substances, we approach the microscopic mechanism of observed magnetic trans-

port phenomena.

Chapter 2

Experimental Methods

2.1 Single crystal growth

Single crystals of $AM\mathrm{Bi}_2$ (A=Sr, Eu, Ba, M=Mn, Zn,Cd) were grown by the Bi self-flux method. For EuMnBi_2, high-purity ingots of Eu (99.9%), Mn (99.9%), and Bi (99.999%) were mixed in the ratio of Eu/Mn/Bi = 1:1:9 and put into an alumina crucible in an argon-filled glove box. The ratios of the mixture for other compounds are shown in Tab. 2.1. The crucible was sealed in an evacuated quartz tube and heated at $T_1 = 1000$ °C for 10 hours, followed by slow cooling from $T_2 = 650$ °C to $T_3 = 400$ °C at the rate of ~ 2 °C/hour, where the excess Bi flux was decanted using a centrifuge as shown in Fig. 2.1(a). The values of T_1, T_2 and T_3 for other compounds are shown in Tab. 2.1 Plate-like single crystals with atypical size of $\sim 5 \times 5 \times 1$ mm^3 shown in Fig. 2.1(b) were obtained.

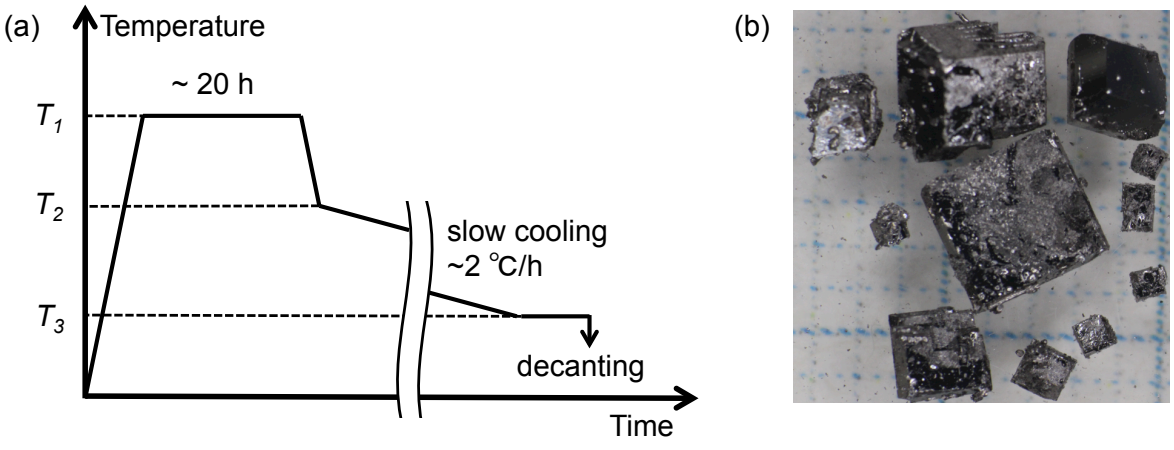

Fig. 2.1 (a) Temperature profile for the single crystal growth of $AM\mathrm{Bi}_2$. The values of $T_{1,2,3}$ for each compounds are shown in Tab. 2.1. (b) Single crystals of EuMnBi_2 grown by the self-flux method.

compounds	ratio of the mixture	T_1 (C°)	T_2 (C°)	T_3 (C°)
$EuMnBi_2$	Eu/Mn/Bi = 1 : 1 : 9	1000	700	400
$EuZnBi_2$	Eu/Zn/Bi = 1 : 5 : 10	900	800	400
$(Ba, Sr)ZnBi_2$	(Ba, Sr)/Zn/Bi = 1 : 2 : 10	900	650	400
$(Eu, Sr)CdBi_2$	(Eu, Sr)/Cd/Bi = 1 : 5 : 10	900	650	400

Tab. 2.1 Details of the synthesis methods of $AMBi_2$ (A=Sr, Eu, Ba, M=Mn, Zn, Cd). Definitions of T_1, T_2 and T_3 are shown in Fig. 2.1(a).

2.2 Evaluation of the crystal structure and the chemical composition

The obtained samples were characterized by the powder x-ray diffraction technique with a Cu Kα radiation on a Bruker D8 advance diffractometer. The crystal orientation was determined from x-ray Laue patterns. The chemical composition of the single crystals were determined by the EDX technique on a Hitachi Scanning Electron Microscope S-4300.

2.3 Magnetization measurement

Magnetization up to 7 T were measured down to 1.9 K using Magnetic Property Measurement System (QuantumDesign).

2.4 Electrical resistivity, Hall resistivity, Magnetoresistance

In-plane resistivity ρ_{xx} and Hall resistivity ρ_{yx} were measured by a conventional five-terminal method with electrodes formed by room temperature curing silver paste as shown in Fig. 2.2(a). The typical sample dimension is ∼2.0 mm (length) × 0.5 mm (width) × 0.1 mm (thickness). The voltage terminals were needed to cover the whole thickness of the sample side to avoid the admixture of the interlayer resistance. Interlayer resistivity ρ_{zz} was measured by a four-terminal method on bar-shaped samples with a typical dimension of ∼1.5 mm in length along the c axis and ∼0.4 × 0.4 mm^2 in cross section as shown in Fig. 2.2(b). Current terminals were formed so as to completely short out the in-plane current.

2.5 High-field mesurements

Measurements using the pulsed magnet

The magnetization and resistivity up to 55 T were measured using the nondestructive pulsed magnet with a pulse duration of 36 ms at the International MegaGauss Science

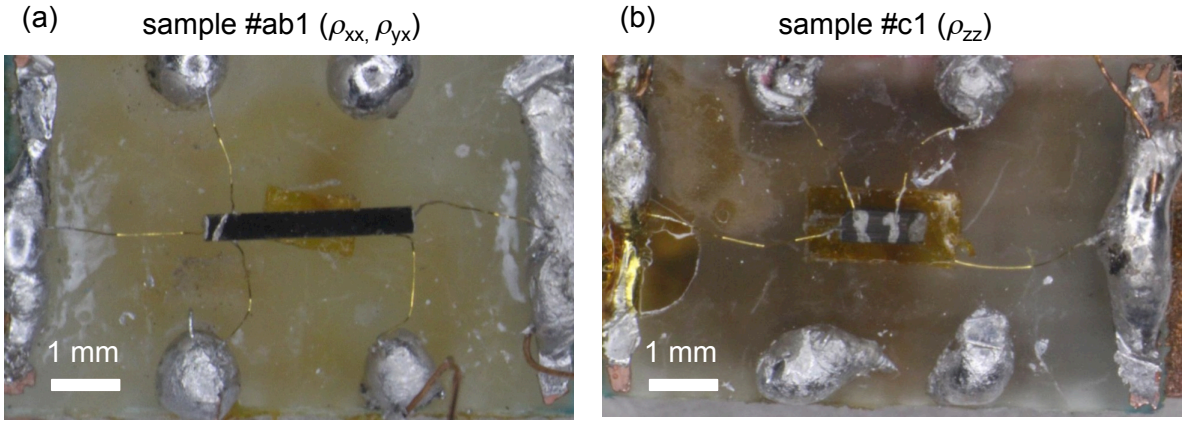

Fig. 2.2 Geometry of the samples and electrodes for the resistivity measurements.

Laboratory at the Institute for Solid State Physics. The measurement temperature range was 1.9 to 150 K. The magnetization was measured by the induction method, using coaxial pickup coils. The resistivity (ρ_{xx}, ρ_{yx}, and ρ_{zz}) was measured by a lock-in technique at 100 kHz with ac excitation of 1 to 10 mA.

Measurement using the hybrid magnet

The resistivity measurement up to 28 T at ∼50 mK was performed with a lock-in amplifier at 17Hz with ac excitation of 100 mA by using a dilution refrigerator embedded in the cryogen-free hybrid magnet at High Field Laboratory for Superconducting Materials in the Institute of Materials Research, Tohoku University[42].

2.6 Resonant x-ray magnetic scattering

Resonant x-ray magnetic diffraction measurements on $EuMnBi_2$ and $EuZnBi_2$ were performed at BL-3A, Photon Factory, KEK, Japan, by utilizing the horizontally polarized x-ray in resonance with Eu L_3 absorption edge (∼6.975 keV). We used a relatively thick sample with the (0 0 1) and (1 0 L) natural facets ($L \sim 1$ - 2) with a dimension of $\sim 3 \times 2 \times 1.5$ mm^3. The (0 0 L) and (1 0 L) reflections were measured on the (0 0 1) natural facet at the temperatures of 5 to 300 K by attaching the sample to the cold finger of a He closed-cycle refrigerator on a four-circle diffractometer. The (4 0 1) and (3 0 0) reflections were measured on the (1 0 L) natural facet at the temperatures from 5 K to 40 K in the magnetic field along the c axis using a superconducting magnet equipped on a two-cycle diffractometer. For selected magnetic reflections, we performed polarization rotation measurements, where the polarization of scattered x-rays was analyzed by utilizing a Cu(110) single crystal. Unless otherwise stated, the scattered x-rays were detected without analyzing polarization and hence include both the σ'- and π'-polarization components. For all the measurements, we used a

silicon drift detector.

2.7 Single crystal neutron diffraction

Single crystal neutron diffraction experiments on $EuMnBi_2$ were carried out using the time-of-flight single-crystal neutron diffractometer SENJU at the Materials and Life Science Experimental Facility (MLF) of the Japan Proton Accelerator Research Complex (J-PARC). The wave-length range of incident neutrons was selected to be 0.4 - 4.4 Å. A plate-like single crystal sample of $EuMnBi_2$ with a dimension of $3 \times 3.5 \times 1$ mm^3 was chosen for the experiments. The neutron diffraction patterns in the magnetic field along the c axis were measured using a vertical-field superconducting magnet for the AFM phase (2 K, 6 T), SF phase (2 K, 6 T) and PM phase (25 K, 6 T), respectively.

2.8 Electronic structure calculation

We performed first-principles band structure calculations using the density functional theory with the generalized gradient approximation [100] and the projector augmented wave method [101] as implemented in the Vienna *ab initio* simulation package [102, 103, 104, 105]. The spin-orbit coupling and the $+U$ correction [106, 107] with $U_{eff} \equiv U - J$ =2 eV for Eu-f electrons were included. Note here we did not include the $+U$ correction for Mn-d electrons, because the positions of the Mn-d bands in $SrMnBi_2$ are known to be well reproduced without the $+U$ correction[39, 108]. For all the calculations, a tetragonal unit cell containing four formula units was chosen in order to represent the AFM orders of the Mn and Eu spins. The plane-wave cutoff energy of 350 eV and a 16 × 16 × 4 k-mesh were used. Lattice parameters and atomic coordinates were taken from experiment[44]. To see the dependence of spin splitting on $U_{eff} \equiv U - J$ for Eu-f electrons, we also performed the calculations with U_{eff} = 4 and 6 eV.

Chapter 3

Exploration of the $AM\mathrm{Bi}_2$ phases

3.1 Characterization and the lattice parameters in $AM\mathrm{Bi}_2$ phases

Fig. 3.1(a-c) show the powder x-ray diffraction profiles of $EuMnBi_2$, $SrMnBi_2$ and $EuZnBi_2$ at room temperature. All of these materials crystallizes in a tetragonal unit cell with a space group of $I4/mmm$. The lattice constants estimated from the Le Bail fitting of the measured profiles are shown in Tab. 3.1.

	a (Å)	c (Å)
$EuMnBi_2$	4.5416(4)	22.526(2)
$SrMnBi_2$	4.5609(4)	23.104(2)
$EuMnBi_2$	4.6170(3)	21.354(2)

Tab. 3.1 Lattice parameters of $AM\mathrm{Bi}_2$ (A=Sr, Eu, M=Mn, Zn) evaluated by the powder x-ray diffraction profiles.

3.2 Coupling between the magnetic order and resistivity

FIg. 3.2 (a-c) show the temperature dependence of the magnetic susceptibility M/H under the magnetic field along the c axis, the interlayer resistivity ρ_{zz} and the in-plane resistivity ρ_{xx}, respectively, for $EuMnBi_2$, $SrMnBi_2$ and $EuZnBi_2$.

For $SrMnBi_2$, the antiferromagnetic order of the Mn sublattice is observed in the magnetic susceptibility at $T_N(\mathrm{Mn})\sim$ 300 K as shown in Fig. 3.2(a). $EuMnBi_2$ also show the Mn antiferromagnetic order for below $T_N(\mathrm{Mn})\sim$ 315 K[44]. However, almost no anomaly is observed in the interlayer and in-plane resistivity ρ_{zz}, ρ_{xx} at $T_N(\mathrm{Mn})$ as shown in Fig. 3.2(b, c). This indicates that the Mn magnetic order barely affects the transport properties of the Dirac fermion.

For $Eu(Mn,Zn)Bi_2$, the antiferromagnetic order of the Eu sublattice is clearly ob-

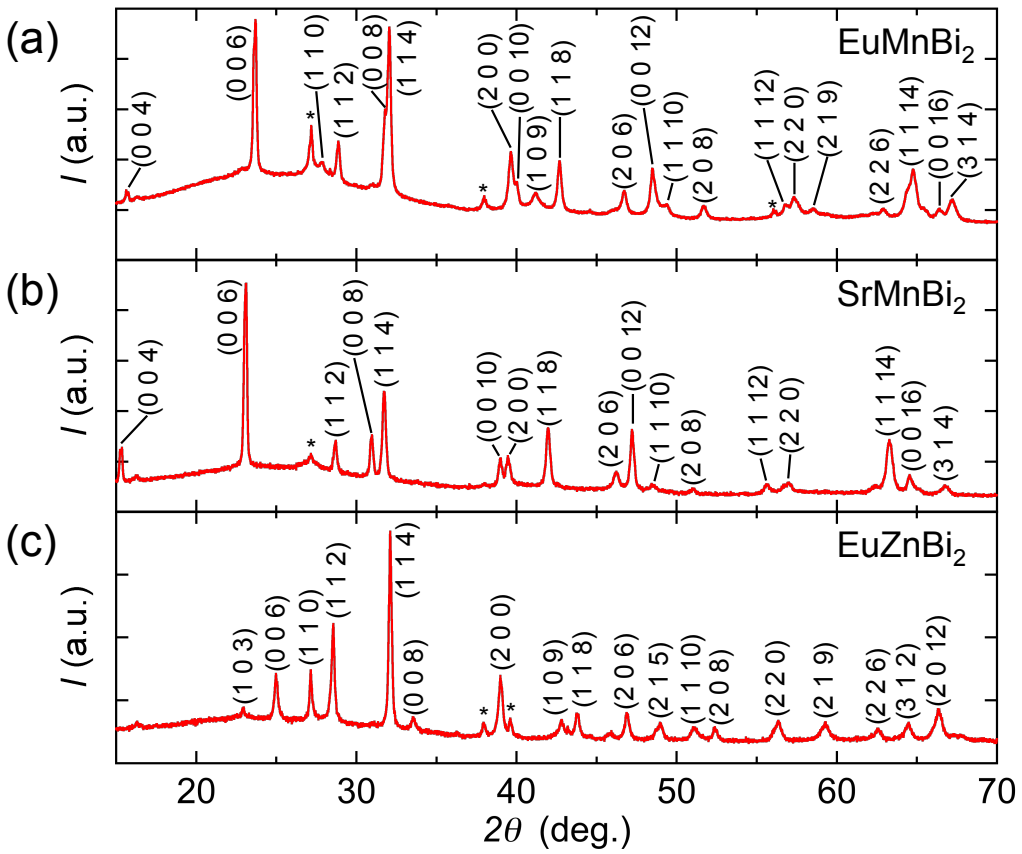

Fig. 3.1 Profiles of the $2\theta - \theta$ powder x-ray diffraction for $EuMnBi_2$, $SrMnBi_2$, and (C) $EuZnBi_2$ measured by Cu-Kα radiation at room temperature. The numbers in each panel are Miller indices based on the space group $I4/mmm$. * denotes the reflections from the Bi flux stuck to the crystal surfaces.

served in the magnetic susceptibility at T_N(Eu)$\sim$ 22 K as shown in Fig. 3.2(a). The difference in M/H below T_N(Eu) in Eu(Mn,Zn)Bi_2 indicates the different orientations of the Eu moments in two compounds. Interestingly, both Eu(Mn, Zn)Bi_2 show clear cusp-like anomaly in ρ_{xx} and sharp increase in ρ_{zz} at T_N(Eu). This evidences that the magnetic order of the Eu sublattice strongly influences the conduction in the adjacent Bi tetragonal lattice layer. On the other hand, it can be seen from Fig. 3.2(c) that the ρ_{zz} value of (Sr, Eu)$MnBi_2$ is larger than that of $EuZnBi_2$ by more than one order of magnitude in the entire temperature range. Furthermore, broad maximum appears in ρ_{zz} of (Sr, Eu)$MnBi_2$ at around 200 K, which signifies the crossover from the high-temperature incoherent regime to the low-temperature coherent interlayer conduction regime, typical of quasi-two-dimensional metals. ρ_{xx}, on the other hand, shows metallic temperature dependence at all temperatures for all the compounds. This indicates that the Mn layer increases ρ_{zz} and makes the system

more two-dimensional.

Hence, in $AM\mathrm{Bi}_2$, by tuning the magnetism in the insulating layer by chemical substitution, we can develop variety of magnetic Dirac materials with different strength of the coupling between the magnetism and the transport or different two dimensionalities. In the following chapters, we focus on EuMnBi_2, which hosts strong two-dimensionality and strong magnetism-transport coupling, and show that the quantum transport properties of the Dirac fermion is strongly coupled to the Eu magnetic order.

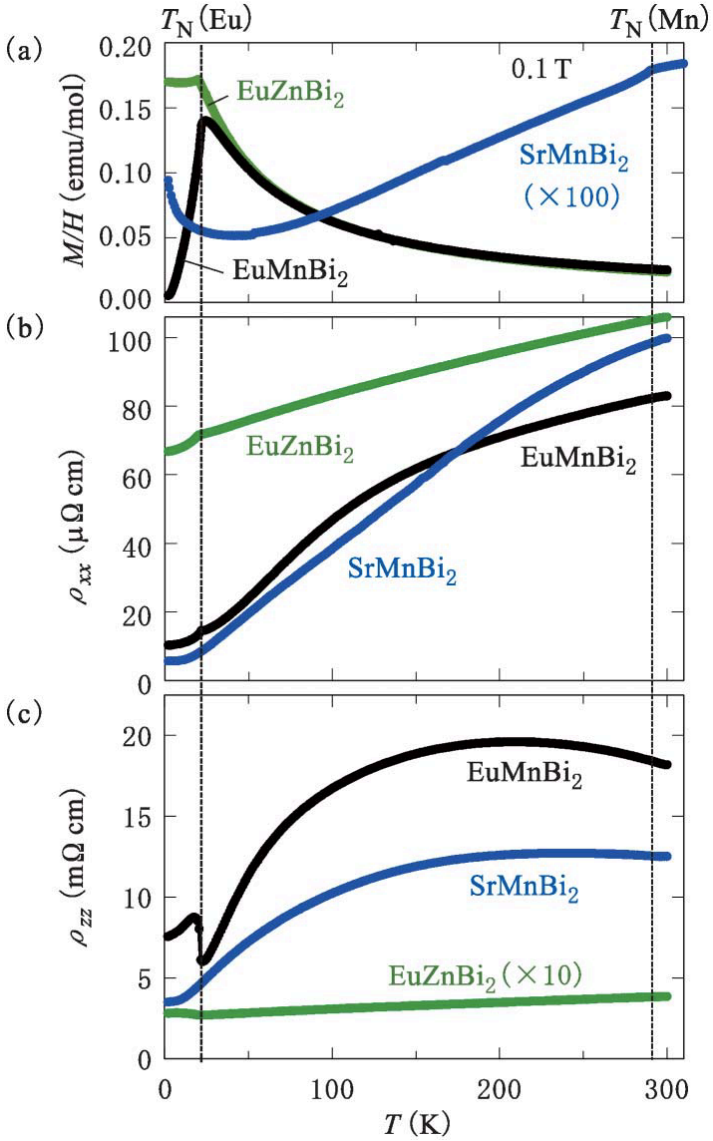

Fig. 3.2 Temperature dependence of the (a) magnetic susceptibility M/H (0.1 T, $H||c$), (b) interlayer resistivity ρ_{zz}, and (c) in-plane resistivity ρ_{xx} for $\mathrm{SrMnBi_2}$, $\mathrm{EuMnBi_2}$ and $\mathrm{EuZnBi_2}$. T_N(Eu) and T_N(Mn) are the antiferromagnetic transition temperatures for the Eu ($\mathrm{EuMnBi_2}$ and $\mathrm{EuZnBi_2}$) and Mn ($\mathrm{SrMnBi_2}$ and $\mathrm{EuMnBi_2}$) sublattices, respectively.

Chapter 4

Discovery of novel magnetic Dirac material $EuMnBi_2$

Here, By applying fields up to 55 T that enable complete control of the magnetic order of Eu sublattice, we demonstrate its strong impact on interlayer hopping of quasi-2D Dirac fermions on the Bi layer, which gives rise to the bulk multilayer quantum Hall state.

4.1 Dirac fermions state coupled to the magnetic order

As shown in Fig. 4.1A, the magnetic susceptibility M/H parallel to the c axis for $EuMnBi_2$ steeply decreases below the antiferromagnetic (AFM) transition temperature $T_N \sim 22$ K, indicating that the Eu moments are aligned parallel to the c axis[44]. To reveal the AFM arrangement of the Eu sublattice, we have measured the resonant x-ray scattering spectra near the Eu L_3 absorption edge. At 5 K, we found the (0 0 11) reflection at $E = 6.975$ keV that is forbidden in the present space group ($I4/mmm$) (inset to Fig. 4.1B). Considering the evolution of the reflection intensity below T_N (Fig. 4.1B) and the observation of polarization rotation as well as a sharp resonance at the Eu L_3 edge (Fig. 4.7), it can be assigned to resonant magnetic scattering from the Eu sublattice. In Sec. 4.3, we derive the most probable magnetic structure as shown in Fig. 4.1E. The Eu moments order ferromagnetically in the ab plane and align along the c axis in the sequence of up-up-down-down, where the Bi square net intervenes between the Eu layers with magnetic moments up and down. This magnetic arrangement can be regarded as a natural spin valve-like superstructure.

Figure 4.1 (C and D) shows the temperature profiles of in-plane (ρ_{xx}) and interlayer (ρ_{zz}) resistivity for $EuMnBi_2$, respectively. At 0 T below 120 K, both the ρ_{xx} and ρ_{zz} curves show metallic behavior down to T_N, but the anisotropy is fairly large (for example, $\rho_{zz}/\rho_{xx} \sim 480$ at 50 K at 0 T). At T_N, we observed a small drop (or cusp-like anomaly) in ρ_{xx} and a steep jump in ρ_{zz} toward the lowest temperature. These transport properties seem to be consistent with the AFM order of the Eu layer;

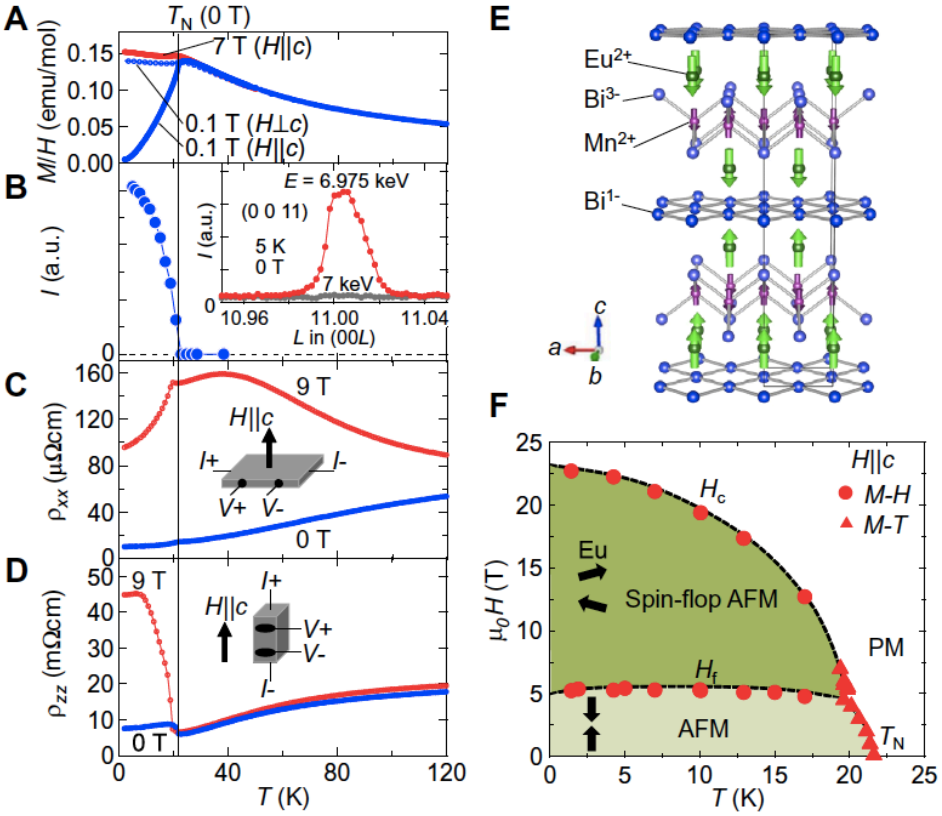

Fig. 4.1 Transport coupled with the magnetic order of Eu sublattice. (A to D) Temperature dependence of magnetic and transport properties near the AFM transition temperature (T_N) for $EuMnBi_2$. (A) Magnetic susceptibility M/H for the field parallel to the c axis ($H||c$) at 0.1 T (blue) and 7 T (red). Open symbols are the data for the field perpendicular to the c axis ($H \perp c$) at 0.1 T. (B) Intensity of resonant magnetic reflection (0 0 11) at 6.975 keV at 0 T. The inset shows the profile of the (0 0 11) reflection along [001] at 6.975 keV (resonant) and 7.00 keV (nonresonant). In-plane resistivity ρ_{xx} (C) and interlayer resistivity ρ_{zz} (D) at 0 and 9 T ($H||c$). Schematic sample configuration for the resistivity measurement is shown in each panel. emu/mol, electromagnetic unit per mole; a.u., arbitrary unit. (E) Schematic illustration of the plausible magnetic structure for $EuMnBi_2$ at zero field, together with the formal valence of each ion. The arrangement of the Mn sublattice is assumed to be the same as in $SrMnBi_2$[45]. (F) Magnetic phase diagram for the Eu sublattice as functions of field ($H||c$) and temperature. PM and AFM denote the paramagnetic and antiferromagnetic states, respectively. H_f and H_c correspond to the transition fields to the spin-flop AFM and PM (forced ferromagnetic) phases, respectively. Black arrows are schematic illustration of the Eu moments sandwiching the Bi^-1 layer. Note the Mn sublattice orders at ~ 315 K ($> T_N$).

the interlayer conduction should be suppressed by the staggered Eu moments along the c axis, whereas the ferromagnetic order within the plane may promote the in-plane one. The application of the field parallel to the c axis has a strong impact on the temperature profiles of ρ_{xx} and ρ_{zz} (red curves in Fig. 4.1, C and D). At 9 T, $\rho_{xx}(T)$ exhibits marked positive magnetoresistance effects that evolve with decreasing temperature down to $\sim$ 40 K, followed by a steep drop at T_N. On the other hand, $\rho_{zz}(T)$ at 9 T shows minimal (longitudinal) magnetoresistance effects above T_N, but shows a much larger jump on cooling at T_N than that at 0 T. These suggest that the increase of anisotropy in resistivity below T_N is further enhanced at 9 T; the increase in ρ_{zz}/ρ_{xx} with decreasing temperature from 25 K (just above T_N) to 2 K exceeds 1000% at 9 T, whereas it is approximately 180% at 0 T. Judging from the temperature profile of M/H at 7 T for $H||c$ in Fig. 4.1A (and also magnetic phase diagram in Fig. 4.1F), the Eu moments are oriented perpendicular to the c axis in the AFM phase at 9 T, which appears to strongly suppress the interlayer conduction between the Bi layers. We will again discuss the effect of the Eu spin flop on the resistivity in terms of its field profile (vide infra).

The magnetotransport properties enriched by the Eu magnetic order are further highlighted by the magnetization and resistivity measured in the magnetic field up to 55 T applied along the c axis (Fig. 4.2). The magnetization at 1.4 K exhibits a clear metamagnetic (spin-flop) transition at $H = H_f$ ($\sim$ 5.3 T), corresponding to the reorientation of the Eu moments to be perpendicular to the field (Fig. 4.2A). In the forced ferromagnetic state above H_c ($\sim$ 22 T), the magnetization is saturated close to 7 μ_B, reflecting the full moment of localized Eu $4f$ electrons. The temperature variation of H_f and H_c is plotted in Fig. 4.1F , which forms a typical phase diagram for an anisotropic antiferromagnet in the field parallel to the magnetization-easy axis.

The interlayer resistivity is markedly dependent on the AFM states of the Eu sublattice (Fig. 4.2B). Above T_N (at 27 and 50 K), ρ_{zz} is almost independent of field, except for clear Shubnikov-de Haas (SdH) oscillations at 27 K. At 1.4 K, on the other hand, ρ_{zz} exhibits a large jump at H_f, followed by giant SdH oscillations that reach $\Delta\rho_{osc}/\rho \sim 50\%$. This high-$\rho_{zz}$ state is terminated at H_c, above which the ρ_{zz} value is substantially reduced. The origin of such ρ_{zz} enhancement (that is, suppression of interlayer coupling) in the spin-flop phase remains as an open question at present: the interlayer charge transfer caused by the electron's hopping on the local Eu moments would not change, if Eu moments were simply reoriented perpendicular to the c axis while keeping the same AFM pattern. We should note here that the Mn sublattice that antiferromagnetically orders at $\sim$ 315 K[44] as well as the Eu one play a vital role in achieving the high-ρ_{zz} state. As shown in the inset in Fig. 4.2B, the ρ_{zz} value at 0 T for $EuZnBi_2$ is reduced to $\sim 1/25$ of that for $EuMnBi_2$, although the plausible AFM order of Eu sublattice at 0 T for $EuZnBi_2$ is analogous to that in the spin-flop phase for $EuMnBi_2$ (that is, the Eu moments are aligned in the ab plane with staggered stacking along the c axis; see fig. 4.10E). For $SrMnBi_2$, on the other hand, the ρ_{zz} value at 0 T is comparable to that for $EuMnBi_2$ but shows

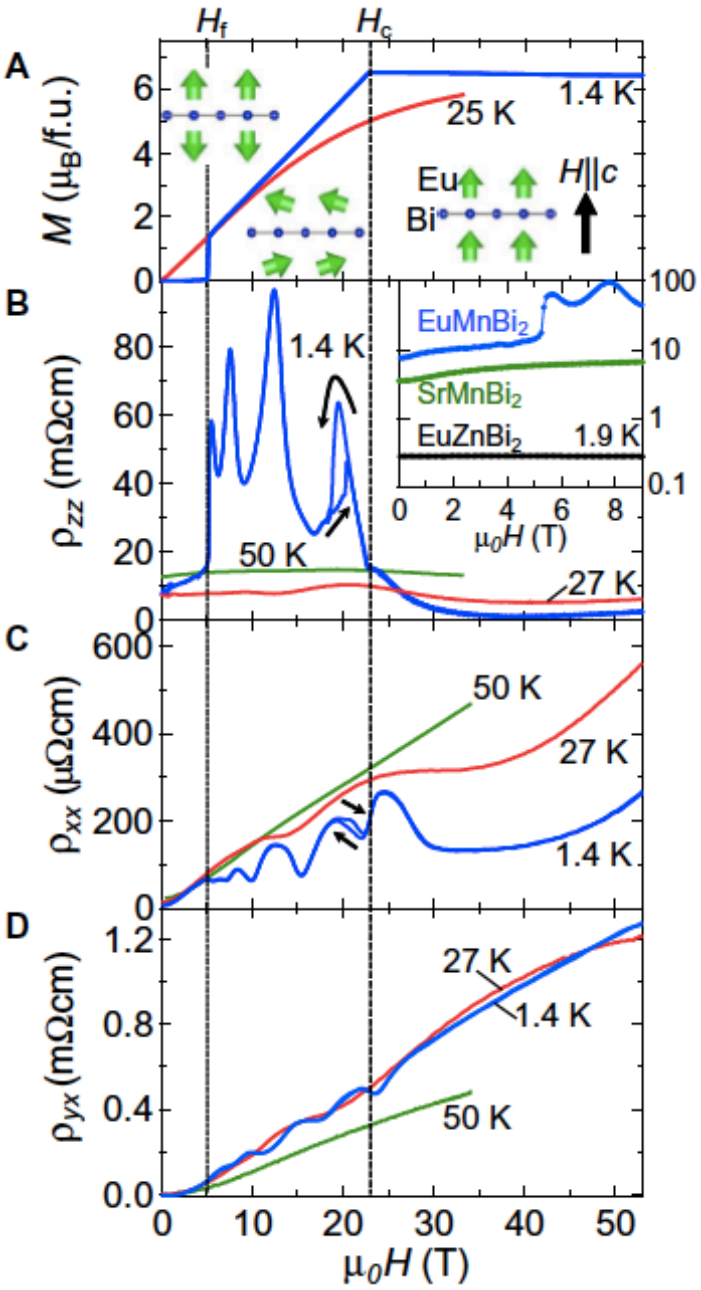

Fig. 4.2 Magnetic field dependence of magnetic and transport properties at high fields. (A to D) M (A), ρ_{zz} (sample #3) (B), ρ_{xx} (C), and Hall resistivity ρ_{yx} (sample #1) (D) for $EuMnBi_2$ at selected temperatures for the field parallel to the c axis up to $\sim$ 55 T. Schematic illustration of the Eu^{2+} moments adjacent to the Bi layer for $H < H_f$, $H_f < H < H_c$, and $H_c < H$ is presented in (A). The inset in (B) shows the field profile of ρ_{zz} (below 9 T) for $EuMnBi_2$, $EuZnBi_2$, and $SrMnBi_2$. f.u., formula unit.

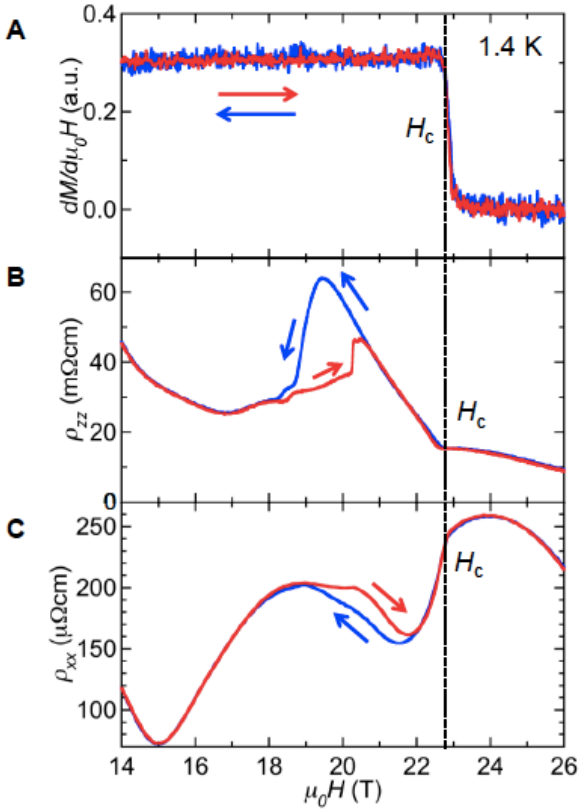

Fig. 4.3 Field profile of (A) derivative of magnetization $dM/d(\mu_0 H)$, (B) in-plane resistivity ρ_{xx} and (C) interlayer resistivity ρ_{zz} at 1.4 K between 14 T and 26 T. Red and blue lines denote the field-increasing and -decreasing runs, respectively. The magnetization (or field derivative of magnetization) curve shows no anomaly at 1.4 K around 20 T, where clear hysteretic anomaly is discerned in the ρ_{xx} and ρ_{zz} curves.

a minimal magnetoresistance effect up to 9 T. The magnetic order in both the Eu and Mn sublattices is thus essential for enhancing ρ_{zz}. As a possible model based on these facts, the magnetic order of the Mn sublattice might be significantly modulated upon the Eu spin flop due to the $f-d$ coupling. It is also likely that we need to take into consideration the anisotropy of Eu^{2+} $4f$ orbital induced by the crystal field splitting[46], which might reduce wave function overlap with the Mn sites along the c axis when the Eu moment and orbital rotate. Revealing the detailed mechanism would, however, be an issue for future experimental and theoretical works.

Another important feature is that the ρ_{zz} peak around 20 T shows a sizable hysteresis between the field-increasing and field-decreasing runs. [Correspondingly, a hysteretic anomaly also manifests itself in ρ_{xx} (Fig. 4.2C).] Because no clear anomaly is discerned in the magnetization curve around 20 T (Fig. 4.3), the Eu moments play a minor role; instead, a possible transition between the Landau levels with different

spin orientation might be responsible for this hysteresis, as discussed below.

The in-plane resistivity exhibits a large positive (transverse) magnetoresistance effect, irrespective of the Eu magnetic order (Fig. 4.2C). At 50 K, the $\rho_{xx}(H)$ profile is strikingly H-linear without saturation up to 35 T, resulting in the magnetoresistance ratio of $\rho(H = 35T)/\rho(0) \sim 2000\%$. Such large H-linear magnetoresistance is occasionally observed in Dirac semimetals [47, 48, 49, 50, 51]. At lower temperatures, the SdH oscillations are superimposed; at 1.4 K, in particular, the magnitude of oscillation is largely enhanced in the spin-flop AFM phase between H_f and H_c, similarly to ρ_{zz}. The enhanced SdH oscillations in the spin-flop phase are also noticeable for the Hall resistivity ρ_{yx} (Fig. 4.2D), which show plateau-like structures at 1.4 K. In the following, we will analyze the details of ρ_{yx} plateaus in terms of the multilayer QHE in the stacking 2D Bi layers.

4.2 Observation of the bulk multilayer quantum Hall effect in the spin-flop phase

In Fig. 4.4A, we plot the inverse of ρ_{yx} at 1.4 K (spin-flop phase) as a function of B_F/B, where B_F is the frequency of SdH oscillation and B is the magnetic induction. B_F/B is the normalized filling factor [corresponding to $\left(n + \frac{1}{2} - \gamma\right)$ in Eq. 4.1[57], which is used to compare the 2 samples with different B_F (Table 4.1). The inverse of ρ_{yx} also exhibits clear plateaus at regular intervals of B_F/B, the positions of which nicely correspond to deep minima in ρ_{xx} (Fig. 4.4B) and pronounced peaks in ρ_{zz} (Fig. 4.4C). All these features signify the multilayer QHE, as previously observed for the GaAs/AlGaAs superlattice[52, 53]. Although the ρ_{xx} minima do not reach zero, $\omega_c\tau$ estimated from ρ_{yx}/ρ_{xx} is much larger than unity (for example, ~ 5 at around $B_F/B = 1.5$;see fig. 4.5A), where ω_c is the cyclotron frequency and τ is the scattering time. What is prominent in the present compound is that the values of $1/\rho_{yx}$ are quantized to half-integer multiples, when scaled by $1/\rho^0_{yx}$, the step size of successive plateaus (see fig. 4.5B for definition). Given the conventional view of QHE, this quantization of $\rho^0_{yx} = \rho_{yx}$ leads to the normalized filling factor of $n + \frac{1}{2}$, where n is a nonnegative integer. This is consistent with the plateaus occurring at half-integer multiples of B_F/B (vertical dotted lines in Fig. 4.4A, where a small shift corresponds to the phase factor as explained below). Such a half-integer (normalized) filling factor is known to stem from the nontrivial π Berry's phase of Dirac fermions [20, 21], which in two dimensions leads to the Hall resistance quantized as follows[54, 55]

$$\frac{1}{R_{yx}} = \pm s \left(n + \frac{1}{2} - \gamma\right) \frac{e^2}{h} \tag{4.1}$$

where e is the electronic charge, h is the Planck' s constant, s is the spin and valley degeneracy factor, and γ is the phase factor expressed as $\gamma = \frac{1}{2} - \frac{\phi_B}{2\pi}$, with ϕ_B as the Berry's phase[56]. The observed half-integer filling factor thus corresponds

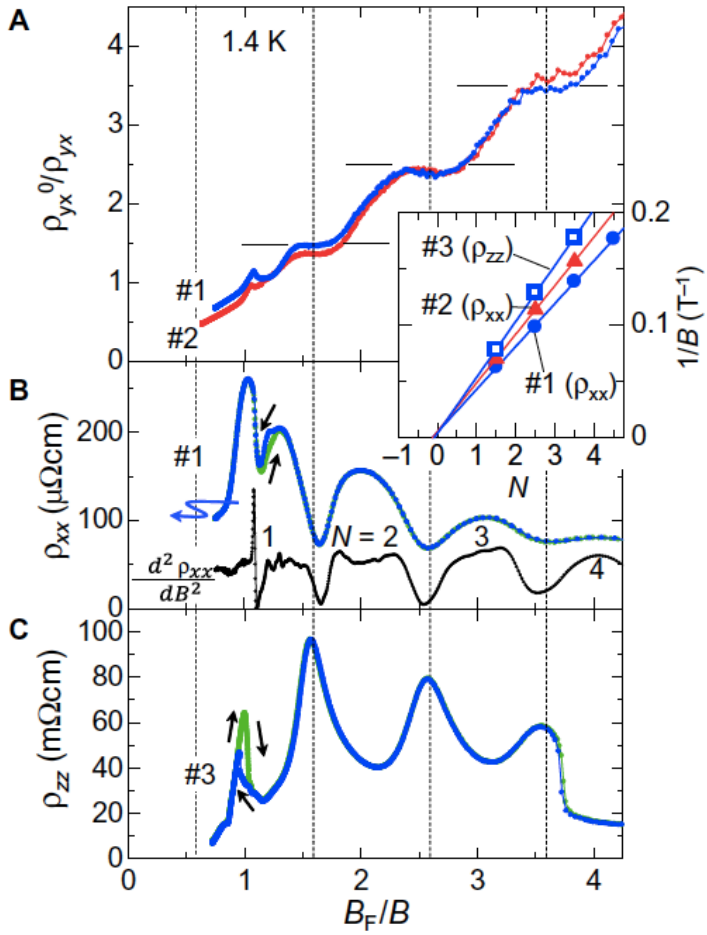

Fig. 4.4 Quantized Hall plateaus and SdH oscillations. (A) Normalized inverse Hall resistivity ρ_{yx}^0/ρ_{yx} versus B_F/B measured at 1.4 K for samples #1 and #2, where B_F is the frequency of SdH oscillation and $B = \mu_0(H+M)$ is the magnetic induction. $1/\rho_{yx}^0$ is the step size between the consecutive plateaus in $1/\rho_{yx}$ (see fig. 4.5B). (B and C) ρ_{xx}, second field derivative $-\,d^2\rho_{xx}/dB^2$ for sample #1 (B) and ρ_{zz} for sample #3 (C) versus B_F/B measured at 1.4 K. Vertical dotted lines denote half-integer multiples shifted by $-\gamma$, where $\gamma \sim -\,0.1$ is a phase factor estimated from the fan plot. (Inset) Landau fan plot ($1/B$ versus N) for #1, #2, and #3. The slope and intercept with the N axis give B_F and $\gamma - \delta$, respectively (Table 4.1). A phase shift δ should be negligibly small for a quasi-2D Fermi surface, as discussed in the main text.

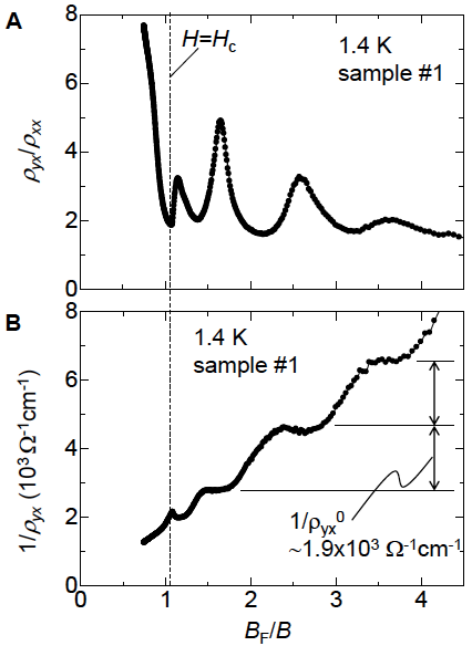

Fig. 4.5 (A) Hall angle ρ_{yx}/ρ_{xx} (corresponding to $\omega_c\tau$) The value of $\rho_{yx}/\rho_{xx} = \omega_c\tau$ is larger than unity in the entire field range of the spin-flop phase and reaches ~ 5 at around $B_F/B = 1.5$. (B) Inverse Hall resistivity $1/\rho_{yx}$ versus B_F/B at 1.4 K for sample #1, where B_F is the frequency of SdH oscillation and $B = \mu_0(H + M)$ the magnetic induction. The data were taken in a field-decreasing run. Horizontal lines in (B) denote the positions of $1/\rho_{yx}$ plateau, from which we have estimated $1/\rho^0_{yx}$, the step size between the consecutive plateaus. For sample #1, for instance, the value of $1/\rho^0_{yx}$ is estimated to be $\sim 1.9 \times 10^3\ \Omega^{-1}\mathrm{cm}^{-1}$ (i.e. $1/\rho^0_{yx} \sim 5.3 \times 10^{-4}\ \Omega\mathrm{cm}$).

to $\gamma \sim 0$, that is, nontrivial π Berry's phase in the present QHE. Furthermore, following standard analyses on the SdH oscillations using fan diagram, we plot the values of $1/B$ at the ρ_{xx} minima [or ρ_{zz} maxima[52, 53]] against half-integers (Fig. 4.4, inset). On the basis of a semiclassical expression of oscillating part in ρ_{xx}[21, 57], $\Delta\rho_{xx} \propto \cos[2\pi(B_F/B - \gamma + \delta)]$, a linear fitting yields $\gamma - \delta$ close to 0 (~ -0.1) for all the samples (Table 4.1), where a phase shift δ is determined by the dimensionality of the Fermi surface, varying from 0 (for 2D) to $\pm 1/8$ (for 3D). Because the value of δ tends to be negligibly small for quasi-2D Fermi surfaces even in bulk materials[57, 58], the fitted results indicate $\gamma \sim -0.1$, which again verifies the nonzero Berry's phase in this compound.

The quantization of ρ^0_{yx}/ρ_{yx} to half-integer multiples is well reproduced for two samples (#1 and #2 in Fig. 4.4A). The thickness of sample #2 is 60% of that of #1. Nevertheless, their difference in ρ^0_{yx} is only ~ 10 %. This fact ensures that the observed Hall plateaus are of bulk origin, which should be attributed to the parallel

Sample No.	ρ_{ij}	B_F (T)	γ (phase factor)	Sample thickness (μm)	ρ^0_{yx} ($\mu\Omega$cm)	s (degeneracy factor)
1	ρ_{xx}, ρ_{yx}	26.1(2)	-0.12(4)	130	525	5.5
2	ρ_{xx}, ρ_{yx}	23.1(2)	-0.12(2)	78	578	5.0
3	ρ_{zz}	19.5(1)	-0.08(2)	-	-	

Tab. 4.1 Parameters related to the SdH oscillations and quantized Hall plateaus in the spin-flop phase (at 1.4 K and 5.3 to 22 T). B_F and γ are the results of linear fit to the Landau fan plot.

transport of the 2D Bi layers stacking along the c axis, as is the case for multilayer quantum Hall systems, including semiconductor superlattice[52, 59], Bechgaard salts[60, 61], Mo_4O_{11}[62, 63], and Bi_2Se_3[64]. The inverse Hall resistivity is hence expressed as $1/\rho_{yx} = Z^*/R_{yx}$, where $Z^* = 1/(c/2) \sim 8.9 \times 10^6 \left(\mathrm{cm}^{-1}\right)$ is the number of the Bi layers per unit thickness and c is the c axis length. This gives the step size between the successive $1/\rho_{yx}$ plateaus as $1/\rho^0_{yx} = sZ^* \left(e^2/h\right)$, from which we have estimated the degeneracy factor s to be $\sim$ 5 to 6, as shown in Table 4.1 (see also fig. 4.5B).Provided that there exist four valleys in $EuMnBi_2$[126] as is the case of $SrMnBi_2$[41, 66], s should be 8 (including double spin degeneracy). Even having taken into account errors in sample thickness ($\pm$10 to 20%), the s value of 8 is somewhat larger than the estimated one, which may be attributable to the inhomogeneous transport arising from dead layers and/or the imperfect contacts.

From the SdH frequencies in the spin-flop phase, we are capable of estimating the 2D carrier density per Bi layer at 1.4 K to be $n_{2D} = seB_F/h \sim 4.9 \times 10^{12}\mathrm{cm}^{-2}$ assuming $s = 8$, which results in 3D density $n_{3D} = n_{2D}Z^* \sim 4.4 \times 10^{19}$ cm^{-3} (sample #1). This is comparable to that estimated from ρ_{yx} at $\sim$ 20 T: $n_H = B/e\rho_{yx} \sim 2.9 \pm 0.2 \times 10^{19}\mathrm{cm}^{-3}$, where errors arise from the oscillatory component. From the value of residual resistivity ρ_0, we have obtained the mobility $\mu = n_{3D}/e\rho_0 \sim 14,000$ cm^2/Vs at $\sim$ 2 K, which attains a markedly high value despite the transport coupled with the Eu magnetic order.

As shown in Fig. 4.4B, the $N = 2$ Landau level clearly splits into two peaks in the second derivative of resistivity $-\, d^2\rho_{xx}/dB^2$, whereas the splitting for $N = 3$ is barely discernible. This Landau level splitting is likely to be more pronounced for $N = 1$ (at higher fields), supposedly forming a dip structure in ρ_{xx} as well as $-\, d^2\rho_{xx}/dB^2$ around $B_F/B = 1$. Unfortunately, only one of the split Landau levels is accessible for $N = 1$, because the spin-flop phase is terminated at H_c (a spiky peak in $-\, d^2\rho_{xx}/dB^2$; see also Fig. 4.6). With further decreasing temperature down to 50mK, another Landau level splitting appears to evolve (thick arrow in Fig. 4.6). Although the origin of these splittings is unclear at present, it should be relevant to the spin and valley degrees of freedom, as is often the case in the conventional QHE in semiconductor heterostructures [67]. It is surprising that such lifting of spin and

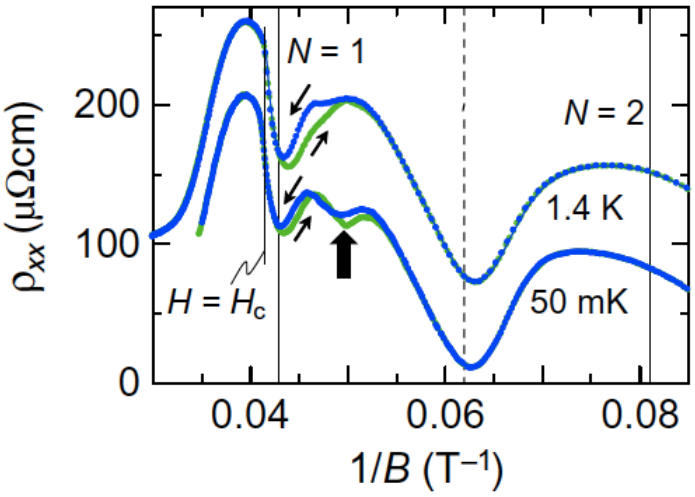

Fig. 4.6 Hysteresis and split of the Landau level. ρ_{xx} as a function of $1/B$ at 50 mK and 1.4 K. The curve at 50 mK is shifted downward for clarity. The arrow denotes the ρ_{xx} valley noticeable at 50 mK. Long solid and dashed lines indicate the integer and half-integer multiple of $B_F/B - \gamma$, respectively. Short solid line denotes the position corresponding to the field $H = H_c$.

valley degeneracy is clearly observed at moderately high fields ($\sim$ 20 T) even in the bulk system. This may be indicative of a large Landé g factor and/or strong electron correlations, characteristic of Dirac fermions formed on the Bi layer[73, 74, 75].

Finally, we mention the hysteretic anomalies in ρ_{xx} and ρ_{zz} around 20 T (Fig. 4.2). It should be noted here that similar hysteretic phenomena of resistivity have been discovered in many 2D electron gas systems in both the regimes of the integer[68, 69] and fractional QHE[70, 71]. Their physical origin is considered to be relevant to the crossing of Landau levels for electrons (or for composite fermions in the fractional QHE) with different spin polarization[72], where magnetic domains are likely to form. In the present compound, because the resistivity shows substantial hysteresis near the transition between the split Landau levels (in the $N = 1$ state as shown in Fig. 4.6), it might originate from the dissipative conduction along such domain walls. Although detailed discussions about its mechanism are beyond the scope of the present study, the observed distinct hysteresis may suggest the possible importance of the spin polarization of Landau level for Dirac fermions.

4.3 Antiferromagnetic structure in the AFM phase

Figures 4.7A-C show resonant x-ray magnetic scattering profiles for $EuMnBi_2$ measured at 5 K at zero magnetic field. In order to study the origin of the (0 0 11) reflection shown in Fig. 4.1B, we performed energy scans near the Eu L_3 absorption edge (Fig. 4.7A). A single peak, suggesting the resonant nature of the reflection, was

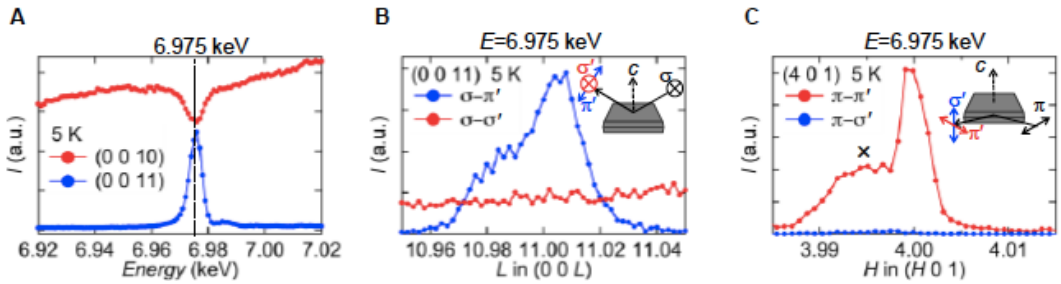

Fig. 4.7 Resonant x-ray magnetic scattering for $EuMnBi_2$ near the Eu L_3 absorption edge. (A) Energy scans at the (0 0 10) Bragg reflection and (0 0 11) magnetic reflection with σ-incident polarization. (B), (C) Polarization analysis of the (0 0 11) and (4 0 1) magnetic reflections at 5 K at 6.975 keV. The broad peak denoted by $\times$ arises from an unknown powder line. Experimental setup is shown schematically in each inset.

found at 6.975 keV, which arises from dipole resonant scattering involving transitions from the core $2p$ state to the empty $5d$ one[76]. The $5d$ state should be polarized via the onsite $4f - 5d$ mixing due to the locally broken inversion symmetry by crystal field at the Eu site.

Additionally, the magnetic origin of the (0 0 11) reflection was evidenced by polarization analysis (Fig. 4.7B). The magnetic form factor (f_i^{mag}) of the ith Eu magnetic moment in the electric-dipole transition is described as

$$f_i^{mag} \propto (\boldsymbol{e} \times \boldsymbol{e'}) \cdot \boldsymbol{M}_i \ , \tag{4.2}$$

where $\boldsymbol{e}$ and $\boldsymbol{e'}$ denote unit vectors of the incident and scattered polarization, respectively, and $\boldsymbol{M}_i$ denotes the direction of the ith Eu magnetic moment[77]. In the current experimental configuration, magnetic scattering contributes only to the rotated $\sigma - \pi'$ channel, while charge scattering contributes to the unrotated $\sigma - \sigma'$ channel. As shown in Fig. 4.7B, the (0 0 11) reflection was observed in the $\sigma - \pi'$ channel but not in the $\sigma - \sigma'$ channel, which suggests the magnetic origin of this reflection.

In order to determine the orientation of the Eu magnetic moments, we performed polarization analysis for the (4 0 1) magnetic reflection. Since the π-incident polarization is nearly parallel to the ab plane in measuring this reflection (Inset to Fig. 4.7C), the magnetic scattering by the c (ab) component of the magnetic moments should be observed in the $\pi - \pi'$ ($\pi - \sigma'$) channel. As shown in Fig. 4.7C, magnetic reflection was detected in the $\pi - \pi'$ channel but not in the $\pi - \sigma'$ channel, which suggests that the Eu magnetic moments are aligned along the c axis at 5 K at zero magnetic field. This result is consistent with the magnetization data for the AFM the phase (see Figs. 4.1A and 4.2A in the main text).

Next, we discuss the magnetic structure of $EuMnBi_2$. From the observation of the (0 0 11) and (4 0 1) magnetic reflections, the magnetic order of Eu sublattice

A

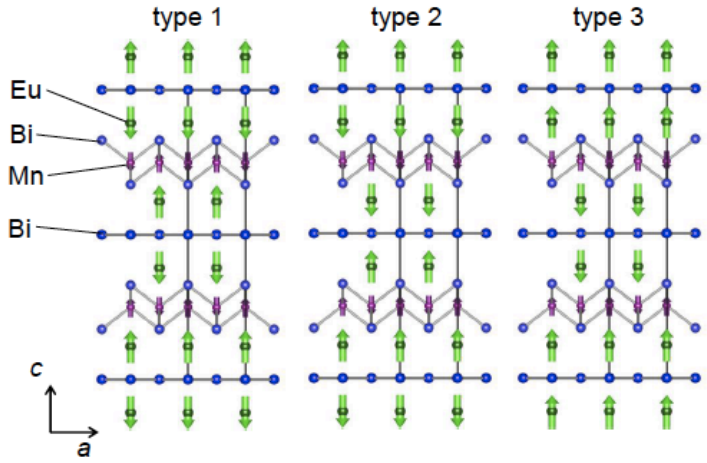

B

	type 1	type 2	type 3
(0 0 11) (4 0 1)	×	○	○
(3 0 0)	×	×	○

Fig. 4.8 (A) Three types of Eu moment arrangement at 5 K. (B) Extinction rule obtained by calculating I_{calc} for each magnetic structure. Allowed and forbidden reflections are denoted by ∘ and ×, respectively.

is characterized by a (001) reciprocal vector, which indicates that the Eu magnetic moments order ferromagnetically within the *ab* plane and antiferromagnetically along the *c* axis. However, there remain three types of stacking sequences of ferromagnetic layers along the *c* axis, as depicted in Fig. 4.2A. In the following, we show that type 2 in Fig. 4.1A is the most plausible, based on the comparison between the calculations and experimental data. The intensity of magnetic scattering I_{calc} is expressed as

$$I_{calc} = \left| \sum_i e^{i\boldsymbol{q}\cdot\boldsymbol{r}_i} f_i^{mag} \right|^2 = \left| (\boldsymbol{e} \times \boldsymbol{e}') \cdot \sum_i e^{i\boldsymbol{q}\cdot\boldsymbol{r}_i} \boldsymbol{M}_i \right|^2 , \tag{4.3}$$

where $\boldsymbol{r}_i$ is the position of the ith Eu site taken from Ref. [44] and f_i^{mag} is the magnetic form factor of the ith Eu moment given in Eq. 4.3. Considering the extinction rules obtained by calculating I_{calc} for the three types of magnetic order (Fig. 4.8B), the observation of (0 0 11) magnetic reflection suggests that the structures type 2 and type 3 remain as possible candidates. On the other hand, no signal was observed at around (3 0 0) (Fig. 4.9B), which suggests that only the structure type 2 satisfies the extinction rules. In addition, we have measured the intensities (I_{obs}) of several (0 0 L)

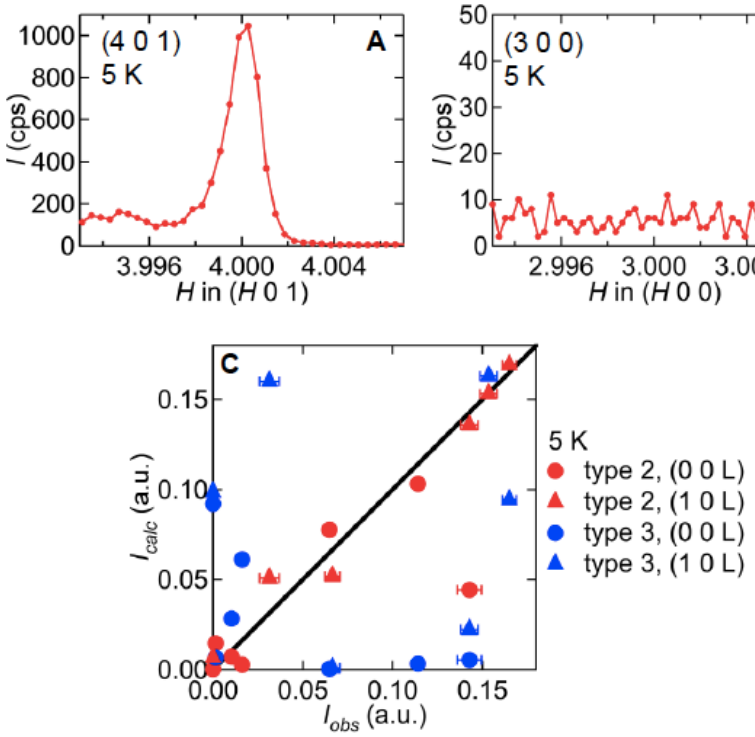

Fig. 4.9 Determination of magnetic structure of Eu sublattice for $EuMnBi_2$. (A, B) Scans around the (4 0 1) and (3 0 0) reflections at 5 K at 6.975 keV with π-incident polarization. (C) Comparison between the observed (I_{obs}) and calculated (I_{calc}) intensities of the (0 0 L = odd) and (1 0 L = even) magnetic reflections at 5 K.

(L = odd) and (1 0 L) (L = even) magnetic reflections and compared them with the calculated intensities I_{calc} for type 2 and type 3 (Fig. 4.9C). Measured intensities are in excellent agreement with the calculation results for type 2, which again supports type 2 as the most probable Eu moment arrangement.

4.4 Magnetic properties of $EuZnBi_2$

As shown in Fig. 4.10A, the magnetic susceptibility (M/H) for $EuZnBi_2$ steeply drops below T_N ($\sim$ 20 K) for H|| [100], whereas it is almost constant below T_N for H|| [001]. This indicates that the Eu moments are oriented perpendicular to the c axis in the AFM phase at 0 T for $EuZnBi_2$, in contrast to $EuMnBi_2$. The magnetization almost linearly increases with increasing field for both H|| [100] and H|| [001], whereas we observed a weak anomaly around 1 T in the profile for H|| [110] (Fig. 4.10B), which suggests the Eu moments tend to be oriented parallel to the [110] direction in the AFM phase due to a weak anisotropy within the ab plane. To study the AFM arrangement for $EuZnBi_2$, we have measured the resonant x-ray magnetic scattering

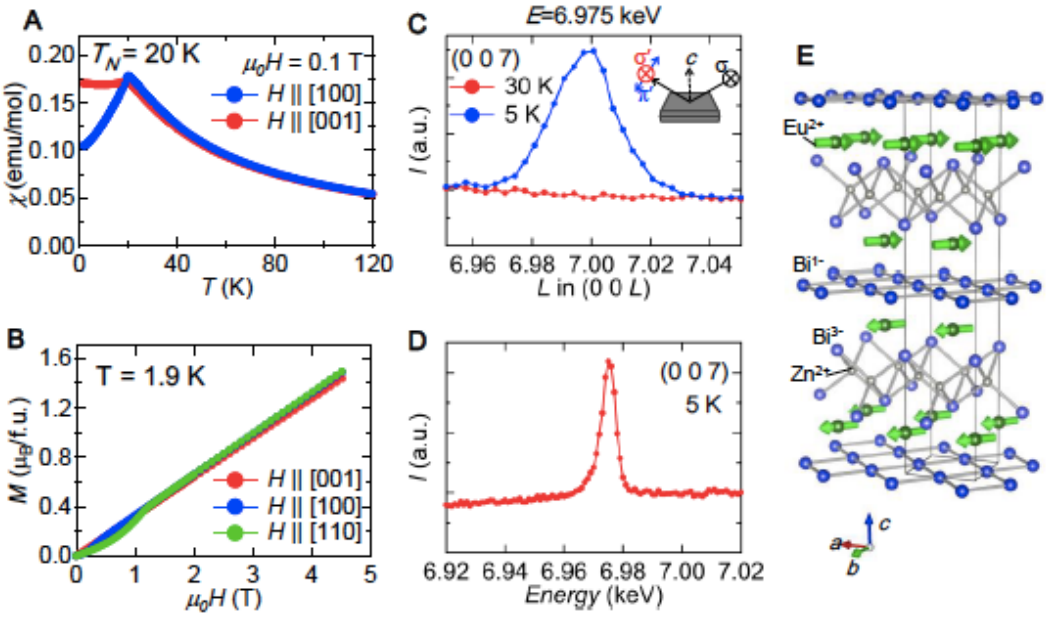

Fig. 4.10 Magnetization and resonant x-ray magnetic scattering near the Eu L_3 absorption edge for $EuZnBi_2$. (A) Temperature profile of magnetic susceptibility along [001] (red symbols) and [100] (blue) measured at 0.1 T. (B) Field profiles of magnetization for along [001] (red), [100] (blue) and [110] (green) at 1.9 K. (C) Profile of the (0 0 7) magnetic reflection along [001] at 6.975 keV at 5 K (below T_N) and 30 K (above T_N). The inset shows schematic illustration of the measurement configuration. (D) Energy profile of the (0 0 7) magnetic reflection at 5 K. (E) Schematic illustration of the plausible magnetic structure for $EuZnBi_2$ at 0 T.

at $E = 6.975$ keV (near the Eu L_3 absorption edge). We clearly observed the (0 0 L) (L = odd) magnetic reflections below T_N, in analogy with $EuMnBi_2$. As a typical example, Figs. 4.10C and 4.10D present the profiles of the (0 0 7) reflection along [001] at 5 K (below T_N) and 30 K (above T_N), and its energy scan at 5 K, respectively. The overall features are quite similar to those observed in $EuMnBi_2$. Based on these data, we can naturally assume that $EuZnBi_2$ hosts the same AFM stacking sequence along the c axis as $EuMnBi_2$ (type 2 in Fig. 4.8), which results in the AFM order shown in Fig. 4.10E as a plausible model at 0 T. There the magnetic structure of the Eu sublattice is analogous to those in the spin-flop AFM phase for $EuMnBi_2$.

4.5 Summary for Chap.4

In this chapter,, we have presented a marked tuning of magnitude in inter-layer conduction of quasi-2D Dirac fermions, utilizing the AFM order of Eu moments. In addition to the staggered moment alignment along the c axis, the field-induced flop of

the Eu moment direction appears to further reduce the interlayer coupling and hence confine the Dirac fermions within the constituent 2D Bi layer well enough to quantize the Hall conductivity in a bulk form. Such a magnetically active Dirac fermion system would form a promising class of spintronic materials with very high mobility.

Chapter 5

Investigation of the coupling between Dirac fermion and magnetism in $EuMnBi_2$

5.1 Magnetic structure of $EuMnBi_2$

Among the magnetic Dirac materials, $EuMnBi_2$ is a rare compound that exhibits quantum transport of Dirac fermions coupled with the field-tunable magnetic order[43]. $EuMnBi_2$ has a layered structure consists of Bi square nets hosting two-dimensional Dirac fermion and the insulating layers hosting magnetic Eu^{2+} and Mn^{2+} ions as shown in Fig. 5.1(a, b). In this system, the magnetic order of the Eu sublattice is modulated by the temperature and the external magnetic field ($H||c$) as shown in Fig. 5.1(c). The magnetic order highly enriches the quantum transport properties of the Dirac fermion. Namely, the interlayer conduction is dramatically suppressed in the field-induced spin-flop AFM (SF) phase, leading to the giant magnetoresistance effect in the interlayer resistivity ρ_{zz}. Furthermore, the enhanced two-dimensionality leads to the multilayer quantum Hall effect in a bulk crystal, which is signified by the giant SdH oscillations and the plateau-like structures in the Hall resistivity. However, detailed mechanisms of the coupling between the magnetic order and the Dirac fermion remain unclear.

In order to reveal the coupling between the quantum transport of the Dirac fermion and the magnetic order in $EuMnBi_2$, detailed information on the magnetic structure is indispensable. In the previous report we derived a probable antiferromagnetic structure of the Eu sublattice for the AFM phase by the resonant x-ray magnetic diffraction measurements[43]. The magnetic structure of the Mn sublattice, which shows antiferromagnetic order below $T_N(\mathrm{Mn}) \sim 315$ K[44], is suggested to be the same as in isostructural $SrMnBi_2$[45], although no direct evidence is reported so far. The magnetic structure for the SF phase is not investigated, although the Eu moments

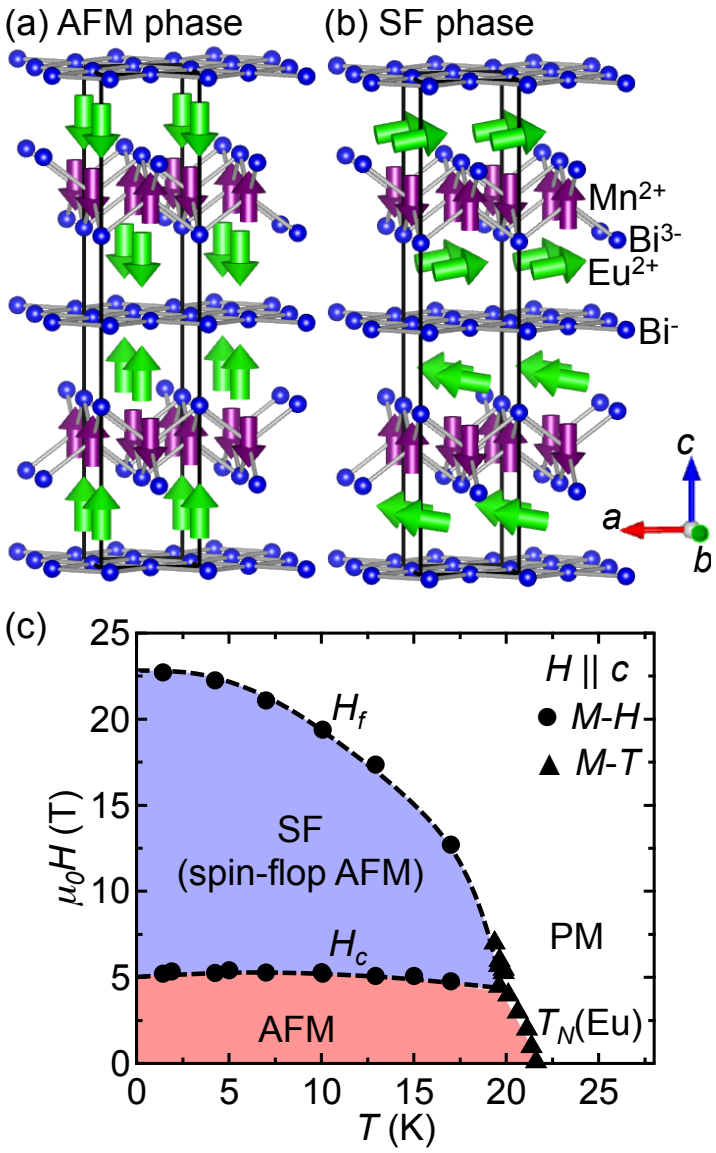

Fig. 5.1 (a, b) Antiferromagnetic structures in $EuMnBi_2$ for the AFM (3 K, 0 T) and SF (3 K, 6 T, $a-$domain) phases, respectively. The magnetic structures were obtained by the present work, while the atomic positions were reproduced from Ref. [44]. The crystallographic unit cell is shown by the solid lines. (c) Magnetic phase diagram of the Eu sublattice as functions of magnetic field ($H||c$) and temperature. Note that the Mn moments show antiferromagnetic order below T_N(Mn) $\sim$ 315 K. Reproduced from Ref. [43] for readability.

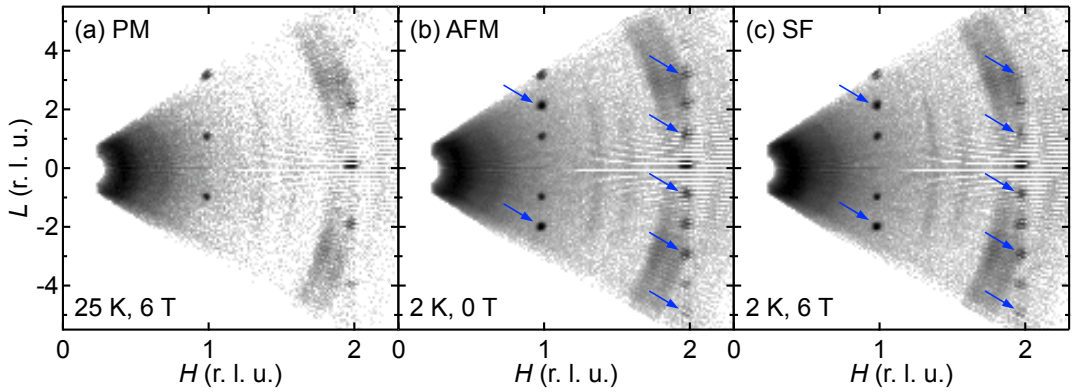

Fig. 5.2 Single-crystal neutron diffraction intensity distributions of $EuMnBi_2$ on the (H 0 L) reciprocal lattice planes for the (a) PM (25 K, 6 T), (b) AFM (2 K, 0 T) and (c) SF (2 K, 6 T) phases, respectively. The blue arrows in (b, c) indicate the Eu magnetic reflections that satisfy the conditions of $H + K + L =$ odd, $L \neq 0$. The ring-like intensities correspond to the powder lines which may arise from aluminum in the sample holder or bismuth flux stuck to the crystal surfaces.

are suggested to be reoriented to be perpendicular to the c axis. Furthermore, the magnetic arrangement of the Mn sublattice is possibly modulated by the interaction between the Eu and Mn moments in the SF phase. The focus of the present research is to reveal the antiferromagnetic structure of both the Eu and Mn sublattices with particular focus on the SF phase,utilizing the single crystal neutron and resonant x-ray magnetic diffraction measurements under magnetic fields.

5.1.1 Neutron diffraction profiles

Figures 5.2(a-c) show the neutron diffraction intensity distributions on the (H 0 L) reciprocal lattice plane in the PM (25 K, 6 T), AFM (2 K, 0 T) and SF (2 K, 6 T) phases. The obtained lattice parameters for the AFM phase were $a = 4.4988(2)$ Å and $c = 22.799(10)$ Å, which are comparable to those estimated from the powder x-ray diffraction[43].

In the PM phase, a sufficient number of reflections were observed under the condition of $H + K + L =$ even, which follows the extinction rule of $I4/mmm$ symmetry of the crystal. No superlattice reflection was observed, although the Mn moments are ordered antiferromagnetically below $T_N(\mathrm{Mn}) \simeq 315$ K. This result suggests that the magnetic reflections from the Mn moments are superposed on the nuclear Bragg reflections and also follow the condition of $H + K + L =$ even. Measurements at the temperatures above $T_N(\mathrm{Mn})$ is not performed in the present research.

The Mn antiferromagnetic arrangement for the PM phase is derived as follows. The integer diffraction indices HKL of the Mn magnetic reflections reveal that the

magnetic arrangement of the Mn sublattice is described by the propagation vector of $\boldsymbol{q} = (0, 0, 0)$. Mn magnetic reflections follow the condition of $H + K + L =$ even, indicating that the body-centered translation symmetry of the crystal is retained by the Mn magnetic order. It follows that among the four Mn sites in a unit cell, two sites related by the body-centered translation (*e.g.* (1/2, 0, 1/4) and (0, 1/2, 3/4); see Fig. 5.1[a]) host Mn moments parallel to each other.

Furthermore, magnetization measurements imply the Mn antiferromagnetic order with the Mn moments parallel to the c axis below T_N(Mn)[44]. These considerations indicate the checkerboard-type AFM order as shown in Fig. 5.1(a) with an antiferromagnetic arrangement for both the in-plane and out-of-plane nearest neighbors.This magnetic arrangement is the same as that in isostructural $SrMnBi_2$[45].

In the AFM phase (Fig. 5.2[b]), superlattice reflections from the Eu magnetic moments were observed at the positions of $H + K + L =$ odd, $L \neq 0$. This result is consistent with the previous results of the x-ray resonant magnetic diffraction measurements[43]. The integer diffraction indices HKL of the Eu magnetic reflections reveal that the magnetic arrangement of the Eu sublattice is also described by the propagation vector of $\boldsymbol{q} = (0, 0, 0)$. The violation of the extinction rule means that the Eu antiferromagnetic order breaks the body-centered translation of the crystal. Therefore among the four Eu sites in a unit cell, two sites related by the body-centered translation, *e.g.* (0, 0, $+z_0$) and (1/2, 1/2, 1/2 + z_0), $z_0 \sim 0.11$[44], host Eu moments antiparallel to each other. Furthermore, the absence of $L = 0$ Eu magnetic reflections indicate that two Eu sites facing across the Bi square net layer, *e.g.* $(0, 0, +z_0)$ and $(0, 0, -z_0)$, host Eu moments antiparallel to each other. Above considerations indicate the antiferromagnetic arrangement as shown in Fig. 5.1(a), where the Eu moments order ferromagnetically within the ab plane and align antiferromagnetically along the c axis in the sequence of up-up-down-down[43].

The diffraction intensity distribution for the SF phase (Fig. 5.2[c]) is qualitatively similar to that for the AFM phase, suggesting that the magnetic arrangement for the SF phase is similar to that for AFM phase except for the orientations of the magnetic moments. Figures 5.3(a) and (b) show the integrated intensities of the (1 0 L) ($-2 \leq L \leq 3$) and (0 1 L) ($-3 \leq L \leq 2$) reflections, respectively, in the PM, AFM and SF phases. Reflections of $L =$ odd, i.e. $H + K + L =$ even, arising from the nuclear and Mn magnetic reflections show comparable intensities in PM, AFM and SF phases. This result imply that the Mn moments show similar magnetic structures in three phases, which will be discussed more quantitatively in Sec. 5.1.3. On the other hand, intensities of the $L =$ even Eu magnetic reflections in the SF phase are significantly smaller than that in the AFM phase. In the AFM phase, intensities of the (1 0 $\pm$2) and (0 1 $\pm$2) Eu magnetic reflections are comparable to each other, indicating that the Eu moments are aligned parallel to the c axis and the four-fold rotational symmetry along the c axis of the crystal is retained. In the SF phase, on the other hand, intensities of the (1 0 $\pm$2) Eu magnetic reflections are significantly larger than those of the (0 1 $\pm$2) reflections. These results are interpreted in terms

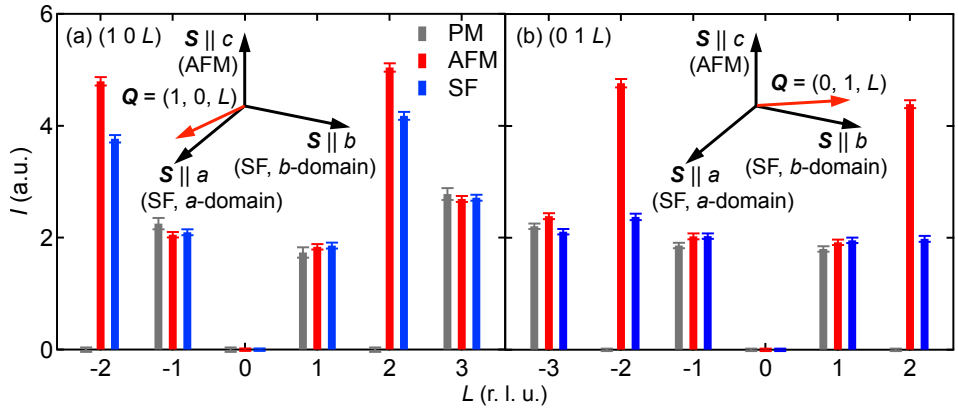

Fig. 5.3 Integrated intensities of the (a) (1 0 L) ($-3 \leq L \leq 2$) and (b) (0 1 L) ($-2 \leq L \leq 3$) reflections in the AFM (2 K, 0 T), SF (2 K, 6 T) and PM (25 K, 6 T) phases. Each inset show the schematic descriptions of the directions of the scattering vectors $\boldsymbol{Q} = (0, 1, L)$ and $(1, 0, L)$ ($L \simeq 2$), along with the directions of the Eu moments $\hat{\boldsymbol{S}}$ in the AFM and SF phases.

of the reorientation of the Eu moments to the a or b directions in the SF phase.

The neutron magnetic diffraction intensities arise from the component of the magnetic moments perpendicular to the scattering vector $\boldsymbol{Q}$. Since $\boldsymbol{Q} = (1, 0, \pm 2)$ is nearly parallel to the a axis as shown in the inset of Fig. 5.3(a), the (1 0 $\pm$2) magnetic reflections mainly arise from the c and b component of the Eu moments. Similarly, the (0 1 $\pm$2) reflections arise from the c and a component of the Eu moments (inset to Fig. 5.3[b]). Eu moments are aligned parallel to the c axis in the AFM phase, arising the large and comparable intensities of the (1 0 $\pm$2) and (0 1 $\pm$2) Eu magnetic reflections. In the SF phase intensities of the (1 0 $\pm$2) magnetic reflections are larger than those of the (0 1 $\pm$2) reflections, indicating that the major number of Eu moments are oriented along the b direction and the others are oriented along the a direction. This implies that in the SF phase, 2 types of domains exist where Eu moments are aligned parallel to the a and b axis (mentioned as $a-$ and $b-$domains in the following), and the $b-$domain is somewhat dominant. The $b-$domain is likely favored due to the small misalignment of the magnetic field away from the c axis[]. Quantitative estimate of the domain population is given in Sec. 5.1.3.

5.1.2 Resonant x-ray magnetic diffraction

The different orientation of the Eu moments in the AFM and SF phases are also signified by the resonant x-ray magnetic reflection measurements. (4 0 1) Eu magnetic reflection was observed at the Eu L_3 absorption edge ($E = 6.975$ keV) in the AFM phase (5 K, 0 T) as shown in Fig. 5.4(a). The (4 0 1) reflection was not observed for the non-resonant x-ray ($E = 7$ keV), supporting the resonant nature of the (4 0 1)

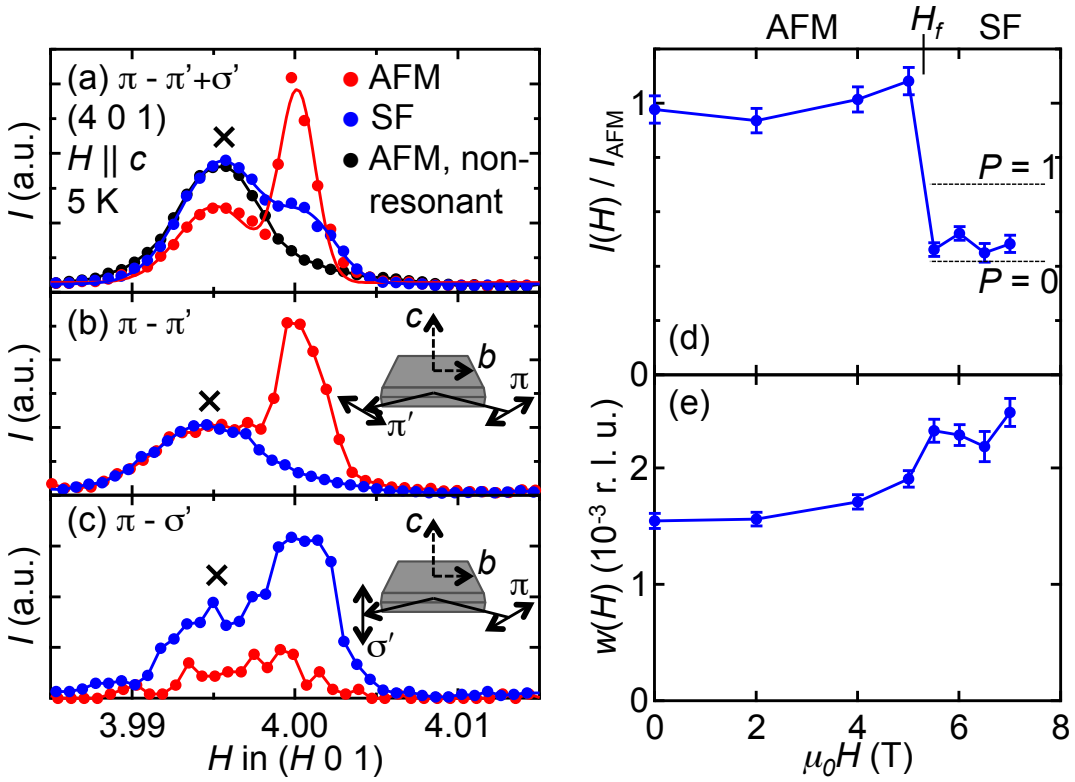

Fig. 5.4 (a) Peak profiles of the (4 0 1) resonant x-ray reflection along [1 0 0] at Eu L_3 edge (E = 6.975 keV) for the AFM (5 K, 0 T) and SF (5 K, 7 T) phases[43]. Peak profile at non-resonance (E = 7 keV) for the AFM phase is also shown. The broad peak denoted by × arises from an unknown powder line. The inset shows the schematic configurations for the measurements. (b, c) Peak profiles of the (4 0 1) resonant x-ray magnetic reflection in the (b) $\pi - \pi'$ and (c) $\pi - \sigma'$ channels, respectively. Schematic configurations for the measurements are shown in each inset. (d, e) Magnetic field dependence of the normalized intensity and the FWHM along [1 0 0] of the (4 0 1) resonant x-ray magnetic reflection. I_{AFM} is the averaged intensity for the AFM phase at 5 K. The vertical dashed line denote $H_f \simeq 5.3$ T, the transition field from the AFM phase to the SF phase[43]. The horizontal lines in (d) indicate the ratio of the intensities for the SF and AFM phases $I_{\mathrm{SF}}/I_{\mathrm{AFM}}$ calculated using Eq. 5.2 for fully polarized spin-flop domains ($P = 0$ or $P = 1$).

Eu magnetic reflection. The (4 0 1) magnetic reflection was also observed in the SF phase with a lower intensity than that in the AFM phase, indicating the reorientation of the Eu moments.

In order to determine the orientation of the Eu moments, we performed the polarization analysis for the magnetic reflection. The (4 0 1) magnetic reflection was observed in the $\pi - \pi'$ channel for the AFM phase, while it was observed in the $\pi - \sigma'$ channel for the SF phase (Fig. 5.4[b, c]). The magnetic form factor f^{mag} of the Eu magnetic moment $\boldsymbol{M}$ in the electric-dipole transition is given as

$$f^{mag} \propto (\hat{\boldsymbol{e}} \times \hat{\boldsymbol{e}}') \times \hat{\boldsymbol{M}} \tag{5.1}$$

, where $\hat{\boldsymbol{e}}$ and $\hat{\boldsymbol{e}}'$ are the unit vectors of the incident and scattered polarization respectively. Eq. 5.1 shows that the resonant x-ray magnetic reflection arises from the component of the magnetic moment $\boldsymbol{M}$ perpendicular to both $\hat{\boldsymbol{e}}$ and $\hat{\boldsymbol{e}}'$. As seen from the inset to Fig. 5.4(b), observation of the magnetic reflection in the $\pi - \pi'$ channel for the AFM phase reveals that the Eu moments are parallel to the c axis.On the other hand, observation of the magnetic reflection in the $\pi - \sigma'$ channel for the SF phase reveals that the Eu moments are pependicular to the c axis in the SF phase (see the inset to Fig. 5.4[c]).

Figures 5.4(d, e) show the magnetic field dependence of the intensity and the FWHM along [1 0 0] of the (4 0 1) resonant x-ray magnetic reflection. The reflection intensity shows a sharp drop at $H_f \sim 5.3$ T due to the spin-flop transition. Ratio of the averaged intensities for the AFM phase (0, 2, 4, 5 T) and that for the SF phase (5.5, 6, 6.5, 7 T) was $I_{\mathrm{SF}}/I_{\mathrm{AFM}} = 0.482(19)$. Utilizing Eq. 5.1, this ratio is calculated as

$$\frac{I_{\mathrm{SF}}}{I_{\mathrm{AFM}}} \simeq \frac{P}{4\cos^2\theta} + \frac{1-P}{4\sin^2\theta} \tag{5.2}$$

Here, $\theta \simeq 52^\circ$ is the scattering angle, and P is the population of the $a-$domain. The angle between the scattering plane and the ab plane ($\sim 3^\circ$) is neglected. Eu moments are assumed to align parallel to the c axis in the AFM phase, a and b axis for the $a-$ and $b-$domains respectively in the SF phase. Comparing this formula and the observed ratio, the domain ratio is evaluated as $P = 0.31(8)$. The FWHM of the (4 0 1) magnetic reflection slightly increases above $H_f \sim 5.3$ possibly due to small spin-flop domains in the SF phase.

5.1.3 Quantitative analysis on the neutron diffraction data

We have qualitatively discussed the results of the neutron diffraction and the resonant x-ray diffraction. The Mn magnetic structures for the PM and AFM phases and the Eu magnetic structures for the AFM and SF phases were revealed. Here, the quantitative analysis on the neutron diffraction intensities is presented, with a particular focus on the Mn magnetic structure for the SF phase.

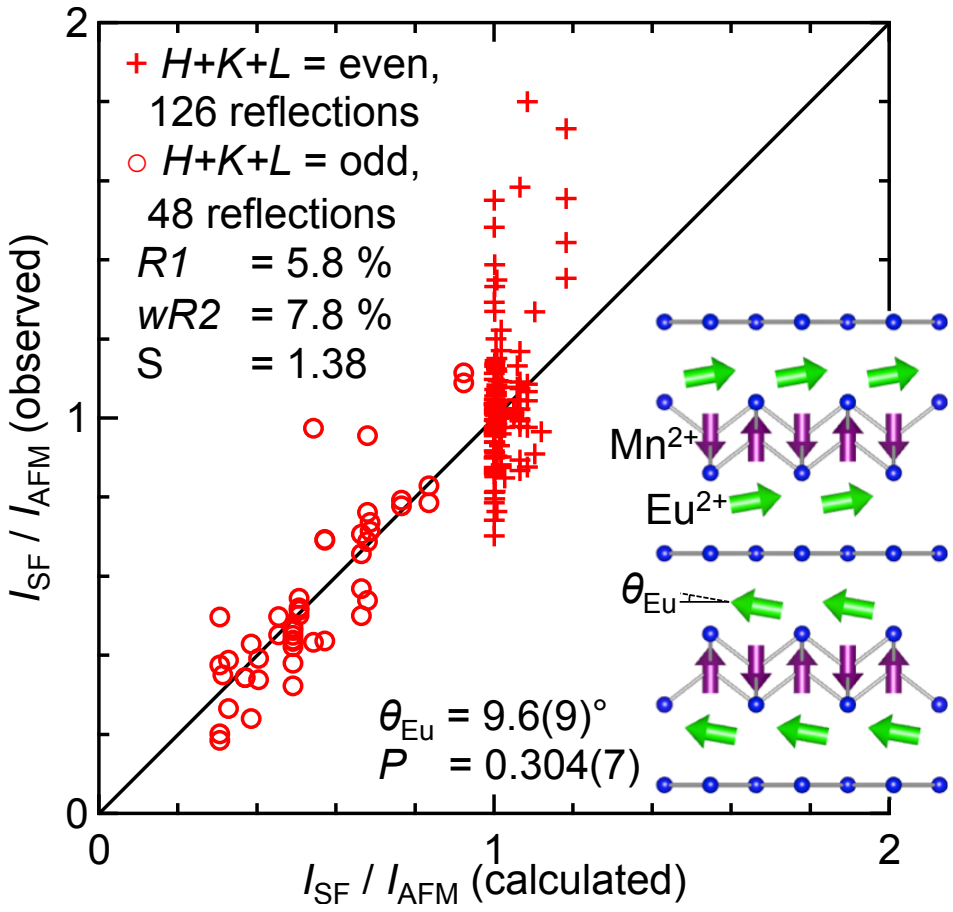

Fig. 5.5 Comparison between the observed and calculated ratio of the intensities for the SF and AFM phases in $EuMnBi_2$. Inset depicts the magnetic structure for the SF phase, along with the definition of θ_{Eu}.

The neutron diffraction intensities were corrected for several crystal orientations in the PM, AFM and SF phases. The observed ratios of the intensities in the SF and AFM phases I_{SF}/I_{AFM} are plotted against the calculated ones in Fig. 5.5. Here, the magnetic structure for the AFM phase as shown in Fig. 5.1(a) was assumed based on the discussions in Sec. 5.1.1. For the SF phase, Eu moments are assumed to be canted by θ_{Eu} from the a (population P) or b $(1-P)$ directions to the direction of the magnetic field (inset to Fig. 5.5). As we discussed in Sec. 5.1.1 the Mn magnetic structure for the SF phase is not dramatically different from those for the PM and AFM phases. Therefore the Mn magnetic structure for the SF phase was first assumed to be the same as that for the AFM phase, and then was assumed to be slightly modulated by the interaction with Eu moments. The crystal structure parameters were also fixed to the literature value[44]. The amplitude of the Eu magnetic moment M_{Eu} was fixed to 6.4 μ_B, the high-field saturated magnetization value of $EuMnBi_2$ at 1.4

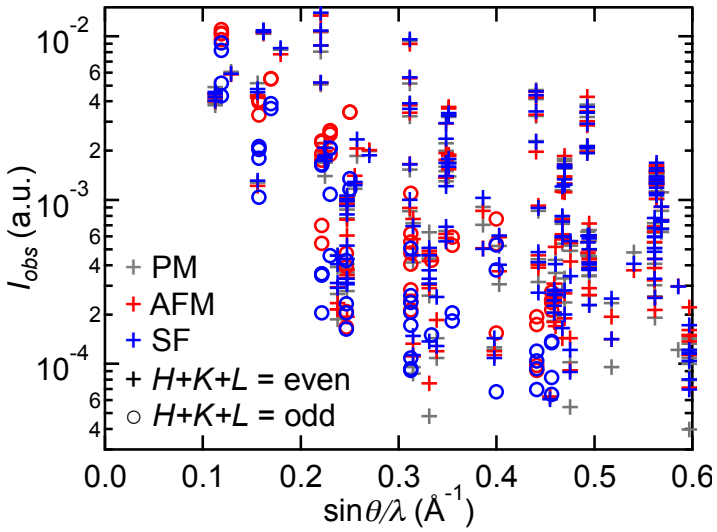

Fig. 5.6 Observed neutron reflection intensities as a function of $\sin\theta/\lambda$, which is proportional to the magnitude of the scattering vector $|\boldsymbol{Q}|$. Eu magnetic reflections under the condition of $H + K + L =$ odd rapidly decreased their intensities with increasing $\sin\theta/\lambda$ and were not observed in the range of $\sin\theta/\lambda > 0.5$ Å^{-1}. This behavior reflects the decrease in the magnetic form factor $f_{\mathrm{Eu}}(\boldsymbol{Q})$ with increasing $|\boldsymbol{Q}|$. Therefore the reflection intensities in the range of $\sin\theta/\lambda > 0.5$ Å^{-1} are not informative of the magnetic structure and were not used for the qualitative analysis, where the atomic positions were fixed to the literature value.

K[43]. The amplitude of the Mn magnetic moment M_{Mn} was also fixed to 3.4 μ_{B}, the amplitude of the Mn magnetic moment in isostructural $SrMnBi_2$ deduced from the neutron diffraction experiment[45]. The magnetic form factors of Eu and Mn were assumed to be $Eu^{2+}\langle j_0\rangle$ and $Mn^{2+}\langle j_0\rangle$ respectively. Two parameters, P and θ_{Eu}, were refined using 126 reflections under the condition of $H + K + L =$ even and 48 reflections under the condition of $H + K + L =$ odd that satisfy $\sin\theta/\lambda < 0.5$ Å^{-1} and $I > 3\sigma$ (see Fig. 5.6 for details).

As shown in Fig. 5.5 relatively good agreement between the observed and calculated $I_{\mathrm{SF}}/I_{\mathrm{AFM}}$ was obtained, with the reasonable reliable factors $R1$ =5.8%, $wR2$ =7.5% and the goodness of fit $S = 1.38$. The refined domain population $P = 0.304(7)$ indicates sufficient dominance of the $b-$domain over the $a-$ domain in the SF phase, which is likely due to the misalignment of the magnetic field away from the c axis. The refined canted angle of the Eu moments $\theta_{\mathrm{Eu}} = 9.6(9)^\circ$ indicates the net magnetization of $M_{\mathrm{Eu}}\sin\theta_{\mathrm{Eu}} = 1.06(10)$ μ_{B}/Eu, which is in rough agreement with the magnetization of 1.6 μ_{B}/f.u observed at 1.4 K, 6 T[43].

It should be noted here that the intensity ratios for the SF and AFM phases $I_{\mathrm{SF}}/I_{\mathrm{AFM}}$, rather than the intensities itself, were used for the quantitative analysis in order to avoid the effect of strong neutron absorption by Eu. Since the neutron

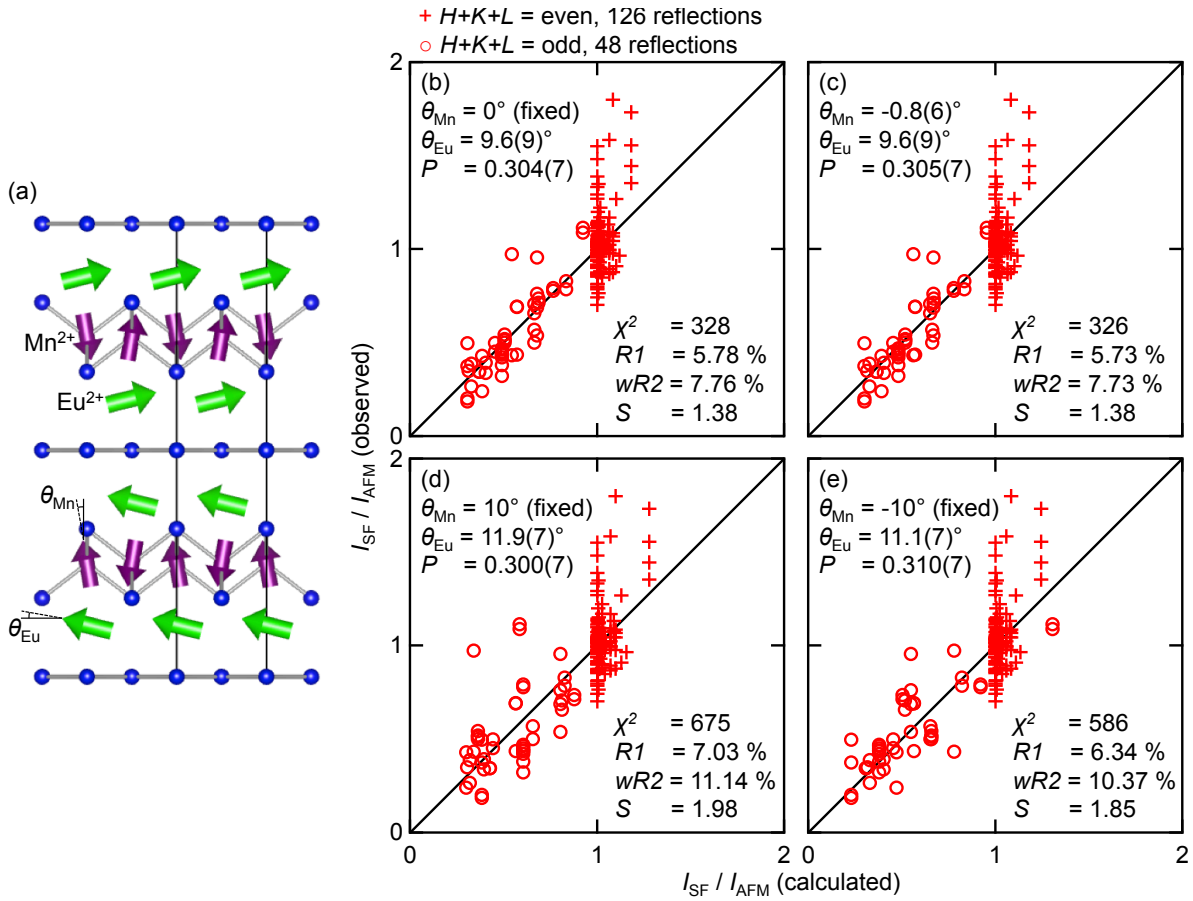

Fig. 5.7 (a) Schematic description of the antiferromagnetic structure in the SF phase of $EuMnBi_2$, where the Mn moments are assumed to be canted parallel to the adjacent Eu moments. The definitions of $\theta_{\rm Eu}$ and $\theta_{\rm Mn}$ are also shown. (b-e) Comparison between the observed and calculated ratio of the intensities for the SF and AFM phases in $EuMnBi_2$. $\theta_{\rm Mn}$ is (b) fixed to 0° (same as Fig. 5 in the main text), (c) refined, (d) fixed to 10° and (e) fixed to −10° during the refinement, respectively.

absorption cross section is independent of the external magnetic field or the magnetic structure, $I_{\rm SF}/I_{\rm AFM}$ is in principle unaffected by the neutron absorption when $I_{\rm AFM}(\boldsymbol{Q})$ and $I_{\rm SF}(\boldsymbol{Q})$ were measured in the same crystal configuration. Analysis using the reflection intensities by applying the absorption correction is not performed due to the limited $\boldsymbol{Q}$−window by the superconducting magnet in the present experiment.

We further proceeded our analysis by assuming the magnetic structure for the SF phase, where the Mn moments are canted to the in-plane direction due to the interaction between the Eu and Mn moments (Fig. 5.7[a]).

Here, the magnetic structure of the Mn moments for the SF phase is examined in

detail. It is likely that some interaction exist between the Eu moments and the Mn moments in $EuMnBi_2$. Due to this interaction, the reorientation of the Eu moments may have some influence on the Mn magnetic structure for the SF phase. In Fig. 5.5, we assumed that the Mn magnetic structure for the SF phase is the same as that for the AFM phase and obtained a relatively good agreement between the observed and calculated intensity ratio $I_{\mathrm{SF}}/I_{\mathrm{AFM}}$. Although this suggests that the Mn magnetic structure for the SF phase is not dramatically changed from that for the AFM phase, the possibility exists that there is a slight change. Here, we first consider how the interaction between the Eu and Mn moments can influence the Mn magnetic structure, based on the crystal structure and the magnetic structure of the Eu and Mn moments. Based on that consideration, we create a magnetic structure model for the SF phase and perform the quantitative analysis of the neutron diffraction intensity ratio $I_{\mathrm{SF}}/I_{\mathrm{AFM}}$.

Each Mn site has four nearest neighbor Eu sites, and the Eu moments of those sites are all oriented in the same direction in the AFM and SF phases (see Fig. 1 in the main text). Therefore, as a result of the interaction with the Eu moments, Mn moments are considered to be under a mean field parallel or antiparallel to the surrounding Eu moments. Especially in the SF phase, since this mean field is parallel to the a or b direction, it is expected that the Mn moments will be slightly canted in that direction. As a result, is is expected that the magnetic structure shown in Fig. 5.7(a) is realized in the SF phase, where the Mn moments are canted parallel or antiparallel to the surrounding Eu moments. Here, θ_{Mn} is the cant angle of the Mn moments, and $\theta_{\mathrm{Mn}} = 0^\circ$ correspond to the case where the Eu-Mn interaction is neglected (same as the inset to Fig. 5 in the main text). $\theta_{\mathrm{Mn}} > 0^\circ$ and $\theta_{\mathrm{Mn}} < 0^\circ$ should be realized when the Eu-Mn interaction is ferromagnetic or antiferromagetic, respectively.

Utilizing this magnetic structure model, we performed the quantitative analysis of the neutron diffraction intensity ratio I_{SF}/I_{AFM} (Fig. 5.7[c]). The obtained $\theta_{\mathrm{Mn}} = -0.8(6)^\circ$ is small and the agreement between the observed and calculated I_{SF}/I_{AFM} did not show significant improvement compared to that obtained when θ_{Mn} is fixed to 0° (Fig. 5 in the main text; reproduced in Fig. 5.7[b]). Furthermore, when θ_{Mn} is fixed to $\pm 10^\circ$, the agreement between the observed and calculated I_{SF}/I_{AFM} was significantly worsened (Fig. 5.7[d, e]). These result reveal that θ_{Mn} is equal to 0° and the Mn magnetic structure in the SF phase is the same as that in the AFM phase within the experimental accuracy. This is probably because the interaction between the Eu moments and the Mn moments is much weaker than that between the Mn moments.

5.1.4 Summary for Chap. 5.1

In summary, we have presented an investigation of the magnetic structure in $EuMnBi_2$ by the single crystal neutron diffraction and the resonant x-ray magnetic diffraction

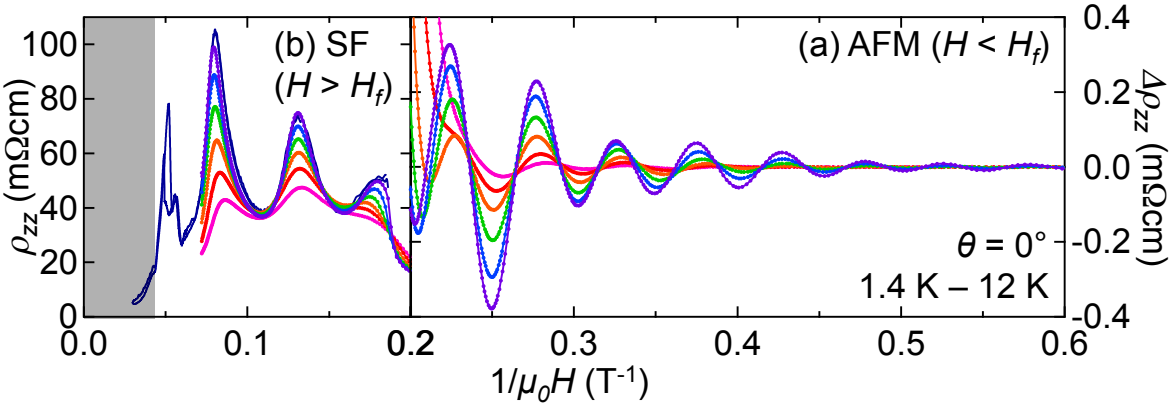

Fig. 5.8 (a) Interlayer resistivity ρ_{zz} as a function of inverse magnetic field $1/\mu_0 H$ along the c axis for the SF (spin-flop AFM) phase ($H > H_f$) at selected temperatures. (b) Oscillatory interlayer resistivity $\Delta\rho_{zz}$ as a function of $1/\mu_0 H$ for the AFM phase ($H < H_f$) at selected temperatures. The shadowed region in (a) correspond to the PM (paramagnetic) phase ($H < H_c$).

measurements. Mn moments show checkerboard-type AFM order with an antiferromagnetic arrangement for both the in-plane and out-of-plane nearest neighbors, with moments parallel to the c axis. Eu moments show antiferromagnetic order where ferromagnetic layers within the ab plane are stacked antiferromagnetically along the c axis in the sequence of up-up-down-down. Eu moments are aligned parallel to the c axis in the AFM phase, while they are reoriented parallel to the a or b axis with spin-flop domains. Mn magnetic structure is unaffected by the reorientation of the Eu moments within the experimental accuracy. These results offer a concrete basis to reveal the coupling between the Dirac fermion and the magnetic order in $EuMnBi_2$ in future studies.

5.2 Impact of the antiferromagnetic order on the Dirac electronic structure

5.2.1 SdH oscillations in the AFM and SF phases

Figure 5.8 shows $\Delta\rho_{zz}$, the SdH oscillatory components of the interlayer resistivity ρ_{zz} for the magnetic field along the c axis ($H||c$) for the AFM and SF phases at selected temperatures. As seen from Fig. 5.8, the SdH periods are comparable for the AFM and SF phases. In Fig. 5.9 we show the Fourier transform of $\Delta\rho_{zz}$ for two phases. The FFT spectrum shows a peak at $F \sim 20$ T both for the AFM and SF phases as summarized in Tab.5.1, indicating that the Fermi surface cross sections

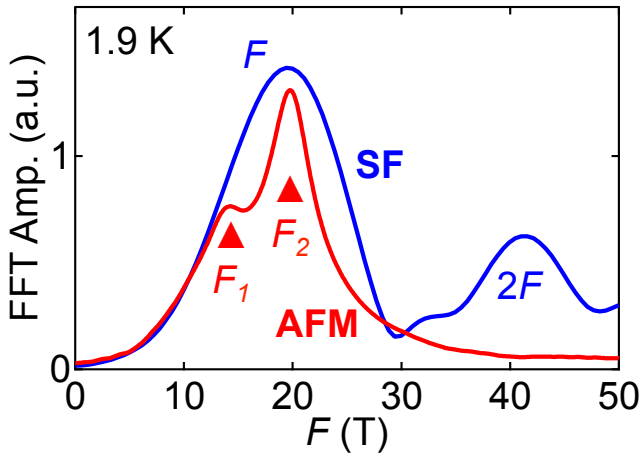

Fig. 5.9 Fourier spectrums of the oscillatory interlayer resistivity $\Delta\rho_{zz}$ for the AFM (red curve) and SF (blue) phases. For the AFM phase, $\Delta\rho_{zz}$ in the range of 1.1 T $< H <$ 5.0 T (0.2 T^{-1} $< 1/H <$ 0.9 T^{-1}) was Fourier transformed. For the SF phase, $\Delta\rho_{zz}$ in the range of 5.4 T $< H <$ 14 T (0.07 T^{-1} $< 1/H <$ 0.19 T^{-1}) was Fourier transformed.

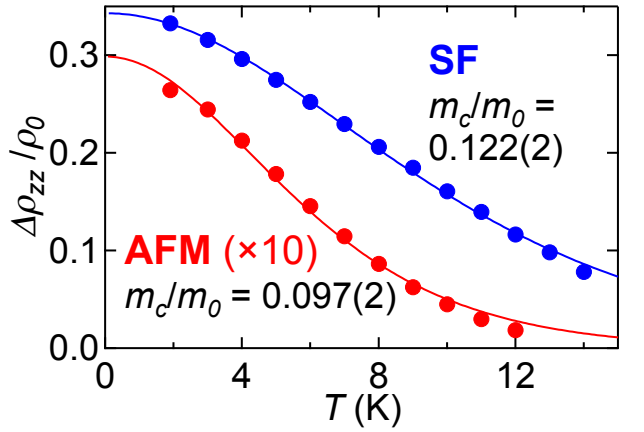

Fig. 5.10 Temperature dependence of the normalized SdH amplitude $\Delta\rho_{zz}/\rho_0$ for the AFM (red curve) and SF (blue) phases. For the AFM phase, $\Delta\rho_{zz}$ was estimated from the Fourier-transform amplitude of the oscillatory signal in the range of 3.6 T $< H <$ 4.0 T (0.25 T^{-1} $< 1/H <$ 0.28 T^{-1}). For the SF phase, $\Delta\rho_{zz}$ and ρ_0 were estimated from the ρ_{zz} values at $H = 6.3$ T ($1/H = 0.16$ T^{-1}, N=3), $H = 7.7$ T ($1/H = 0.13$ T^{-1}, $N = 2.5$) and $H = 9.3$ T ($1/H = 0.11$ T^{-1}, $N = 2$). The solid curves are the fit to the temperature-dependent part of the Lifshitz-Kosevich formula(Eq. 5.3).

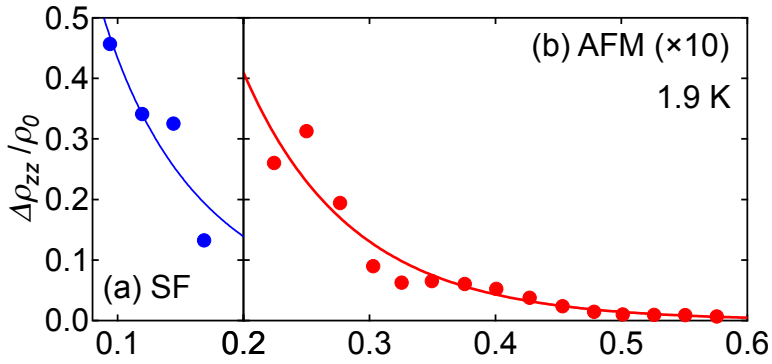

Fig. 5.11 Inverse-field ($1/\mu_0 H$) dependence of the normalized SdH amplitude $\Delta\rho_{zz}/\rho_0$ for the (a) AFM (red curve) and (b) SF (blue) phases, respectively, for 1.9 K. For the SF phase, $\Delta\rho_{zz}$ and ρ_0 were estimated from the ρ_{zz} values at SdH maxima and minima ($1/\mu_0 H$ = 0.18, 0.16, 0.13, 0.11, 0.08 T^{-1}). The solid curves are the fit to the .

	SF	AFM
S_F (nm^{-2})	0.191	0.190
		0.132
m_c/m_0	0.122(2)	0.097(2)
τ (ps)	0.29(16)	0.20(3)

Tab. 5.1 SdH parameters for the SF and AFM phases. $S_F = 2\pi eF/\hbar$ is the extremal cross section of the Fermi surface obtained from the SdH frequency F. m_c/m_0 is the cyclotron mass in unit of the bare electron mass m_0. τ is the scattering time.

are similar for the two phases. This suggest that the Fermi surface volume (i.e. carrier number) is comparable for the two phases, which is consistent with the Hall resistivity ρ_{yx} showing almost no anomaly at the transition from the AFM to the SF phase ($H = H_f$). Also, The FFT spectrum shows two SdH frequencies (F_1 = 13.3 T, F_2 = 19.7 T), indicating that the Fermi surfaces for the AFM phase have two extremal cross sections. Later, we clarify that the origin of the two cross sections are the warping of the quasi-two dimensional Fermi surface.

Figure 5.10 shows the temperature dependence of the normalized SdH amplitude $\Delta\rho_{zz}/\rho_0$ for the AFM and SF phases. The SdH amplitude decreases with increasing temperature. In order to evaluate the cyclotron mass, we analyzed the temperature dependence of the SdH amplitude based on the temperature-dependent part of the

Lifshits-Kosevich (LK) formula

$$\frac{\Delta\rho_{zz}}{\rho_0} \propto \frac{\lambda}{\sinh\lambda}, \lambda = 2\pi^2 k_B T/E_C \tag{5.3}$$

, where k_B is the Boltzmann constant and $E_C = e\hbar\mu_0 H/m_c$ is the cyclotron energy and m_c is the cyclotron mass. The temperature dependence of $\Delta\rho_{zz}/\rho_0$ was fitted by Eq. 5.3, which yields $m_c/m_0 = 0.122(2)$ for the SF phase and $m_c/m_0 = 0.097$ for the AFM phase, respectively, as summarized in Tab. 5.1. The obtained cyclotron masses are sufficiently small, consistent to the Dirac electronic structure in this system. Furthermore, the obtained cyclotron masses are comparable for the AFM and SF phases. Since the magnetic field is applied along the c axis and the cyclotron mass reflects the Fermi velocity within the ab plane, this results suggests that the in-plane dispersion is similar for the AFM and SF phases, which is consistent with the in-plane resistivity ρ_{xx} showing only weak anomaly at the transition from the AFM to the SF phase ($H = H_f$).

Figure 5.11 shows the inverse-field ($1/\mu_0 H$) dependence of the normalized SdH amplitude $\Delta\rho_{zz}/\rho_0$ for the AFM and SF phases. In order to evaluate the mean scattering time τ, we analyzed the $1/\mu_0 H$ dependence of $\Delta\rho_{zz}/\rho_0$ for the AFM phase based on the field-dependent part of the LK formula

$$\frac{\Delta\rho_{zz}}{\rho_0} \propto \frac{1}{\sqrt{H}} \exp\left(-\frac{2\pi^2 k_B T_D}{E_C}\right) \frac{\lambda}{\sinh\lambda} \tag{5.4}$$

, where $T_D = h/k_B\tau$ is the Dingle temperature and τ is the mean scattering time. The $1/\mu_0 H$ dependence of $\Delta\rho_{zz}/\rho_0$ for the AFM phase shown in Fig. 5.11(b) was fitted to Eq. 5.4, yielding the Dingle temperature of $T_D = 6.1(9)$ K and the scattering time of $\tau = 0.20(3)$ ps for the AFM phase. For the SF phase, we analyzed the $1/\mu_0 H$ dependence of $\Delta\rho_{zz}/\rho_0$ for the AFM phase based on the Dingle formula for 2-dimensional electron system:

$$\frac{\Delta\rho_{zz}}{\rho_0} \propto \exp\left(-\frac{2\pi^2 k_B T_D}{E_C}\right) \frac{\lambda}{\sinh\lambda} \tag{5.5}$$

Here, the Dingle formula was used instead of the LK formula for 3D systems, considering the highly two-dimensional electronic structure as clarified by the observation of the bulk multilayer quantum Hall effect. The $1/\mu_0 H$ dependence of $\Delta\rho_{zz}/\rho_0$ for the SF phase shown in Fig. 5.11(a) was fitted to Eq. 5.5, yielding the scattering time of $\tau = 0.29(16)$ ps for the SF phase, which is comparable to that for the AFM phase.

Table 5.1 summarizes the SdH parameters for the AFM and SF phases. The obtained SdH parameters are comparable for the AFM and SF phases, indicating that the Fermi surface size and the in-plane dispersion are similar for the two phases. This result is consistent to ρ_{xx} and ρ_{yx} showing only weak anomalies at the transition from the AFM to the SF phase ($H = H_f$).

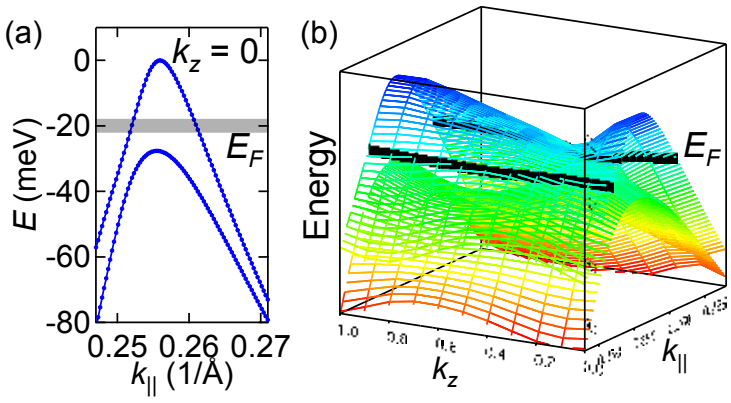

Fig. 5.12 (a) Calculated band structure of $EuMnBi_2$ for the AFM phase in the vicinity of the Dirac point. Only the hole Dirac bands are shown. $k_{||}$ is the wave vector along the [110] ($\Gamma - M$) direction. The Fermi energy E_F is specified by the black line. (b) Calculated band structure for the AFM phase as functions of $k_{||}$ and k_z.

5.2.2 First-principles calculations

As we mentioned before, two SdH frequencies are observed for the AFM phase, indicating that the Fermi surfaces for the AFM phase have two extremal cross sections. In order to clarify the origin of the two extremal Fermi surface cross sections, we performed the first-principles calculation of $EuMnBi_2$ for the AFM phase. Figure 5.12(a) shows the calculated band structure for the AFM phase in the vicinity of the Dirac point. Here, two sets of the Dirac hole bands arises from the unit cell doubling due to the AFM order of the Eu moments. In the PM phase, the crystal structure belongs to the body-centered tetragonal lattice and each unit cell contains one Bi square net layer; in the AFM and SF phases, on the other hand, the Eu magnetic order breaks down the body-centered translational symmetry and the magnetic unit cell contains two Bi square net layers. This lead to the unit cell doubling and the folding of the Dirac band, arising the two sets of the Dirac band. Two Dirac bands are weakly dispersing along the k_z direction as shown in Fig. 5.12(b).

In order to specify the Fermi level, we calculated the Fermi surface cross sections for several Fermi energies and compared them with the experimental SdH frequency. As a result, $E_F \simeq -20$ meV measured from the Dirac hole band top was suggested (see Fig. 5.12). Here, the Fermi energy crosses only the higher Dirac hole band to form a quasi-two-dimensional Fermi surface as shown in Fig. 5.12(b). The warped

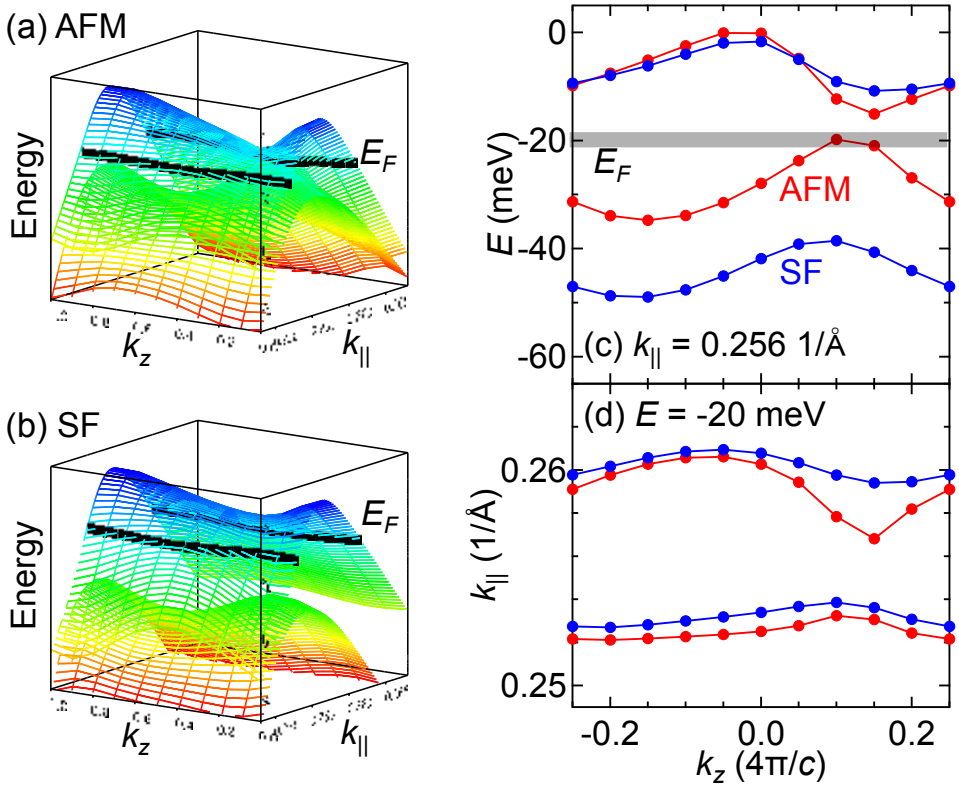

Fig. 5.13 Calculated band structure as functions of $k_{||}$ and k_z for the (a) AFM and (b) SF phases. The Fermi energy E_F is specified by the black curve. (c) k_z dependence of the energy at the top of the higher Dirac hole band ($k_{||} = 0.256$ 1/Å) for the AFM (red markers) and SF (blue) phases. (d) Isoenergy contour at the Fermi level ($E = -20$ meV) on the $k_{||} - k_z$ plane, i.e. the cut of the Fermi surface along the (110) plane.

quasi-two-dimensional Fermi surface has two extremal cross sections along the in-plane direction, which correspond to the two SdH frequencies (F_1, F_2) for the AFM phase (Fig. 5.9). From the two SdH frequencies, the bandwidth W along the k_z direction can be evaluated as:

$$F_2 - F_1 = \frac{\hbar}{2\pi e}(S_{F2} - S_{F1}) = \frac{\hbar}{2\pi e}\frac{\partial S_F}{\partial E}W = \frac{m_c W}{e\hbar} \tag{5.6}$$

Here, S_F is the Fermi surface cross section and $m_c = \frac{\hbar^2}{2\pi}\frac{\partial S_F}{\partial E}\big|_{E_F}$ is the cyclotron mass. Substituting SdH parameters for the AFM phase (Tab. 5.1) into this formula, we obtain $W = 7.2(2)$ meV for the AFM phase. This value is comparable to $W = 11$ meV obtained from the first-principles calculation, supporting our specification of the

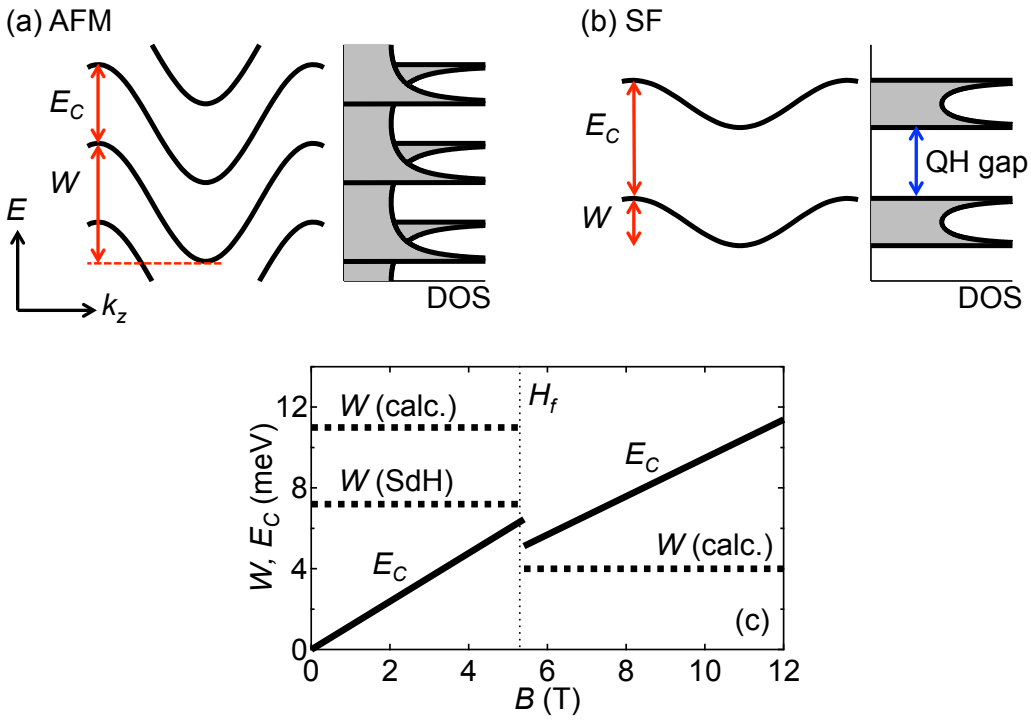

Fig. 5.14 Schematic descriptions of the Landau subbands and the corresponding density of states (D0S) for the (a) AFM and (b) SF phases, respectively. W is the Landau subband width and E_C is the cyclotron energy specifying the intervals between the Landau subbands. Finite quantum Hall (QH) gap exists only for the SF phase. (c) magnetic field dependence of W and E_C. E_C was calculated from the cyclotron masses for the AFM and SF phases summarized in Tab. 5.1. W(SdH) was evaluated using Eq. 5.6 and the SdH frequencies for the AFM phase. W(calc.) was evaluated from the first-principles calculation results shown in FIg. 5.13. $H_f = 5.4$ T denotes the transition field from the AFM to the SF phase.

Fermi level.

We also performed the first-principles calculation for the SF phase. In Fig. 5.13 we compare the calculated band structures for the AFM and SF phases. The higher Dirac hole band is more weakly k_z-dispersing for the SF phase as seen from Figs. 5.13(a-b) and the $E - k_z$ curve at the Dirac hole band top shown in Fig. 5.13. The bandwidth W along the k_z direction at the Dirac hole band top is about one-third smaller in the SF phase ($\frac{W_{\rm SF}}{W_{\rm AFM}} \simeq \frac{1}{3}$). This result is consistent to the enhancement in ρ_{zz} for the SF phase by about 5 to 10 times, considering that ρ_{zz} is proportional to the inverse square of W ($\rho_{zz} \propto W^{-2}$). Due to the suppression of the k_z-dispersion, i.e. W, in the SF phase, the Fermi surface is more cylindrical in the SF phase than in the AFM phase, which is consistent to the single SdH frequency for the SF phase (Fig.5.9).

5.2.3 Mechanism of the bulk multilayer quantum Hall effect in the SF phase

Now, we discuss the mechanism of the bulk multilayer quantum Hall effect in the SF phase in terms of the Landau subband structures. When the magnetic field is applied along the c axis, the electron motion within the ab plane is Landau-quantized, while the motion along the c axis is retained. Therefore the band structures shown in Fig. 5.13(a,b) are quantized to form one dimensional Landau subbands dispersing along the k_z direction with the bandwidth W. The Landau subbands line up at intervals of the cyclotron energy E_C as shown in Fig. 5.14(a). In Fig. 5.14(c) we plot the magnetic field dependence of the Landau subband width W and the cyclotron energy E_C. Here, E_C and W was calculated from the SdH parameters in Tab. 5.1 and W was estimated from the first-principles calculation results. For the AFM phase ($H < H_f$) the Landau subband width W is larger than the Landau subband spacing E_C ($W > E_C$). The corresponding Landau subband structure and the density of states (DOS) is depicted in Fig. 5.14(a). There, since $W > E_C$, the DOSs form each Landau subbands overlap with each other and the total DOS remain finite for any energy or magnetic field. In this case, standard SdH oscillations of quasi-two-dimensional or three-dimensional metals are observed: the SdH amplitude is relatively small and ρ_{xx} remain finite for any magnetic field, in consistent with the experimental results. Furthermore, the Hall resistivity ρ_{yx} is not quantized, although the show finite SdH oscillations. For the SF phase ($H > H_f$), on the other hand, E_C is larger than W due to the decrease in W as seen from Fig. 5.14(c). The corresponding Landau subband structure and the density of states (DOS) is depicted in Fig. 5.14(b). There, since $W < E_C$, the Landau subbands are separated by the quantum Hall gap where the DOS is zero. In this case, the DOS converge to zero when the Fermi energy is located in the quantum Hall gap, resulting in the in-plane resistivity ρ_{xx} converging to zero, ρ_{yx} quantized into plateaus and ρ_{zz} showing giant SdH oscillations. Thus, the bulk multilayer quantum Hall effect is induced in the SF phase because the Landau subband width W along the k_z direction is suppressed and become smaller than E_C, inducing the finite quantum Hall gap.

5.2.4 Mechanism of the enhanced two-dimensionality in the SF phase

Finally, we discuss the mechanism of the enhanced two-dimensionality (i.e. suppressed W) in the SF phase. Fig. 5.15 shows the schematic magnetic and electronic structures for the PM, AFM and SF phases. For the PM phase, the crystal structure belongs to the body-centered tetragonal lattice with one Bi square net layer per unit cell. The corresponding band structure shown in Fig. 5.15(d) disperses almost linearly along the in-plane direction $k_{||}$ and weakly disperses along the k_z direction. The bandwidth along the k_z direction is $4t$, where t is the transfer energy between the adjacent Bi layers (Fig. 5.15[a]). In the AFM and SF phases, Eu antiferromagnetic order breaks

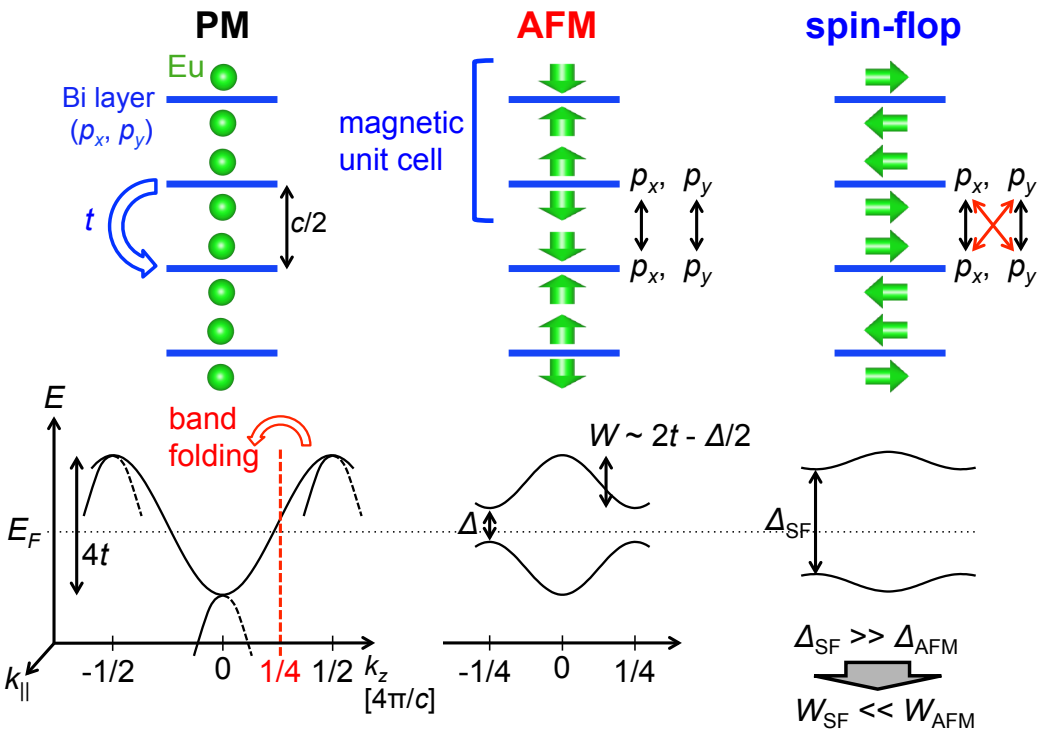

Fig. 5.15 (a-c) Schematic crystal and magnetic structure for the PM, AFM and SF phases, respectively. The blue lines represent the Bi square net layer hosting Dirac fermion and the green balls and allows represent the Eu atoms/moments. t is the interlayer transfer energy between the Bi square net layers. (d-e) Schematic electronic structure for the PM, AFM and SF phases, respectively.

the body-centering translational symmetry, and the magnetic unit cell contains two Bi layers as shown in Fig. 5.15(b, c). As a result, the band structure in the PM phase is folded in the k_z direction to form two sets of the Dirac hole band as shown in Fig. 5.15(e, f). The Fermi energy cross only the higher Dirac hole band to form a quasi-two-dimensional Fermi surface. Here, we desire to clarify the mechanism of the suppressed W in the SF phase. From the first-principles calculation results in Fig. 5.13, it is seen that W is decreased and the gap Δ between the two Dirac hole bands is increased in the SF phase. This result indicates that the increase in Δ is the origin of the suppressed W in the SF phase. We propose that the origin of the enhanced Δ in the SF phase is the additional hybridization via the Eu moment between the Bi p orbitals on the adjacent Bi layers. The Dirac fermion on the Bi layer arises from the Bi p_x and p_y orbitals. Therefore we speculate that the Bi p_x orbital on a Bi layer can hybridize with the Bi p_y orbital on the adjacent layer via the Eu moments directed along the a or b direction in the SF phase, leading to the enhancement in Δ.

5.2.5 Summary for Chap. 5.2

Here, we investigated the Dirac electronic structure and the Landau subband structure for the AFM and SF phases by means of the quantitative analysis of the SdH oscillations and the first-principles calculation. SdH oscillations and first-principles calculations together revealed the similar in-plane dispersion and Fermi surface volume in the AFM and SF phases. In the AFM phase, the antiferromagnetic order of the Eu moments doubles the unit cell and fold the Dirac band in the k_z directions to form two sets of the Dirac bands weakly dispersing along the k_z direction, and only the higher Dirac hole band crosses the Fermi level to form a quasi-two-dimensional Femi surface. In the SF phase, the higher Dirac hole band becomes more weakly dispersing along the k_z direction to induce the enhanced interlayer resistivity ρ_{zz}. Furthermore, this induces the quantum Hall gap between the Landau subbands, leading to the bulk multilayer quantum Hall state in the SF phase. The origin of the weak k_z dispersion was sought in the enhancement in the gap between two sets of the Dirac bands, which may due to the additional hybridization between the Bi p_x and p_y orbitals on the adjacent Bi layers forming the Dirac band via the Eu moments directed along the in-plane direction.

Chapter 6

Landau level splitting modulated by the AFM order in $EuMnBi_2$

$AMnX_2$ (A: alkaline-earth and rare-earth ions, X: Bi and Sb)[41, 39, 121, 122, 123, 124, 44, 43, 126, 125, 127, 128, 129] is also promising as a fertile ground for magnetic Dirac materials, since the crystal structure consists of an alternate stack of a two-dimensional (2D) Dirac fermion conduction layer (X^- square net)[66, 130] and a magnetic insulating layer (A^{2+}-Mn^{2+}-X^{3-}) [see Fig. 6.1(a)]. Among them, $EuMnBi_2$ is a rare compound that exhibits quantum transport of Dirac fermions coupled with the field-tunable magnetic order. In this compound, the interlayer coupling between each Dirac fermion (Bi) layer is dramatically suppressed by the flop of the antiferromagnetically-ordered Eu moments [Fig. 6.1(a)]. The enhanced two dimensionality leads to the giant magnetoresistance effects[44, 43] and the quantum oscillation phenomena[43] that strongly depend on the magnetic order of the Eu sublattice. However, in spite of such a marked impact of magnetism on the transport properties, it remains elusive how and to what extent the Dirac-like band dispersion is affected.

To reveal the coupling between the band structure and magnetic order, the Landau level quantization in a magnetic field can be a powerful probe, since it exhibits the energy splitting due to Zeeman and exchange coupling as well as electron-electron interaction. As demonstrated in the conventional 2D electron gas in semiconductor heterostructures[67] and semimagnetic quantum wells[131], the detailed analyses on the splitting provide lots of information on the band parameters and magnetism of the system, which have been recently performed for graphene[132, 133] and several Dirac semimetals[134, 135, 136]. Also for $EuMnBi_2$, clear Landau level splitting was observed in the SdH oscillation in resistivity[43], the origin of which has not been clarified so far. In this Letter, we clarify that the Landau level splitting in $EuMnBi_2$ is primarily of spin origin, on the basis of the systematic measurements of the SdH oscillations in tilted magnetic fields. The field-angle dependence of SdH oscillations have revealed the effective g factors for the Dirac fermions, which strongly depends on

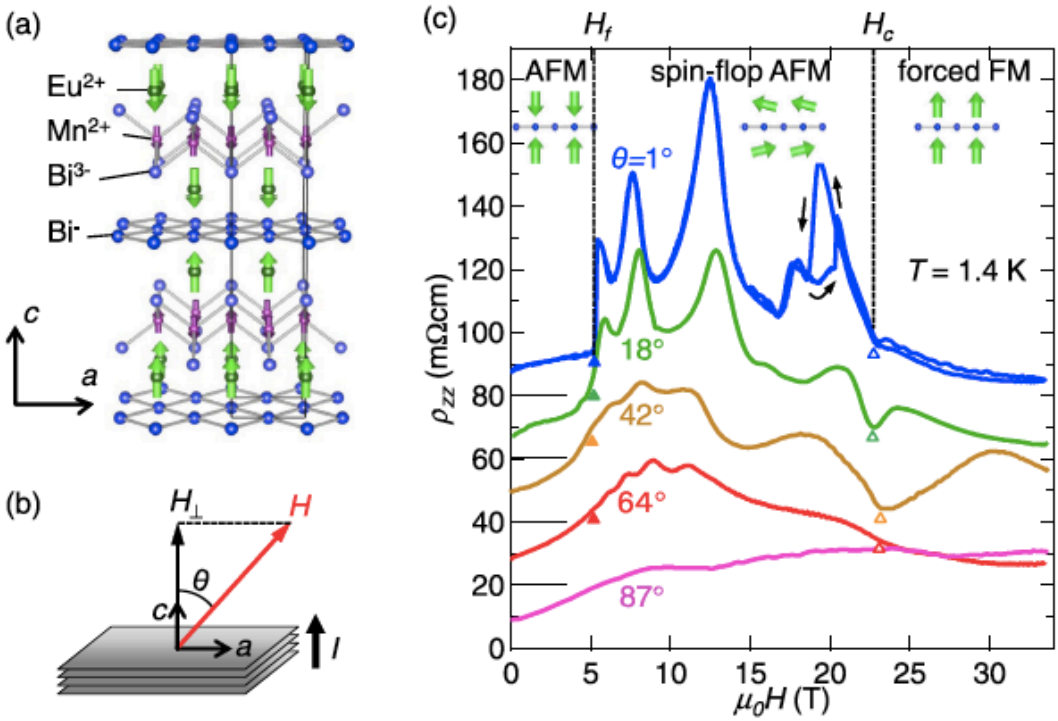

Fig. 6.1 (Color online) (a) Schematic illustration of the crystal and magnetic structure at 0 T for $EuMnBi_2$ [43, 45]. (b) Geometry of the interlayer transport measurement in a tilted magnetic field in the a-c plane, where θ is an angle between the field and the c axis. (c) Field profile of ρ_{zz} at 1.4 K for selected values of θ. For clarity, the curves are shifted vertically by 20 mΩcm. For $\theta < 64°$, the closed triangle denotes H_f while the open triangle denotes H_c. The positions of H_f and H_c are determined as the fields where ρ_{zz} shows a jump and drop in the field-increasing run, respectively. For details, see supplementary Fig. S**. The magnetic order of the Eu sublattice for each antiferromagnetic phase is shown schematically in the inset.

the antiferromagnetic (AFM) order of the Eu sublattice. As a plausible explanation, we discuss the exchange coupling between Dirac fermions and local Eu moments by considering the results of the first-principles calculations.

6.1 Observation of the spin-split Landau levels

For investigating the fine structures of Landau levels, we have here adopted the measurements of interlayer resistivity ρ_{zz}. This is because the high-resistive ρ_{zz} has a much better S/N ratio than that achieved in the in-plane resistivity ρ_{xx}. A rotation of magnetic field is also important in the present study. In 2D systems, the ratio of the cyclotron energy E_c to the Zeeman energy E_Z can be tuned by changing the tilt angle

of the field from the normal to the 2D plane (θ); E_c is proportional to $H_\perp = H\cos\theta$ [the field component perpendicular to the 2D plane, see Fig. 6.1(b)], while E_Z is proportional to H (the total field). The combination of these techniques allow us to elucidate the mechanism of the Landau level splitting and hence the microscopic nature of the Dirac fermions in $EuMnBi_2$, as described below.

Figure 6.1(c) shows the field dependence of interlayer resistivity ρ_{zz} for $EuMnBi_2$ up to 35 T at selected tilt angles of the field. We first review the transport features for the field parallel to the c axis (at $\theta = 1^\circ$). With increasing the field, ρ_{zz} exhibits a steep jump at the spin-flop transition of the Eu sublattice ($H_f \sim 5.3$ T), followed by large SdH oscillations. In the forced ferromagnetic (FM) phase above $H_c \sim 22$ T, however, the value of ρ_{zz} significantly decreases, indicating that ρ_{zz} is specifically enhanced in the spin-flop AFM phase. There, the Dirac fermions in the Bi layer are strongly confined in two dimension, resulting in the signature of multilayer half-integer quantum Hall effect in the in-plane conductions[43].

Similar enhancement in ρ_{zz} in the spin-flop AFM phase was observed at θ up to $\sim 65^\circ$, which is gradually reduced with increasing θ. Concomitantly, the spin-flop transition at H_f is less sharp at high θ, which is still discernible up to $\theta = 64^\circ$ as denoted by closed triangles in Fig. 6.1(c) (for the determination of H_f, see Fig. 6.2). The manner of the SdH oscillation is also strongly dependent on θ, whereas the values of H_f and H_c are almost independent of θ. Note here that, in addition to the SdH oscillation, a hysteretic resistivity anomaly is discernible around 20 T at θ=1°, which immediately disappears when θ increases up to 18°. At present, the origin of this highly-θ-sensitive anomaly remains unclear, the study of which is beyond the scope of this paper. In the following, we shall focus on the θ dependence of the SdH oscillations in ρ_{zz}.

We first show in Fig. 6.3(a) the features of the Landau levels in the spin-flop AFM phase ($H_f < H < H_c$) by presenting the θ dependence of interlayer conductivity $\sigma_{zz} = 1/\rho_{zz}$.The horizontal axis of Fig. 6.3(a) denotes $H_F^0/H_\perp$, the normalized filling factor for a 2D system[57, 43], where H_F^0(=19.3 T) is the SdH frequency for the field parallel to the c axis (Fig. 6.4). At θ=1°, σ_{zz} shows the minima at $H_F^0/H_\perp \simeq 1.5, 2.5, 3.5$, which coincides with the oscillations in σ_{xx} and ρ_{xx}[43]. Since the deep minima in σ_{zz} and σ_{xx} indicate the quantum Hall states[137, 53, 138], the corresponding $H_F^0/H_\perp$ should be given by $H_F^0/H_\perp = N + 1/2 - \gamma$, where N is the Landau index and γ is the phase factor expressed as $\gamma = 1/2 - \phi_B/2\pi$ with ϕ_B the Berry's phase[56]. The σ_{zz} minima occurring at half-integer multiples of $H_F^0/H_\perp$ thus lead to $\gamma \sim 0$, i.e., the nontrivial π Berry's phase in $EuMnBi_2$. In multilayer quantum Hall systems, it was reported that a chiral surface state contributes partly to the interlayer transport in the quantum Hall states (i.e., σ_{zz} minima)[137, 53, 138], which does not affect the frequency or phase of the SdH oscillation discussed below. When θ increases, the frequency of the SdH oscillation increases in proportion to $1/\cos\theta$ [Fig. 6.4(c)], indicating highly 2D nature of the Fermi surface. This results in the almost θ-independent oscillation period when plotted as a function of $H_F^0/H_\perp$, as

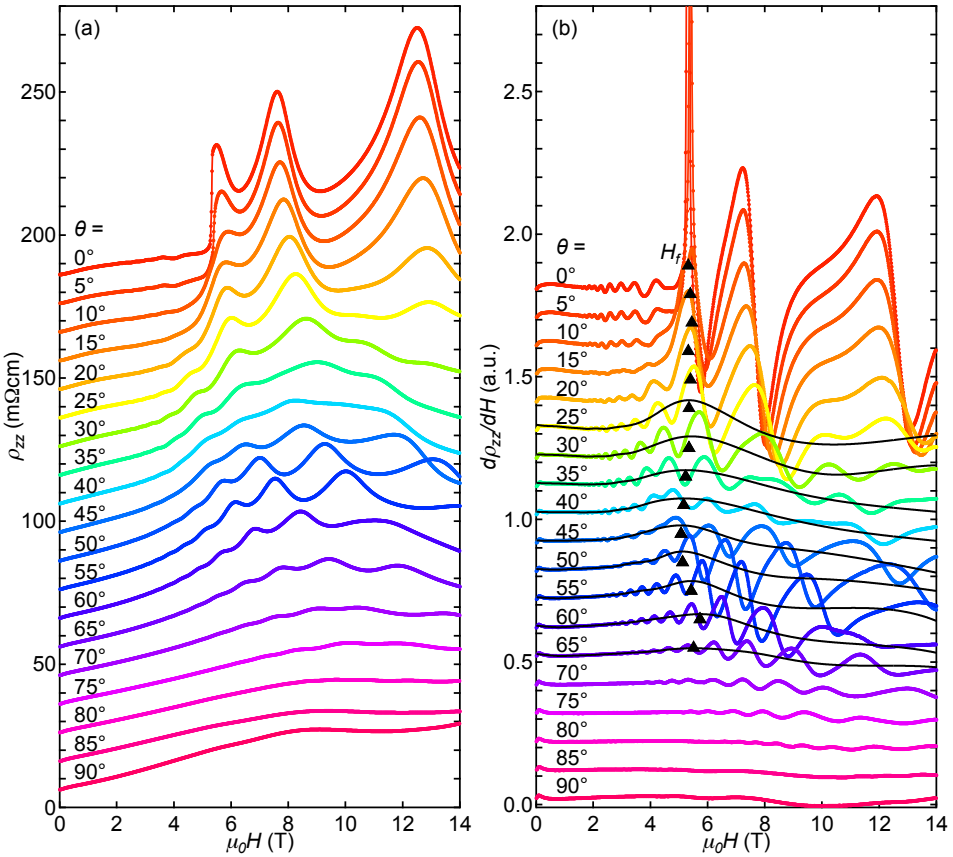

Fig. 6.2 Magnetic field dependence of (a) the interlayer resistivity ρ_{zz} and (b) the field derivative $d\rho_{zz}/dH$ for various tilt angles. The curves are shifted vertically for clarity. The triangles indicate H_f, the transition field to the spin-flop AFM phase. Solid curves are the non-oscillatory part of $d\rho_{zz}/dH$ for $25^\circ \leq \theta \leq 65^\circ$. For $\theta \leq 20^\circ$ a steep jump in ρ_{zz} (i.e. sharp peak in $d\rho_{zz}/dH$) was clearly observed at $H_f \sim 5.3$ T, corresponding to the spin-flop transition. Although the ρ_{zz} jump becomes less sharp as θ is increased, it is barely discernible up to $\theta = 65^\circ$ as seen in Fig. 6.2 (a). For $25^\circ \leq \theta \leq 65^\circ$, H_f was determined from the maxima of the non-oscillatory component of the $d\rho_{zz}/dH$ [denoted by solid curves in (b)].

highlighted by the vertical dotted lines up to $\theta \sim 50^\circ$ in Fig. 6.3(a). For $\theta \geq 55^\circ$, however, the frequency gradually deviates from the $1/\cos\theta$ scaling presumably due to a weak warping of the Fermi surface caused by the non-zero interlayer coupling.

The most salient feature of the SdH oscillation is that the amplitude significantly varies with θ. With increasing θ up to 35°-40°, the amplitude progressively decreases to nearly zero. Above $\theta = 40^\circ$, the amplitude again increases but with an inverted phase. The observed θ dependence of the SdH amplitude is well explained by considering the spin splitting of the Landau levels due to E_Z as follows[95, 96, 97]. When

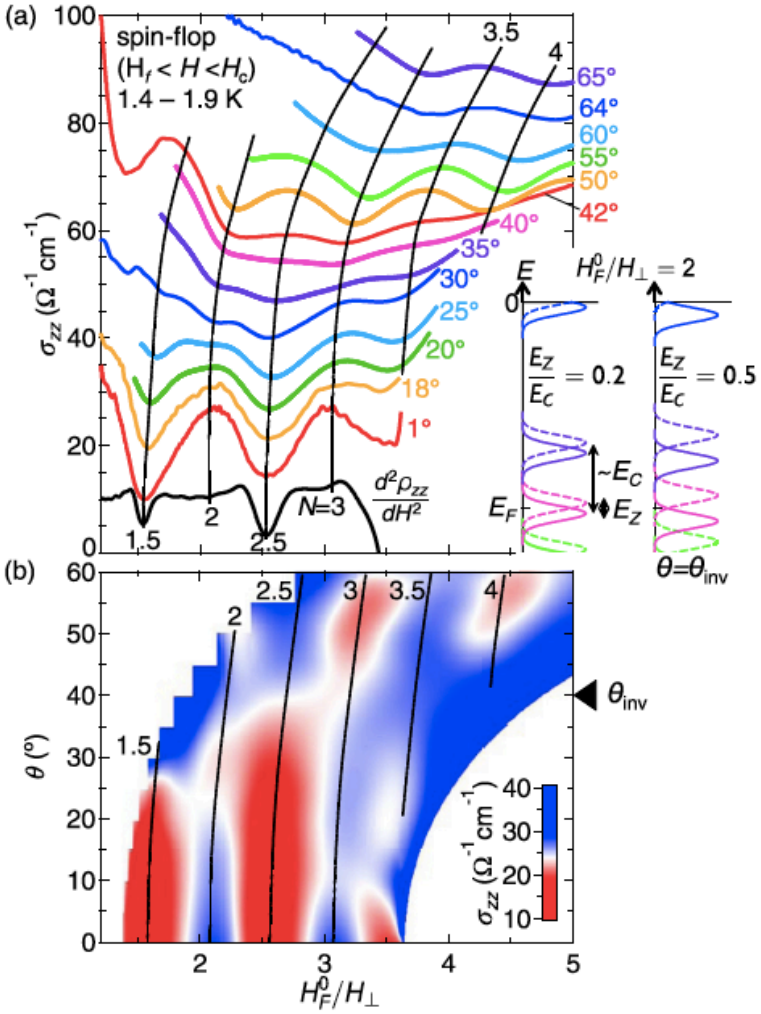

Fig. 6.3 (Color online) (a) σ_{zz} versus $H_F^0/H_\perp$ at θ=1°-65° in the spin-flop AFM phase ($H_f < H < H_c$), where H_F^0 denotes the SdH frequency for the field parallel to the c axis. The curves at $\theta \geq 18°$ are shifted upward for clarity. At the bottom of the panel, the second field derivative $d^2\rho_{zz}/dH^2$ at $\theta = 1°$ is shown. Vertical dotted lines are guides to the eye showing the positions of the maxima and minima of the SdH oscillation, where N denotes the Landau index. Inset: Schematic of the density of states for spin-split Landau levels for a 2D massless Dirac fermion as a function of energy E for $H_F^0/H_\perp = 2$, where E_F is set negative corresponding to the hole carrier system. The value of $E_\mathrm{Z}/E_\mathrm{c}$ can be tuned by tilting the field, where $E_\mathrm{Z} = g^*\mu_\mathrm{B}B$ is the Zeeman energy, $E_\mathrm{c} \equiv e\hbar B_\perp/m_\mathrm{c}$ the effective cyclotron energy, and m_c the cyclotron mass $m_\mathrm{c} = E_\mathrm{F}/v_\mathrm{F}^2$. $E_\mathrm{Z}/E_\mathrm{c} = 0.2$ (left) and 0.5 (right). For details of the calculation, see the main text and supplementary Fig. S3. (b) Color plot of σ_{zz} as functions of $H_F^0/H_\perp$ and θ. θ_inv indicated by the triangle corresponds to θ where the phase of the SdH oscillation is inverted and $E_\mathrm{Z}/E_\mathrm{c}$ is nearly 0.5.

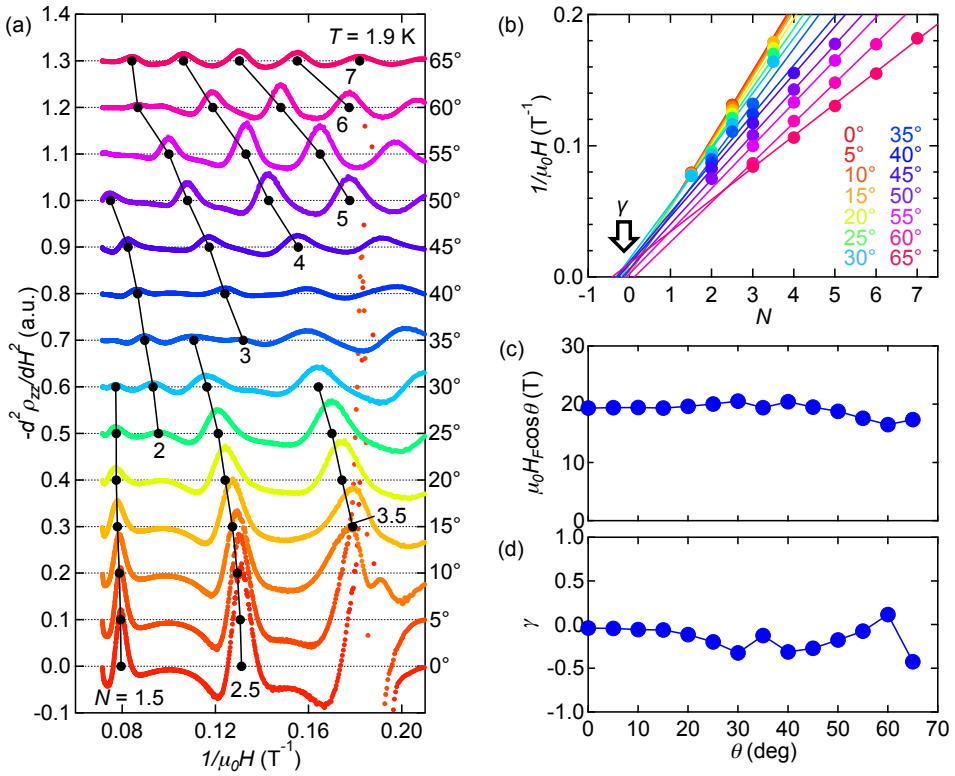

Fig. 6.4 (a) Second field derivative $-\frac{d^2\rho_{zz}}{dH^2}$ for various tilt angles. Markers shows the fields of (half-)integer SdH indices. (b) Fan diagram. For $\theta = 0°$, we plot the values of $1/\mu_0 H$ at the ρ_{zz} (or $-d^2\rho_{zz}/dH^2$) maxima against half-integer Landau indices[43]. The SdH frequency $\mu_0 H_F^0 = 19.3$ T and the phase factor $\gamma \sim -0.04$ for $\theta = 0°$ are consistent with the previous report[43]. We adopted the similar procedure for all θ. However, for $\theta \gtrsim 35°$ we assumed that the peaks in $-d^2\rho_{zz}/dH^2$, which arise from the gaps between spin-split Landau levels, should correspond to the *integer* Landau indices. See also Fig. 6.11. (c) SdH frequency $H_F \cos\theta$ and (d) phase factor γ as a function of θ. The SdH frequency H_F shows the typical 2-dimensional θ dependence $H_F(\theta) \simeq H_F^0/\cos\theta$ with a small discrepancy of up to $\sim 15\%$.

E_Z/E_c is smaller than unity [e.g., $E_Z/E_c = 0.2$ in the inset (left) to Fig. 6.3(a)], the Landau level exhibits a weak spin splitting, which is barely discernible at $\theta \sim 1°$ when plotted in the form of $d^2\rho_{zz}/dH^2$ [Fig. 6.3(a)][43] . With increasing E_Z/E_c by tilting the field, the magnitude of the spin splitting increases, resulting in the reduction in amplitude of the SdH oscillation. Around $\theta = 40°$, the amplitude reaches the minimum, which corresponds to $E_Z/E_c = 0.5$ [the inset (right) to Fig. 6.3(a)]. A further increase in E_Z/E_c leads to crossing of the neighboring Landau levels with opposite spins, which results in the enhanced SdH oscillation with an inverted phase, as observed at $\theta > 50°$. Note here, since the energy spacing of Landau levels for a 2D

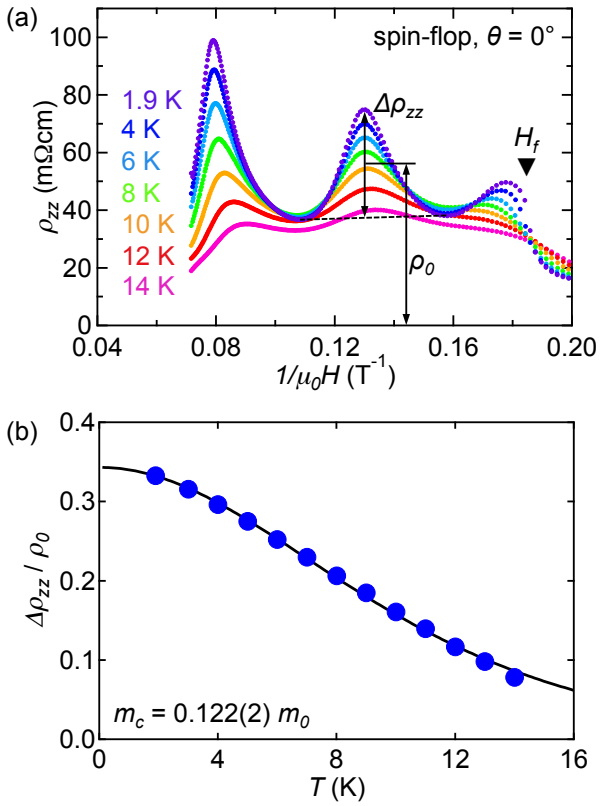

Fig. 6.5 (a) ρ_{zz} as a function of $1/\mu_0 H$ in spin-flop AFM phase at selected temperatures at $\theta = 0°$. $\Delta\rho_{zz}$ and ρ_0 denote the SdH amplitude and the background resistivity at 1.9 K respectively. The amplitude of the SdH oscillations are gradually suppressed as the temperature increases. $\Delta\rho_{zz}$ and ρ_0 are estimated from the ρ_{zz} values at $N = 3$ ($1/\mu_0 H = 0.16$ T^{-1}), $N = 2.5$ ($1/\mu_0 H = 0.13$ T^{-1}) and $N = 2$ ($1/\mu_0 H = 0.11$ T^{-1}) as depicted in Fig. 6.5(a). Note here that for the present analysis we adopted the SdH oscillation at the lowest fields within the spin-flop AFM phase in order to avoid the prominent spin splitting at high fields influencing the estimate of m_c. (b) Temperature dependence of $\Delta\rho_{zz}/\rho_0$. The solid curve is the fit to the data by the Lifshits-Kosevich (LK) formula, which yields $m_c = 0.122 m_0$ for the spin-flop AFM phase.

Dirac fermion is not uniform (i.e., E_c is dependent on N), we need to effectively define $E_c \equiv e\hbar B_\perp / m_c$ by using a semiclassical expression of the cyclotron mass $m_c = E_F / v_F^2$ with v_F and E_F being the Fermi velocity and Fermi energy, respectively[20, 21]. In this scheme, the Landau level crossing in the SdH oscillation occurs when $E_Z/E_c = 1$ irrespective of N, as in the case for a normal 2D electron gas [for details, see Fig. 6.11 and related discussions].

To highlight the θ dependence of the SdH oscillations, we present a contour plot of σ_{zz} as functions of $H_F^0/H_\perp$ and θ in Fig. 6.3(b). It is clear that the phase of

the SdH oscillation is inverted around $\theta_{\rm inv} \sim 40^\circ$, accompanied by the minimum amplitude. As shown in Fig. 6.11(c), this plot is nicely reproduced by calculating the density of states of spin-split Landau levels, where $E_{\rm Z}/E_{\rm c} = 0.5$ corresponds to $\theta = \theta_{\rm inv}$.Noting that $E_{\rm Z}/E_{\rm c} = g^* m_{\rm c}/2m_0 \cos\theta$, this relation gives $\cos\theta_{\rm inv} = g^* m_{\rm c}/m_0$, where g^* is the effective g factor and m_0 is the bare electron mass. By substituting the experimental value ($\theta_{\rm inv} = 40^\circ \pm 5^\circ$), we obtain $g^* m_{\rm c}/m_0 = 0.77(6)$. The value of $m_{\rm c}/m_0$ is independently estimated to be 0.122(2) from the temperature dependence of the SdH oscillations at $\theta = 0^\circ$ based on the standard Lifshitz-Kosevich formula (Fig. 6.5), which results in $g^* = 6.6(6)$. The obtained g^* is much larger than 2, reflecting strong spin-orbit coupling inherent to Bi atom. Additionally, it is presumable that the exchange interaction with the local Eu moments plays a significant role, since net magnetization is non-zero in the spin-flop AFM phase, as discussed later.

6.2 Magnetic structure dependence of the Landau level splitting

Next, we shall show the Landau level splitting in the AFM phase ($H < H_f$), where the amplitude of SdH oscillation is largely reduced as compared with the spin-flop AFM phase. Nonetheless, the oscillation is discernible above ∼1.3 T, as shown in Fig. 6.6(b) where $d^2\rho_{zz}/dH^2$ is plotted for clarity. The weakly beating amplitude presumably signifies the superposition of maximum and minimum cyclotron orbits arising from a slightly warped cylindrical Fermi surface. To summarize the θ dependence of SdH oscillation, we show in Fig. 6.6(a) the color contour plots of $d^2\rho_{zz}/dH^2$ and σ_{zz} for the AFM and spin-flop AFM phases, respectively, as functions of $H_F^0/H_\perp$ and θ. The SdH oscillation in the AFM phase has several common features with that in the spin-flop AFM phase; the period of the SdH oscillation is nearly independent of θ when plotted versus $1/H_\perp$, reflecting a quasi-2D Fermi surface. In addition, the spin splitting of the Landau levels makes the oscillation amplitude dependent on θ, leading to the phase inversion at $\theta_{\rm inv}$ (a horizontal line). However, the value of $\theta_{\rm inv}$ is substantially different in the two phases; $\theta_{\rm inv} \sim 18^\circ$ for the AFM phase while $\theta_{\rm inv} \sim 40^\circ$ for the spin-flop AFM phase. This results in $g^* m_c/m_0 = \cos\theta_{\rm inv} = 0.95(1)$ for the AFM phase ($\theta_{\rm inv} = 18^\circ \pm 2^\circ$), which is approximately 25% larger than that for the spin-flop AFM phase.

In Table 6.1, we compare the band parameters estimated from the SdH oscillation for each AFM phase. The cross section of quasi-2D Fermi surface $S_{\rm F}$ deduced from the SdH frequency (H_F^0) is almost the same for both AFM phases, whereas the values of $m_{\rm c}$ and g^* significantly depend on the AFM order. Since the AFM phase hosts larger $g^* m_{\rm c}/m_0$ and smaller $m_{\rm c}/m_0$ than the spin-flop AFM phase, the resultant g^* value for the former phase is approximately 50% larger than that for the latter phase. These facts indicate that the Dirac-like band for $EuMnBi_2$ is largely modulated by the AFM order of Eu sublattice.

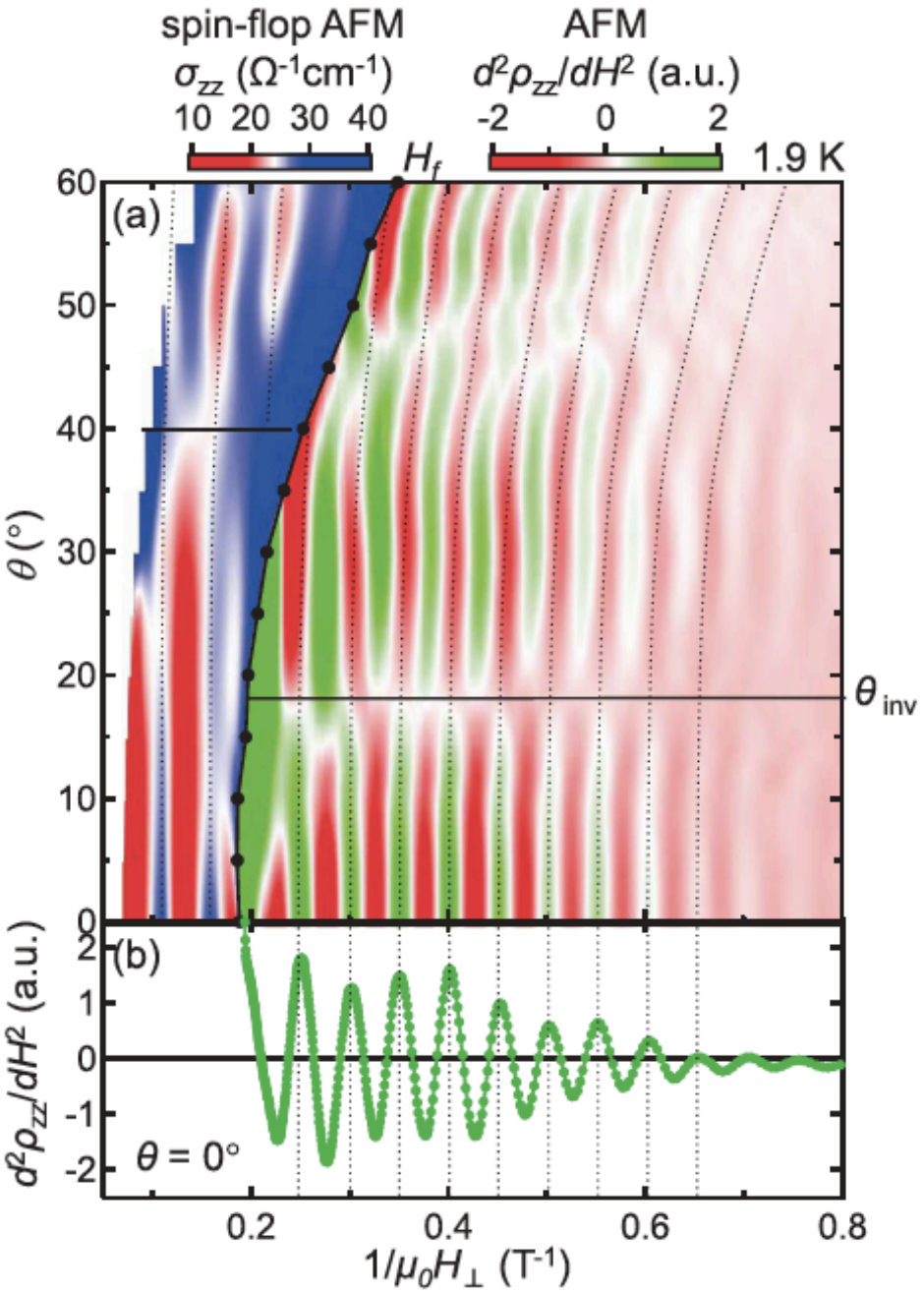

Fig. 6.6 (Color online) (a) Color plot of $d^2\rho_{zz}/dH^2$ as functions of $H_F^0/H_\perp$ and θ in the AFM phase (for $H < H_f$). To compare the θ dependence, the σ_{zz} data in the spin-flop AFM phase (for $H > H_f$) are plotted together. The position of H_f at each θ is denoted by a closed circle, which is determined as the field where ρ_{zz} shows a steep increase (see Fig. 6.2). The horizontal line denotes θ_inv for each phase. (b) Profile of $d^2\rho_{zz}/dH^2$ versus $H_F^0/H_\perp$ for $\theta = 0^\circ$ ($H < H_f$).

Tab. 6.1 Experimentally determined band parameters for the AFM and spin-flop AFM phases. For the estimation of S_F and m_c, see supplementary Figs. 6.5, 6.7, 6.8

	S_F (nm^{-2})	$g^* m_c/m_0$	m_c/m_0	g^*
AFM	0.186	0.95(1)	0.097(2)	9.8(4)
spin-flop	0.191	0.77(1)	0.122(2)	6.6(4)

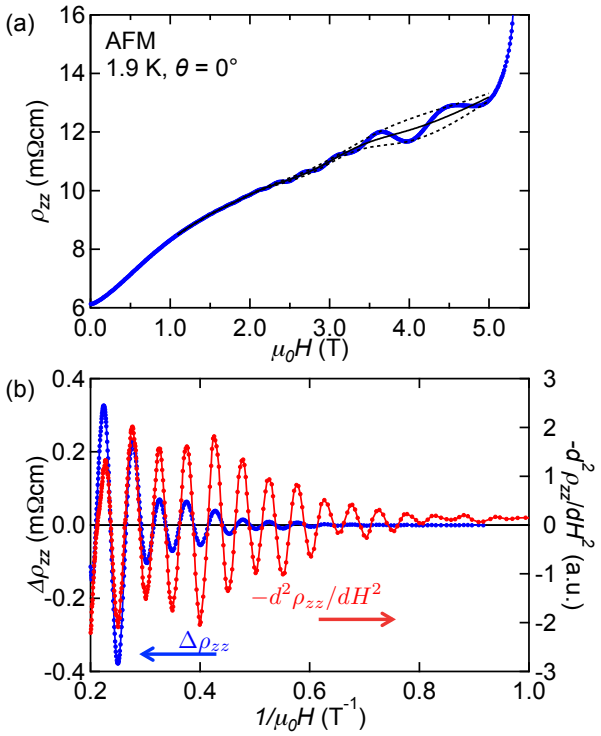

Fig. 6.7 (a) ρ_{zz} versus H at 1.9 K at $\theta = 0°$ for the AFM phase ($H < H_f$). In order to extract the oscillatory part $\Delta\rho_{zz}$ and the non-oscillatory part ρ_0 for the AFM phase, we used the envelope method[99]. The dashed curves are the envelopes of the SdH oscillations, while the solid curve is the non-oscillating part ρ_0, which is the midpoint of the two envelope curves. (b) The oscillatory component of the interlayer resistivity $\Delta\rho_{zz}$ and the second field derivative $-d^2\rho_{zz}/dH^2$ as a function of $1/\mu_0 H$. The oscillatory signals in $\Delta\rho_{zz}$ and $-d^2\rho_{zz}/dH^2$ have the same phase, indicating that we correctly extracted the oscillatory signal $\Delta\rho_{zz}$.

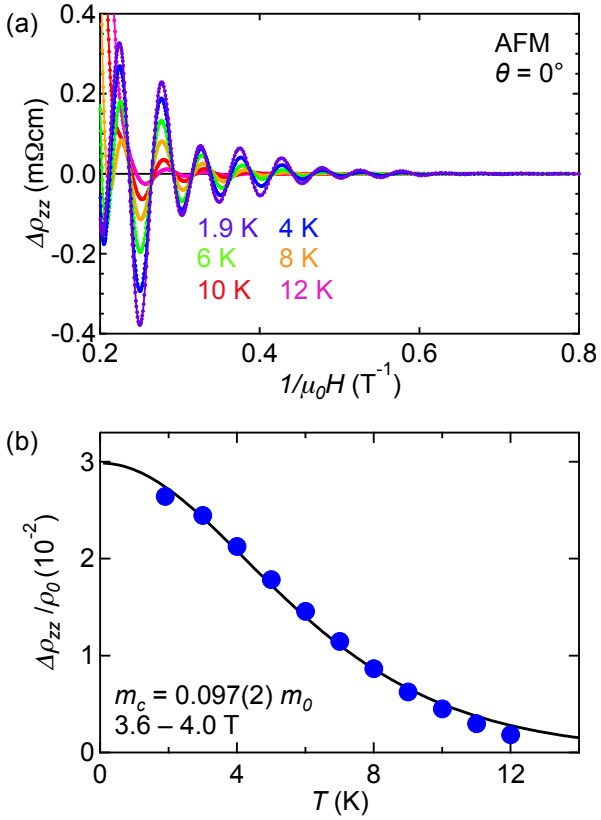

Fig. 6.8 (a) $\Delta\rho_{zz}$ versus $1/\mu_0 H$ curve for the AFM phase at selected temperatures at $\theta = 0°$. The amplitude of the SdH oscillations decreases with increasing temperature. (b) Temperature dependence of $\Delta\rho_{zz}/\rho_0$. Here, Fourier-transform amplitude of $\Delta\rho_{zz}$ for 3.6 T $< \mu_0 H <$ 4 T is used as the SdH amplitude. The solid curve is the fit to the data by the Lifshitz-Kosevich formula, which yields $m_c = 0.097 m_0$ for the AFM phase.

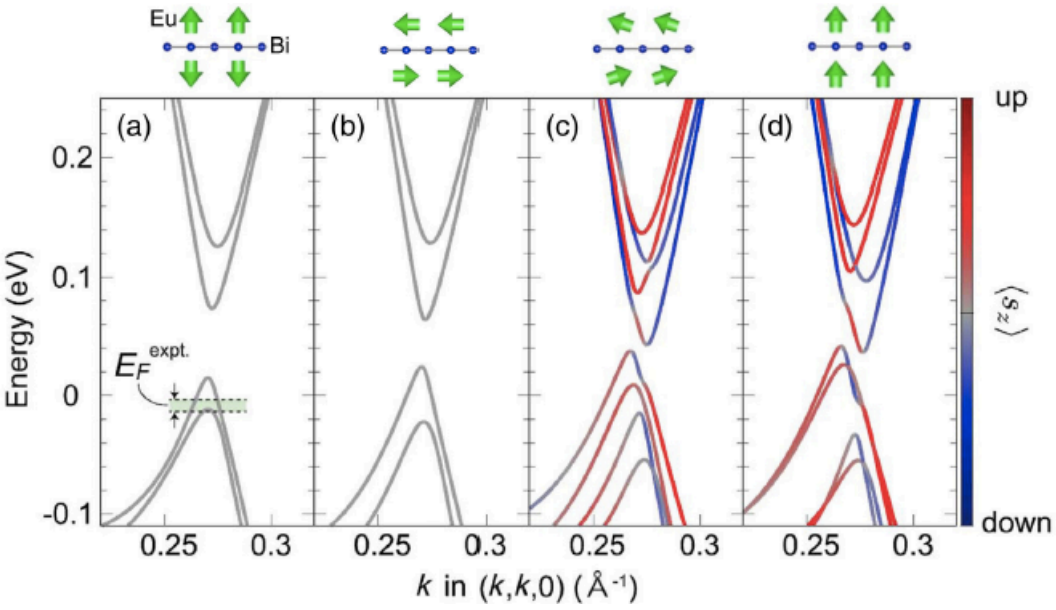

Fig. 6.9 Calculated Dirac-like band structures along the Γ-M line for various magnetic states in $EuMnBi_2$. (a) AFM, (b, c) spin-flop AFM, and (d) forced FM states. In (b), the Eu moment is along the a axis, while in (c) it is inclined at an angle of ∼47° to the c axis on the ac plane. The spin polarization $\langle s_z \rangle$ of each band is represented by red (up) and blue (down) colors. Schematic illustration of the Eu moments adjacent to the Bi layer is also shown. The Fermi energy E_F estimated from the experimental SdH oscillation is denoted by the shaded area in (a). For details, see supplementary Fig. 6.10

6.3 First-principle calculation

First-principles calculations indeed reproduce such a marked dependence of the band structure on the magnetic state, as shown in Fig. 6.9, where the Dirac-like bands near E_F are displayed.Note that two sets of bands arise from the unit cell doubling along the c axis to represent the AFM order of Eu moments, which is adopted to the forced FM state in common.In addition to a small change upon the spin flop of the Eu moments [Figs. 6.9(a) and (b)], the splitting of red-colored (spin up) and blue-colored (spin down) bands progressively evolves, as the net magnetization (i.e., the canting of the Eu moment) increases in the spin-flop AFM phase [Figs. 6.9(b)−(d)]. Since the present calculation does not take E_Z into consideration, this large spin splitting originates from the exchange coupling of the Dirac fermion with the local Eu moments (E_{ex}), which can be expressed as $E_{ex} = J\langle S \rangle = J\chi H/g_J$, where J is the exchange integral, $\langle S \rangle$ is the component of Eu^{2+} spin along the field, $g_J(= 2)$ is the Landé g factor for Eu^{2+}, and χ is the magnetic susceptibility. In the AFM phase,

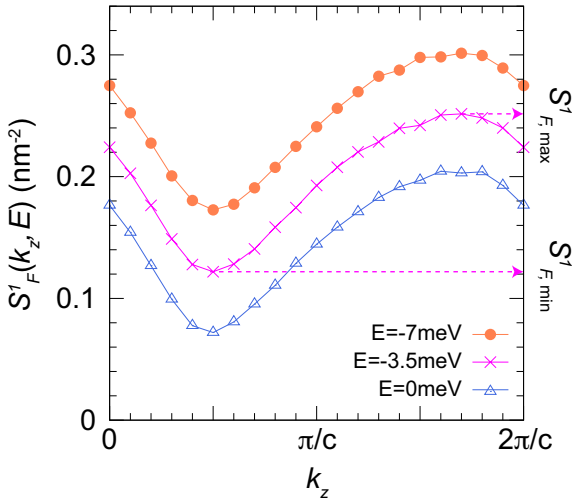

Fig. 6.10 Calculated k_z dispersion of $S^1_F(k_z, E)$ where E is 0, -3.5, and -7 meV. $S^1_{F,\max}(E)$ and $S^1_{F,\min}(E)$ are shown for $E = -3.5$ meV.

since the field is parallel to the easy axis of Eu spins, χ is a small parallel susceptibility and hence $E_{\rm ex}$ is negligible. On the other hand, in the spin-flop AFM phase, where the Eu spin axis changes to be transverse to the field, χ corresponds to a much larger transverse susceptibility.From the magnetization data[43], we have estimated $\chi_{||}$ and $\chi_\perp$ to be 5.4×10^{-3} and 1.4×10^{-1} emu/mol at 2 K, respectively. In the latter phase, the Landau level splitting is caused by $E_{\rm ex}$ as well as $E_{\rm Z}$, which renormalizes the g^* value. From the energy splitting shown in Fig. 6.9(d), we obtain $E_{\rm ex} = 50-80$ meV for $\langle S\rangle$=7/2 (i.e., $J = 14-23$ meV), which is comparable to (or even larger than) $E_{\rm Z} \sim 13$ meV at $H = H_{\rm c} \sim 22$ T for $g^* \sim 10$. Thus, the exchange coupling should appreciably contribute to the observed apparent change in g^* upon the AFM phase. The reduction of g^* in the spin-flop AFM phase implies that the sign of J is opposite to that of pristine g^*, although a more quantitative estimation of these parameters is a future subject.

Here, by comparing the experimentally determined value of S_F for the AFM phase (0.186 nm^{-2} in Table 1) to the first-principles calculation, we have estimated the Fermi energy $E_F^{\rm expt.}$, as shown in Fig. 4(a) in the main text. We here consider two cases: (i) the Fermi energy crosses only the highest valence band and (ii) the Fermi energy crosses the highest and the second highest valence bands. Since the size of the band splitting between the highest and the second highest valence bands is highly sensitive to the calculation details [e.g., see Figs. 4(a) and 4(b) in the main text], it is quite difficult in the present calculation to determine whether the Fermi energy crosses the second highest valence band or not.

Because a very fine $\boldsymbol{k}$-mesh is required for this evaluation, we employed an effective tight-binding model. We extracted the Wannier functions [109, 110] from the cal-

culated band structure using the WIEN2WANNIER [111] and WANNIER90 [112] codes. We took the Eu-f, Mn-d, and Bi-p orbitals as the Wannier basis set. Then, we constructed a tight-binding model with the obtained hopping parameters among these Wannier functions. Using this model, we estimated the values of $S_F^{1,2}(k_z, E)$ using a 1600×1600 $\boldsymbol{k}$-mesh for the (k_x, k_y) plane at each k_z. Here, the upper scripts 1 and 2 denote the highest and the second highest valence bands, respectively. The k_z dispersion of $S_F^1(k_z, E)$ is shown in Fig. 6.10 for E=0, -3.5, and -7 meV, where the energy origin is in common with that shown in Fig. 4(a) in the main text (see [48] in the main text for detail). As shown in Fig.6.10, $S_F^{1,2}(k_z, E)$ takes the maximum and minimum values with respect to k_z, which are denoted as $S_{F,\max}^{1,2}(E)$ and $S_{F,\min}^{1,2}(E)$, respectively.

From these calculated S_F values, we made an estimation of the experimental Fermi energy $E_F^{\text{expt.}}$ by the following way. For the case (i), where the Fermi energy crosses only the highest valence band, we assumed

$$S_F^{\text{expt.}} = \frac{S_{F,\max}^1(E_F^{\text{expt.}}) + S_{F,\min}^1(E_F^{\text{expt.}})}{2}, \tag{6.1}$$

while we assumed

$$S_F^{\text{expt.}} = \sum_{i=1}^{2} \frac{S_{F,\max}^i(E_F^{\text{expt.}}) + S_{F,\min}^i(E_F^{\text{expt.}})}{4}, \tag{6.2}$$

for the case (ii), where the Fermi energy crosses the highest and the second highest valence bands. The obtained $E_F^{\text{expt.}}$ values for the case (i) and (ii) are approximately -3.5 and -13.5 meV, respectively. Since the valence-band top is located at $E = +18$ meV in the present band calculation, the actual Fermi energy is considered to be approximately in the range of -20 to -30 meV when measured from the valence-band top. This plausible range for the experimental Fermi energy is shown in Fig. 4(a) in the main text.

6.4 Calculated spin-split Landau levels and SdH oscillations of Dirac fermion

Due to the Dirac-like linear energy dispersion, the Landau level spacing in the present system is not uniform and proportional to $\sqrt{H_\perp}$.Then E_Z/E_C depends on the magnetic field and Landau indices, making the situation more complicated. In the following, we calculate the spin-split Landau level energies and discuss the field-direction dependence of the SdH oscillations for the present system.

For this purpose, we adopted the effective Hamiltonian of the 2D Dirac fermion in $SrMnBi_2$[66], which should hold for $EuMnBi_2$ with the same crystal structure. This is constructed for a 2-dimensional layer consisting of the Bi^{-1} square lattice and

the coordinating Sr^{2+} (or Eu^{2+}) ions on the basis of the DFT calculations and the tight-binding analysis. The resultant effective Hamiltonian is given as

$$H^{eff} = \hbar v_1 k_1 \sigma_z + \hbar v_2 k_2 \sigma_x = \begin{pmatrix} \hbar v_1 k_1 & \hbar v_2 k_2 \\ \hbar v_2 k_2 & -\hbar v_1 k_1 \end{pmatrix} \tag{6.3}$$

Here, $k_{1,2}$ are the unit vectors defined locally at the Dirac point (k_0, k_0) as $k_1 = (k_x + k_y)/\sqrt{2}$ and $k_2 = (-k_x + k_y)/\sqrt{2}$. $v_{1,2}$ are the Fermi velocities along the local unit vectors $k_{1,2}$. The Pauli matrices $\sigma_{x,z}$ refer to a pseudospin degree of freedom arising from the Bi sublattices. The spin degree of freedom does not appear in H^{eff} because the spin-orbit coupling (SOC) has nothing to do with the formation of the Dirac electronic structure. H^{eff} is transformed by the standard Peierls substitution to calculate the Landau levels in the magnetic field. By adding the Zeeman term to H^{eff}, the Landau level energies are obtained as follows:

$$E_{N\sigma} = \pm v_F \sqrt{2e\hbar N B_\perp} + \frac{1}{2}\sigma E_Z \tag{6.4}$$

Here, $v_F = \sqrt{v_1 v_2}$ is the average Fermi velocity, μ_0 is the magnetic permeability, and $\sigma = \pm 1$ is the spin index. The first term is the well known Landau levels from the Dirac band and the Zeeman effect simply splits these Landau levels into two spin levels. In addition, the SOC may play a role in the Landau levels for the present compound, because it leads to a small energy gap ($\sim$ 50 meV) at the Dirac point (Fig. 4 in the main text). However, Eq. 6.4 appears to work fine as a first order approximation for the calculation of spin-split Landau levels away from the Dirac point, as demonstrated by the comparison with the experimental data (see the main text).

Now we discuss the angular dependence of the Landau levels and the SdH oscillations. For this, we take the normalized form of the Landau levels energies by dividing Eq. 6.4 by E_F:

$$\frac{E_{N\sigma}}{E_F} = \sqrt{N \frac{H_\perp}{H_F^0}} + \frac{\sigma}{4}\frac{E_Z}{E_C}\frac{H_\perp}{H_F^0} \tag{6.5}$$

Here, E_F is the Fermi energy (*i.e.* chemical potential μ at the zero field) and $H_F^0 = 1/2\mu_0 e\hbar v_F^2$ is the SdH frequency. The cyclotron mass $m_c = E_F/v_F^2$ and the cyclotron energy $E_C = e\hbar\mu_0 H_\perp/m_c$ are defined based on the semiclassical theory and E_C characterizes the Landau level spacing near E_F (see Fig. 2(a) in the main text). The Zeeman-cyclotron ratio $E_Z/E_C = g^* m_c/2m_0 \cos\theta$ characterizes the magnitude of Zeeman splitting, which depends on the tilt angle θ. In the following, we investigate the E_Z/E_C dependence of the Landau level energies to discuss the angular dependence of the SdH oscillations.

The Landau levels for small spin splitting ($E_Z/E_C = 0.2$) are shown in Fig. 6.11 (e). The density of states at the chemical potentail $D(\mu)$, whose oscillatory part is

proportional to the SdH oscillations in the interlayer conductivity σ_{zz}, is also shown in Fig. 6.11 (d). In the calculation of μ and $D(\mu)$, we assumed constant carrier density, zero temperature and Gaussian Landau level broadening of the width $\Gamma = 0.06E_F$. As the field $H_\perp$ increases, Landau levels $E_{N\sigma}$ increase and traverse μ at the fields $H_{N\sigma}$ to give the maxima in $D(\mu)$, where $H_{N\sigma}$ is given as $\frac{H_F}{H_{N\sigma}} = \left[\frac{\sqrt{N}+\sqrt{N-\sigma E_Z/E_C}}{2}\right]^2$.

Figure 6.11(c) displays the color plot of the calculated $D(\mu)$ as functions of E_Z/E_C and $H_\perp$, where the values of $H_{N\sigma}$ are plotted together as solid ($\sigma = +$) and dashed ($\sigma = -$) lines. For small spin splitting (i.e. small E_Z/E_C) the peaks in $D(\mu)$ from $(N,+)$ and $(N,-)$ levels are overlapped with each other, whereas those from $(N,+)$ and $(N+1,-)$ levels are well separated. As a result, $D(\mu)$ shows maxima from $(N,+)$ and $(N,-)$ levels at the integer filling factors $H_F^0/H_\perp = N$ as shown in Fig. 6.11 (d). When E_Z/E_C is larger than 1/2, $1/H_{N+}$ is well separated from $1/H_{N,-}$ and rather close to $1/H_{N+1,-}$. In this case, the peaks in $D(\mu)$ from $(N,+)$ and $(N+1,-)$ levels are overlapped each other to form the $D(\mu)$ maxima at the half-integer filing factors $H_F^0/H_\perp = N + 1/2$ (Fig. 6.11 (a,b)). Thus the maxima and minima in $D(\mu)$ are inverted for $E_Z/E_C < 1/2$ and $E_Z/E_C > 1/2$. Interestingly, the inversion of the oscillations described above occurs simultaneously for all N when E_Z/E_C exceeds 1/2 as shown in Fig. 6.11 (c), even though the energy separation between E_{N+} and $E_{N+1,+}$ depends on N and is proportional to $\sqrt{H_\perp}$, not $H_\perp$.

6.5 Summary for Chap.6

In conclusion, we observed spin-split Landau levels of quasi-two-dimensional Dirac fermions in a bulk antiferromagnet $EuMnBi_2$, which markedly depend on the field-tunable magnetic order of Eu moments. In addition to Zeeman splitting relevant to the large g factor, the Dirac-like band exhibits substantial exchange splitting due to the coupling with the local Eu moments. Such an interplay of the spin-orbit and exchange interactions in the present compound yields novel correlated Dirac fermion states in a solid, offering a promising approach to emerging topological spintronics.

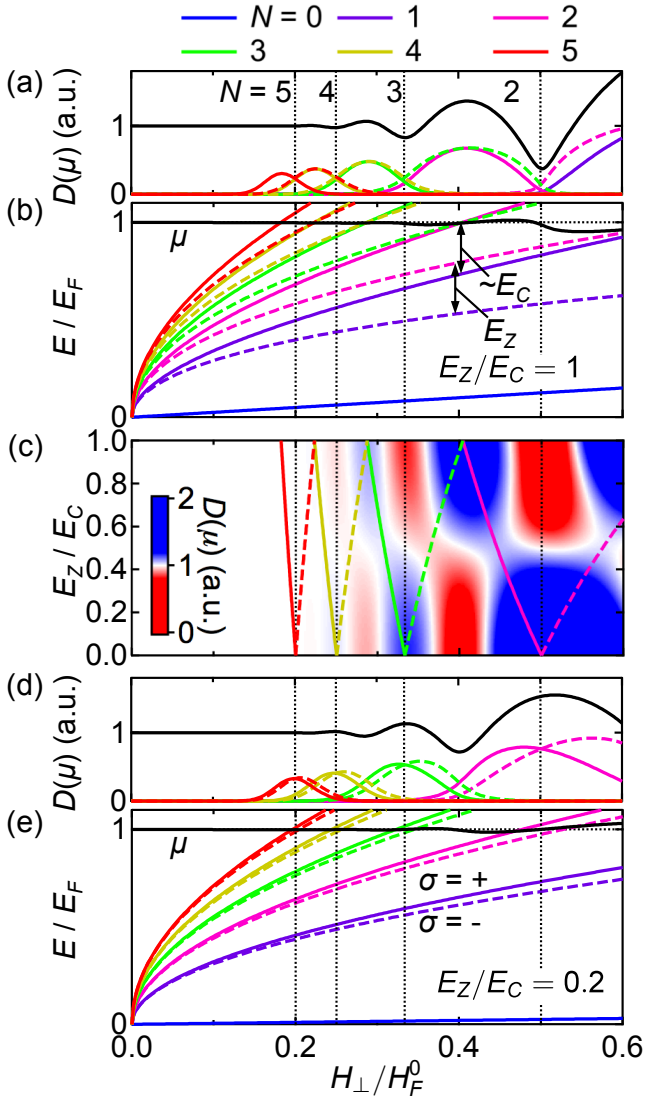

Fig. 6.11 Energy levels of spin-split Landau levels for 2-dimensional Dirac fermion. (a) The density of states at the chemical potential $D(\mu)$ as a function of out-of-plane field $H_\perp$ for large spin splitting ($E_Z/E_C = 1$). Contributions from each Landau levels are also shown for $0 \leq N \leq 5$. Landau level index N is specified by the colors and the spin index σ by the solid and dashed lines. Vertical dotted lines show the fields of integer filling factors $H_\perp/H_F^0 = 1/2, 1/3, \ldots$. (b) Landau levels $E_{N\sigma}$ as a function of out-of-plane field $H_\perp$ for $E_Z/E_C = 1$. The chemical potential μ is also shown. (c) Image plot of $D(\mu)$ as functions of $H_\perp$ and E_Z/E_C. Solid and dashed curves show $H_{N\sigma}/H_F^0$, where $H_{N\sigma}$ is the fields at which $E_{N\sigma}$ traverse E_F. (d) $D(\mu)$ and (e) $E_{N\sigma}$, μ for small spin splitting ($E_Z/E_C = 0.2$).

Chapter 7

General discussion

7.1 Impact of Eu magnetic order on the Dirac fermion in $EuMnBi_2$

In this section, we comprehensively discuss the impact of the Eu magnetic order on the Dirac electronic structure, based on the results given in the previous sections. Fig. 7.1 show the schematic crystal and magnetic structures of $EuMnBi_2$ for the

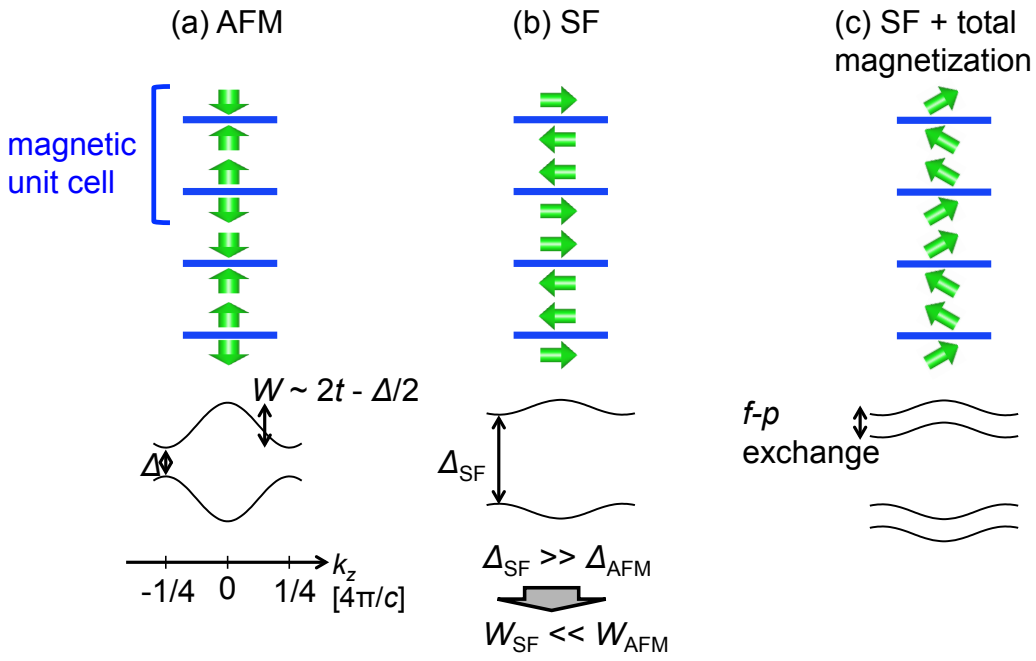

Fig. 7.1 Schematic description of the crystal and magnetic structure, and the corresponding Dirac band structure fro the (a) AFM and (b, c) SF phases. The Eu moments are canted parallel to the external magnetic field $H||c$ for (c).

AFM and SF (spin-flop AFM) phases. In the AFM phase, the Eu magnetic order breaks the body-centered translational symmetry of the underlying crystal as shown in Chap. 5.1. Here, each magnetic unit cell contains two Bi square net layers. As a result, two sets of Dirac bands appear due to the folding of the Dirac bands as depicted in Fig. 7.1. The Fermi level crosses only the higher Dirac hole band to form a quasi-two-dimensional Fermi surface in the AFM phase. In the SF phase, the gap Δ between the two Dirac bands are enhanced, leading to the suppression in the bandwidth W of the higher Dirac hole band as we discussed in Chap. 5.2. This result in the enhancement in the interlayer resistivity ρ_{zz}, which was described in Chap. 4. Furthermore, the suppression of W induces the quantum Hall gap between the Landau subbands (see Fig. 5.14), leading to the bulk multilayer quantum Hall effect described in Chap. 4. The mechanism of the enhancement in Δ in the SF phase is suggested to be an additional hybridization between the Bi p_x and p_y orbitals on the adjacent layers via the Eu moments oriented along the a or b direction. The strong spin-orbit coupling of Bi is likely playing a crucial role.

In the SF phase, the Eu moments are canted parallel to the external magnetic field $H||c$ to arise a finite total magnetization. Here, the Dirac fermions are subject to the exchange field due to the exchange coupling the Dirac fermion and the Eu moments. The exchange field induces spin splitting of the Dirac band, which was signified by the difference in the magnitude of the spin splitting of the Landau levels in the AFM and SF phases as revealed in Chap. 6.

7.2 $EuMnBi_2$ compared to other magnetic Dirac materials

In this section, we compare $EuMnBi_2$ with other magnetic Dirac materials to clarify the characteristic of $EuMnBi_2$ outstanding from other magnetic Dirac materials.

We compare the physical properties of several magnetic Dirac materials in Tab. 7.1 and Fig. 7.2. In Fig. 7.2 we plot the magnitude of the coupling energy between the Dirac fermion and the magnetic order (e.g. exchange coupling energy) against the carrier mobility.

The most outstanding feature of $EuMnBi_2$ is the high carrier mobility of $\sim 14,000$ cm^2/Vs. This mobility is extremely large among the magnetic Dirac materials showing strong coupling between the Dirac electronic state and the magnetic order. Since the high mobility is the most outstanding feature of the Dirac materials, the compatibility of the high mobility of the Dirac fermion and its strong coupling to the magnetic order makes $EuMnBi_2$ an ideal Dirac material.

There are two reasons that the Dirac fermions of $EuMnBi_2$ show high mobility. First, the magnetic moments are localized to the Eu site, which is separated from the Bi^{-1} sites hosting the Dirac fermion. For correlated (semi-)metals such as Mn_3Sn and $R_2Ir_2O_7$, on the other hand, the conducting carriers arise from the strongly correlated orbitals (e.g. Mn $3d$ orbital for Mn_3Sn) hosting magnetic moments. Hence the carrier mobility is as low as ~ 1 cm^2/Vs. Second, the conducting Dirac band originates from

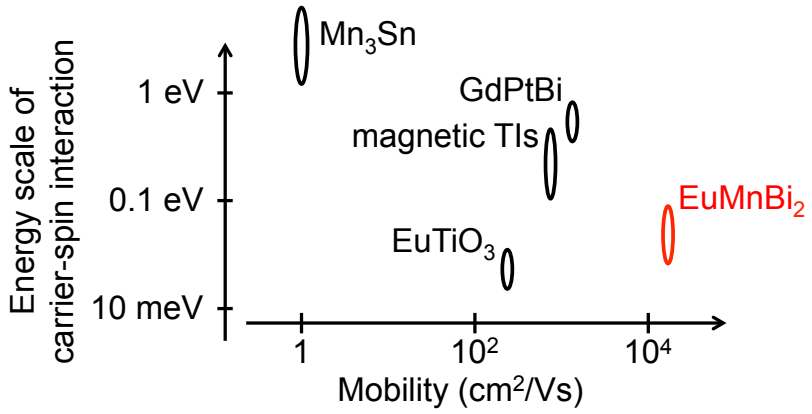

Fig. 7.2 Mobility and the energy scales of the electron-spin interaction. For GdPtBi, magnetic topological insulators (TIs), $EuTiO_3$ and $EuMnBi_2$, the exchange coupling energy in the forced ferromagnetic state is plotted in the vertical axis. For $EuMnBi_2$, the gap between the two Dirac bands induced by the magnetic order (5 - 40 meV; see Sec. 5.1) is also plotted.

Tab. 7.1

material	carrier-density (cm^{-3})	mobility (cm^2/Vs)	conducting orbit	magnetic orbit
$EuMnBi_2$	3×10^{19}	14,000	Bi $6p$	Eu $4f$
Cr-$(Bi,Sb)_2(Te,Se)_3$		760	Bi $6p$, Se $4p$	Cr $3d$
Mn_3Sn	4×10^{22}	~ 1	Mn $3d$	Mn $3d$
GdPtBi	$\sim 10^{18}$	$\sim 1,500$	Bi $6p$	Gd $4f$
$EuTiO_3$ thin film	10^{19} - 10^{21}	~ 200	Ti $3d$	Eu $4f$

the Bi p_x, p_y orbitals, which forms covalent-type bondings to realize a highly dispersing bands. Therefore the Dirac fermion with a quite high Fermi velocity is realized in $EuMnBi_2$. For this reason, a Dirac electronic state having a very high Fermi velocity is realized. On the other hand, in other magnetic Dirac materials such as GdPtBi, although the conducting orbitals are different from the orbitals responsible for the magnetism, the conducting orbitals do not form chemical bonds and the bands near the Fermi level are relatively weakly dispersive. Hence the mobilities are about 100 to 1000 cm^2/Vs, which are sufficiently smaller than hat in $EuMnBi_2$.

Another feature of the magnetic Dirac material $EuMnBi_2$ lies in the mechanism of the coupling between the Dirac fermion and the magnetism. In $EuMnBi_2$, the unit cell doubling and the corresponding folding of the Dirac band, as well as the exchange coupling between the Dirac fermion and the Eu moments, play crucial roles

on the coupling of the Dirac fermion with the magnetic order. On the other hand, in many magnetic Dirac materials such as magnetic topological insulators and GdPtBi, the exchange coupling mechanism is the only mechanism of the coupling between the magnetic order and the magnetism. Hence, we have proposed through a research on $EuMnBi_2$ a new mechanism of the coupling between the Dirac fermion and the magnetism, which should be called as "band folding mechanism".

Chapter 8

Summary and conclusion

In this thesis, we explored novel magnetotransport phenomena arising from the coupling between the Dirac fermions in solids and the magnetic order. We focused on the Dirac material with Bi square net and tried to functionalize them by chemical substitutions. Especially, we focused on $EuMnBi_2$ and revealed the strong coupling between the Dirac fermion and the antiferromagnetic order of Eu.

Chapter 4: Discovery of the novel magnetic Dirac material $EuMnBi_2$

In this study, we have focused on a layered bulk antiferromagnet $EuMnBi_2$, where the Bi square nets hosting quasi-2D Dirac fermion and the magnetic insulating layers stack alternatively, and demonstrated that the quantum transport of Dirac fermions is highly enriched by Eu antiferromagnetic(AFM) order. Below the AFM transition temperature, external magnetic field induces spin-flop transition of Eu moments, which suppresses the interlayer coupling between the Bi layers and dramatically enhances interlayer resistivity ρ_{zz}. Furthermore, this high-ρ_{zz} state is accompanied by plateau-like structures in the Hall resistivity and giant SdH oscillations, which signify the quantum Hall effect in a bulk magnet.

Chapter 5: Magnetic structure of $EuMnBi_2$

We have presented an investigation of the magnetic structure in $EuMnBi_2$ by the single crystal neutron diffraction and the resonant x-ray magnetic diffraction measurements. Mn moments show checkerboard-type AFM order with an antiferromagnetic arrangement for both the in-plane and out-of-plane nearest neighbors, with moments parallel to the c axis. Eu moments show antiferromagnetic order where ferromagnetic layers within the ab plane are stacked antiferromagnetically along the c axis in the sequence of up-up-down-down. Eu moments are aligned parallel to the c axis in the AFM phase, while they are reoriented parallel to the a or b axis with spin-flop domains. Mn magnetic structure is unaffected by the reorientation of the Eu moments within the experimental accuracy. These results offer a concrete basis to reveal the coupling between the Dirac fermion and the magnetic order in $EuMnBi_2$ in future studies.

Chapter 6: Landau level splitting modulated by the antiferromagnetic order in $EuMnBi_2$
We report spin-split Landau levels of quasi-two-dimensional Dirac fermions in a layered antiferromagnet $EuMnBi_2$, as revealed by interlayer resistivity measurements in a tilted magnetic field up to $\sim$35 T. The amplitude of Shubnikov-de Haas (SdH) oscillation in interlayer resistivity is strongly modulated by changing the tilt angle of the field, i.e., the Zeeman-to-cyclotron energy ratio. The effective g factor estimated from the tilt angle, where the SdH oscillation exhibits a phase inversion, differs by approximately 50% between two antiferromagnetic phases. This observation signifies a marked impact of the magnetic order of Eu sublattice on the Dirac-like band structure. The origin may be sought in strong exchange coupling with the local Eu moments, as verified by the first-principles calculation.

We have discovered the magnetic Dirac material $EuMnBi_2$ and revealed that the transport properties and electronic structures of the high-mobility Dirac fermion in $EuMnBi_2$ is highly modulated by the magnetic order of the Eu moments tuned by the external magnetic field. The outstandingly high mobility of $\sim 14,000$ cm^2/Vs and the controllability of the Dirac fermion via the field-tunable magnetic order together makes $EuMnBi_2$ a unique system as a magnetic Dirac material. We believe that the present study contribute to the basis of the future electronics and spintronics.

A

Physical properties of other $AM\mathrm{Bi}_2$ phases (A = Eu, Sr, Ba, M = Zn, Cd)

Figure A.1 shows the XRD patterns of several $AM\mathrm{Bi}_2$ phases (A = Sr, Ba, Eu, M = Zn, Cd). The XRD profiles indicate that the crystal structure is tetragonal ($I4/mmm$) for all the materials. The lattice parameters obtained from the Le Bail fitting is shown in Tab. A.1.

Figure A.2 show the temperature dependence of the in-plane (ρ_{xx}) and interlayer (ρ_{zz}) resistivity. The resistivity is metallic for all the materials. The interlayer resistivity ρ_{zz} for (Sr, Eu)(Zn, Cd)Bi_2 is about two orders of magnitude smaller than

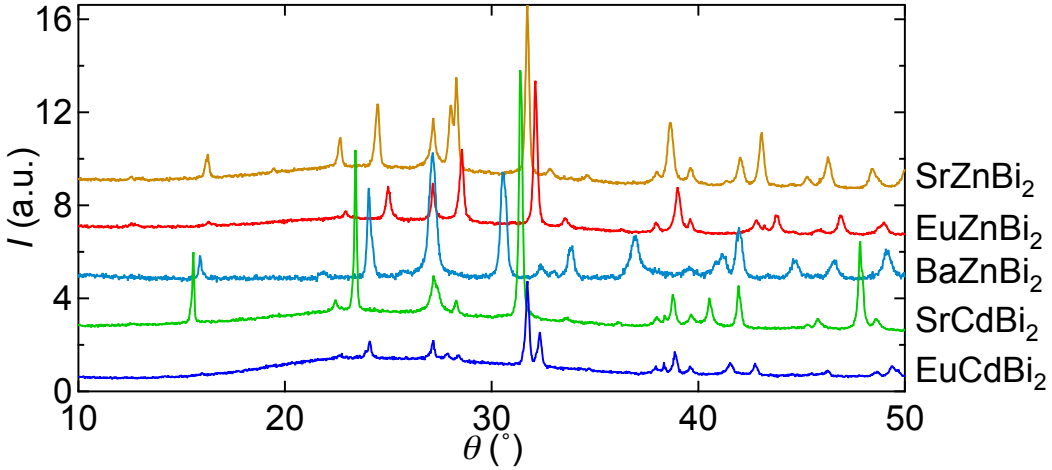

Fig. A.1 powder XRD patterns of SrZnBi_2, EuZnBi_2, BaZnBi_2, EuCdBi_2, SrCdBi_2.

Tab. A.1 Lattice constants of $AM\mathrm{Bi}_2$ phases (A = Sr, Ba, Eu, M = Zn, Cd)

	a (Å)	c (Å)
$SrCdBi_2$	4.6476(2)	22.830(1)
$EuCdBi_2$	4.6314(2)	22.143(1)
$BaZnBi_2$	4.8561(3)	22.0268(13)
$SrZnBi_2$	4.6609(3)	21.824(2)
$EuZnBi_2$	4.6170(3)	21.354(2)

that for(Sr, Eu)$MnBi_2$, indicating that the resistive anisotropy is much smaller for (Sr, Eu)(Zn, Cd)Bi_2. For Eu(Zn, Cd)Bi_2 clear anomalies are observed both in ρ_{xx} and ρ_{yx} at $T_N \sim 20$ K, corresponding to the antiferromagnetic order of the Eu.

Figure A.3 (a, b) show the first-principles calculation results for $SrCdBi_2$ and $SrZnBi_2$, respectively. A Dirac-like linear dispersion appears close to the Fermi level for both systems as denoted by the red circles. Furthermore, bands other than the Dirac band cross the Fermi level around the Γ point to form relatively three-dimensional Fermi surfaces. These three-dimensional Fermi surfaces are likely responsible for the weak resistive anisotropy for (Eu, Sr)(Zn, Cd)Bi_2.

In order to experimentally confirm the existence of the Dirac fermion we performed the magnetoresistance and Hall resistivity measurements (Fig. A.4). (Sr, Eu)$CdBi_2$ show large linear magnetoresistance effect reaching $\rho(9\ \mathrm{T})/\rho(0\ \mathrm{T}) \sim 70$ at 1.9 K. This magnetoresistance is comparable to that of $EuMnBi_2$ and likely arises from the high mobility of the Dirac fermion, supporting the Dirac fermion state in (Eu,Sr)$CdBi_2$. (Eu, Sr)$ZnBi_2$ show much weaker magnetoresistance effect, possibly because the mobility is low due to the poor crystal quality (note that RRR of (Sr, Eu)$ZnBi_2$ is as low as ~ 2; see Fig. A.2). The Hall resistivity ρ_{yx} of (Eu, Sr)(Zn,Cd)Bi_2 is small compared to that of $EuMnBi_2$ and shows nonlinear behavior, supporting the multi-carrier nature of (Eu, Sr)(Zn,Cd)Bi_2

Figure A.5(a) shows the SdH signature of $EuCdBi_2$ observed in the interlayer magnetoresistance ρ_{zz} at 1.9 K. Utilizing the standard Fan diagram analysis (Fig. A.5[b]), we obtained relatively small SdH frequency of $F = 76$ T and the phase factor of $\gamma \sim 0.1$. These results indicate that the observed SdH oscillations arise from the Dirac-like carrier in $EuCdBi_2$.

Finally, we comment on the hysteretic anomaly at T 200 K observed for $SrCdBi_2$. Figures A.6 (a-c) shows the temperature dependence of the resistivity ρ_{xx}, the Seebeck coefficient S and the thermal conductivity κ for $SrCdBi_2$. All of them show clear anomaly at $T \sim 200$ K, suggesting that there occurs some phase transition. Since $SrCdBi_2$ do not host magnetic element, this transition can not be related to the magnetic order. In FIg. A.6(c) we also plot the electron thermal conductivity $\kappa_{el} = \frac{\pi^2 k_B^2}{3e^2} \frac{T}{\rho_{xx}}$ obtained using the Wiedemann-Franz law and the phonon thermal conductivity $\kappa_{ph} = \kappa - \kappa_{el}$. Interestingly, κ_{ph} shows almost no anomaly around 200

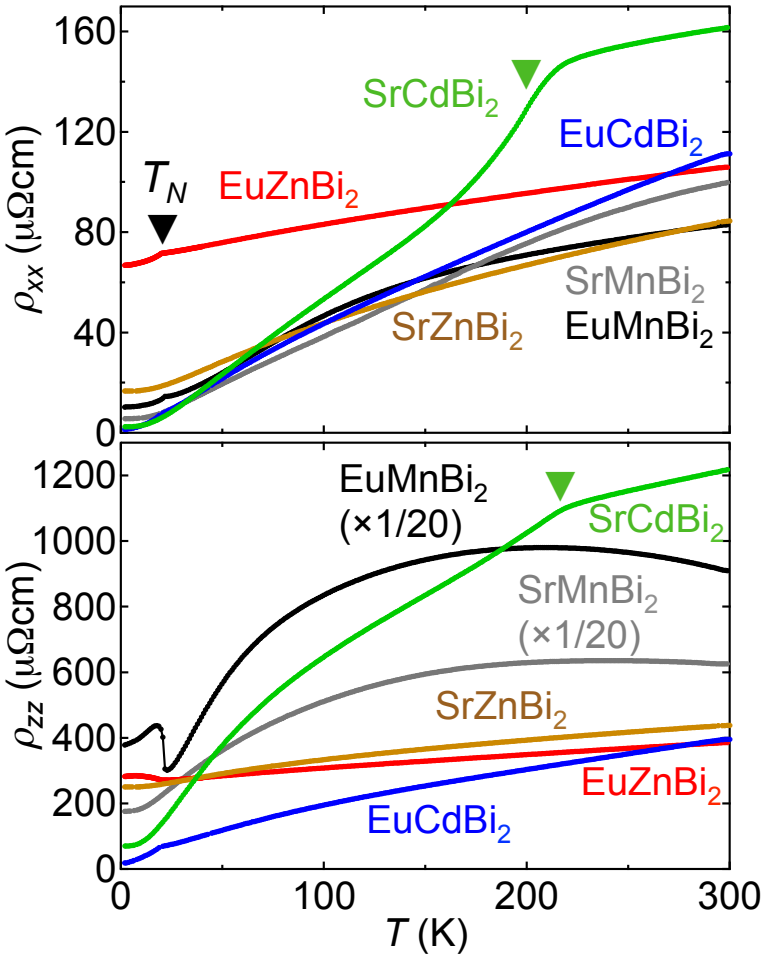

Fig. A.2 Temperature dependence of the (a) In-plane resistivity ρ_{xx} and (b) interlayer resistivity ρ_{zz} of $AM\mathrm{Bi}_2$ phases (A = Sr, Eu, M = Mn, Zn, Cd)

K. This result indicates that this transition does not involve any structural distortion. Hence, the anomaly at ~ 200 K arises from some transition of electronic origin exemplified by the CDW order. However, since ρ_{xx} decreases below the transition temperature, this transition is not explained by the simple CDW order. The origin of the transition is to be clarified in future works.

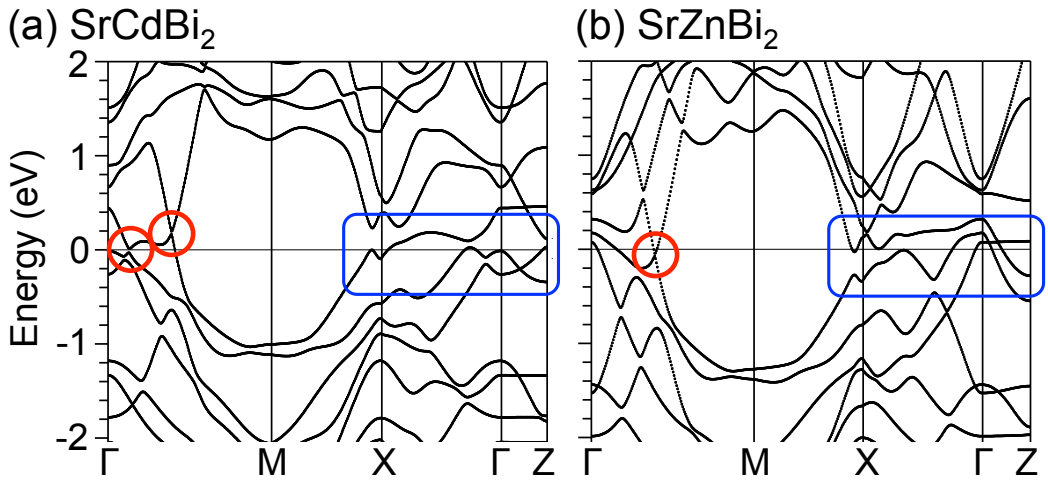

Fig. A.3 Calculated band structures of (a) SrCdBi_2 and (b)SrZnBi_2.

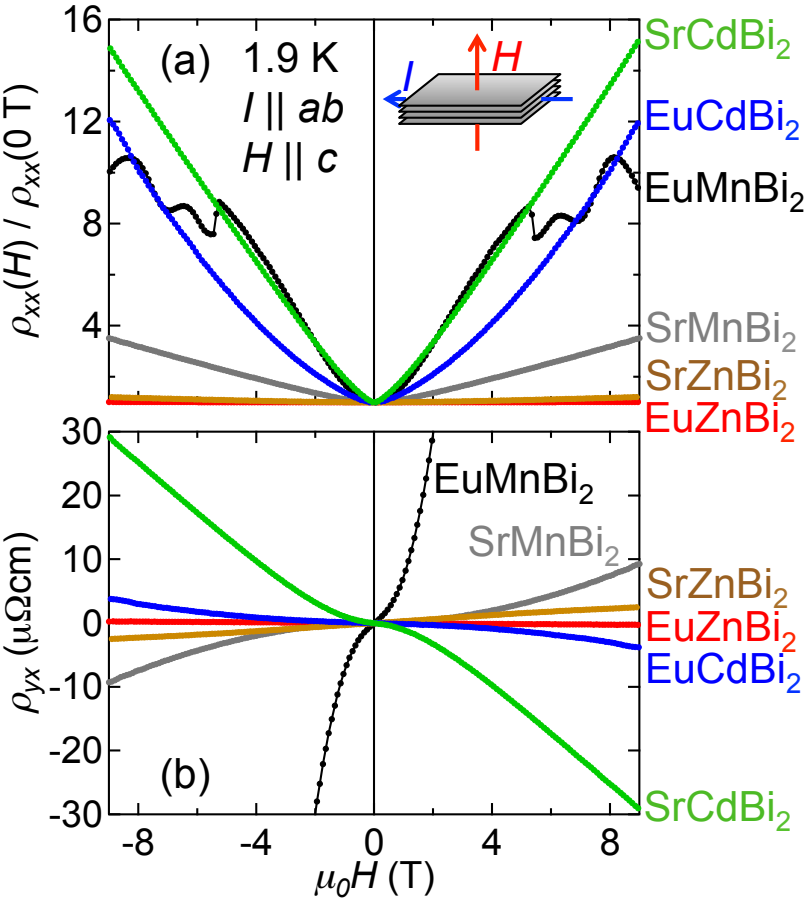

Fig. A.4 Magnetic field ($H||c$) dependence of the (a) In-plane resistivity ρ_{xx} and (b) Hall resistivity ρ_{yx} of $AM\mathrm{Bi}_2$ phases (A = Sr, Eu, M = Mn, Zn, Cd).

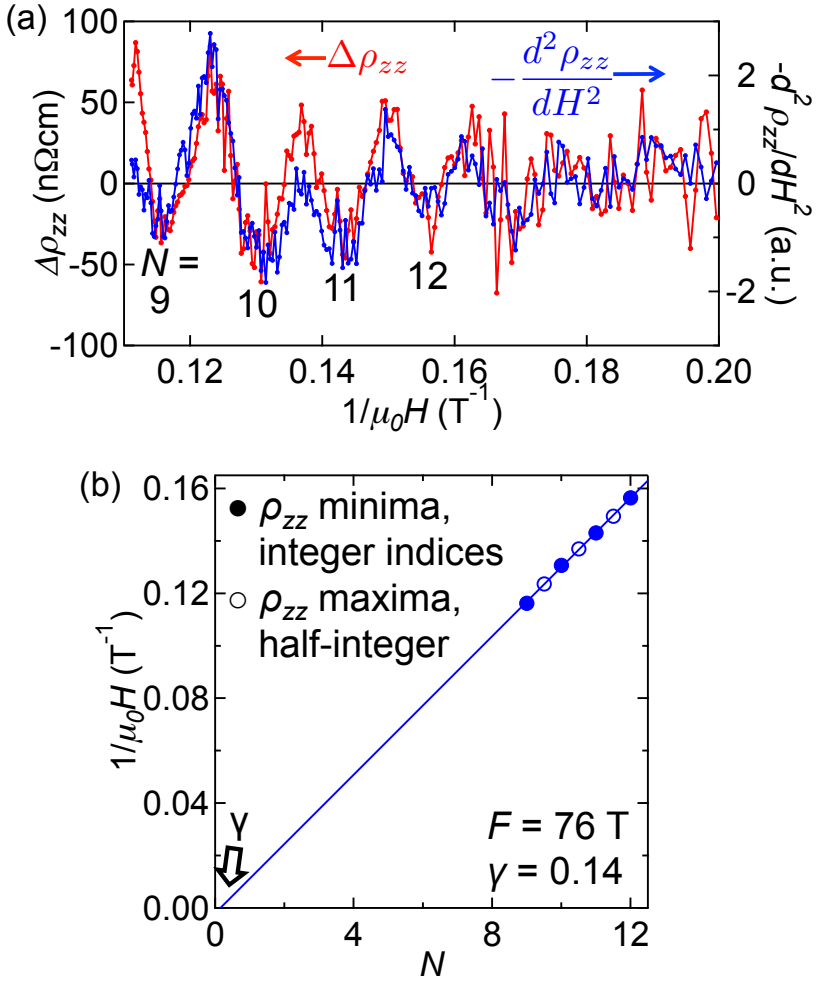

Fig. A.5 (a) Oscillatory interlayer resistivity $\Delta\rho_{zz}$ and second-field-derivative interlayer resistivity $-d^2\rho_{zz}/dH^2$ as a function of inverse magnetic field. (b) Fan diagram of the SdH oscillation in EuCdBi_2.

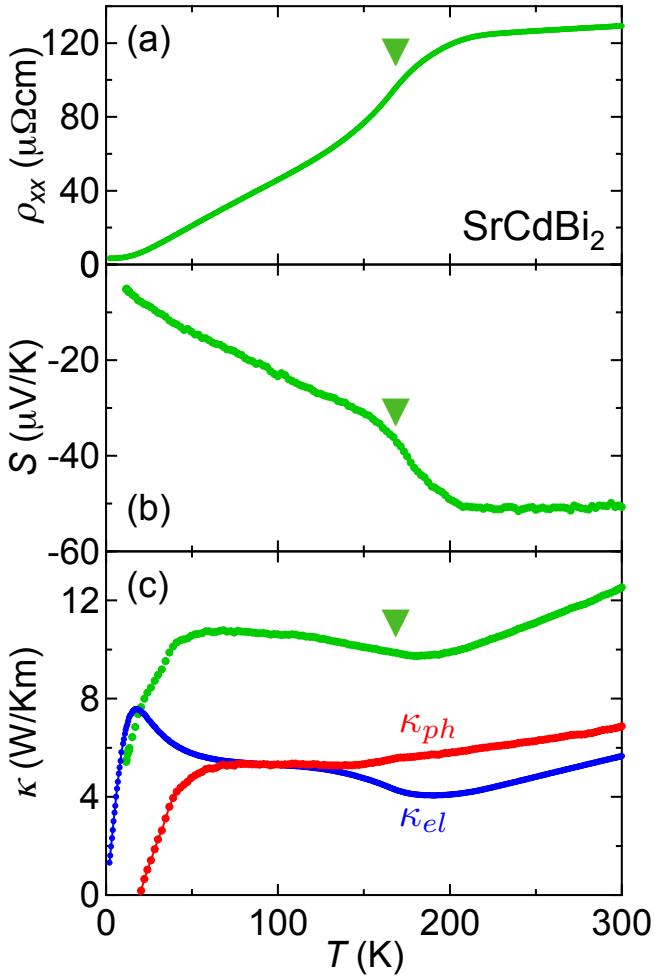

Fig. A.6 Temperature dependence of the in-plane (a) resistivity ρ_{xx}, (b) Seebeck coefficient S and (c) thermal conductivity κ. $\kappa_{el} = \frac{\pi^2 k_B^2}{3e^2}\frac{T}{\rho_{xx}}$ is the electron thermal conductivity obtained from the Wiedemann-Franz law and $\kappa_{ph} = \kappa - \kappa_{el}$ is the phonon thermal conductivity.

Bibliography

[1] J. C. Meyer, A. K. Geim, M. I. Katsnelson, K. S. Novoselov, T. J. Booth, and S. Roth, Nature 446, 60 (2007).

[2] A. H. Castro Neto, F. Guinea, N. M. R. Peres, K. S. Novoselov, and A. K. Geim, Rev. Mod. Phys. 81, 109 (2009).

[3] K. Kajita, Y. Nishio, N. Tajima, Y. Suzumura, and A. Kobayashi, J. Phys. Soc. Japan 83, 1 (2014).

[4] X.-L. Qi and S.-C. Zhang: Reviews of Modern Physics 83 (2011) 1057.

[5] Y. Ando: Journal of the Physical Society of Japan 82 (2013) 1.

[6] 安藤陽一: トポロジカル絶縁体入門 (講談社, 2014).

[7] R. Yoshimi, A. Tsukazaki, Y. Kozuka, J. Falson, K. Takahashi, J. G. Checkelsky, N. Nagaosa, M. Kawasaki, and Y. Tokura: Nature Communications 6 (2015) 6627.

[8] Z. Wang, H. Weng, Q. Wu, X. Dai, and Z. Fang: Physical Review B 88 (2013) 125427.

[9] M. Neupane, S.-Y. Xu, R. Sankar, N. Alidoust, G. Bian, C. Liu, I. Belopolski, T.-R. Chang, H.-T. Jeng, H. Lin, A. Bansil, F. Chou, and M. Z. Hasan: Nature Communications 5 (2014) 1.

[10] Z. Wang, Y. Sun, X.-Q. Chen, C. Franchini, G. Xu, H. Weng, X. Dai, and Z. Fang: Physical Review B 85 (2012) 195320.

[11] Z. K. Liu, B. Zhou, Y. Zhang, Z. J. Wang, H. M. Weng, D. Prabhakaran, S.-K. Mo, Z. X. Shen, Z. Fang, X. Dai, Z. Hussain, and Y. L. Chen: Science 343 (2014) 864.

[12] T. Kariyado and M. Ogata: Journal of the Physical Society of Japan 80 (2011) 083704.

[13] T. Kariyado and M. Ogata: Journal of the Physical Society of Japan 81 (2012) 064701.

[14] M. N. Ali, Q. Gibson, S. Jeon, B. B. Zhou, A. Yazdani, and R. J. Cava: Inorganic Chemistry 53 (2014) 4062.

[15] Hongming Weng, Chen Fang, Zhong Fang, B. Andrei Bernevig, and Xi Dai Phys. Rev. X 5, 011029

[16] B. Q. Lv, H. M. Weng, B. B. Fu, X. P. Wang, H. Miao, J. Ma, P. Richard, X. C. Huang, L. X. Zhao, G. F. Chen, Z. Fang, X. Dai, T. Qian, and H. Ding: Physical Review X 5 (2015) 031013.

[17] W. Zdanowicz and L. Zdanowicz: Annual Review of Materials Science 5 (1975) 301.
[18] T. Liang, Q. Gibson, M. N. Ali, M. Liu, R. J. Cava, and N. P. Ong: Nature Materials 14 (2014) 280.
[19] M. I. Katsnelson, K. S. Novoselov, and A. K. Geim: Nature Physics 2 (2006) 620.
[20] K. S. Novoselov, A. K. Geim, S. V. Morozov, D. Jiang, M. I. Katsnelson, I. V. Grigorieva, S. V. Dubonos, and a. a. Firsov: Nature 438 (2005) 197.
[21] Y. Zhang, Y.-W. Tan, H. L. Stormer, and P. Kim: Nature 438 (2005) 201.
[22] K. S. Novoselov, Z. Jiang, Y. Zhang, S. V. Morozov, H. L. Stormer, U. Zeitler, J. C. Maan, G. S. Boebinger, P. Kim, and A. K. Geim: Science 315 (2007) 1379.
[23] T. Osada: Journal of the Physical Society of Japan 77 (2008) 084711.
[24] T. Konoike, M. Sato, K. Uchida, and T. Osada: Journal of the Physical Society of Japan 82 (2013) 1.
[25] J. C. Meyer, A. K. Geim, M. I. Katsnelson, K. S. Novoselov, T. J. Booth, and S. Roth, Nature 446, 60 (2007).
[26] I. Žutić, J. Fabian, and S. Das Sarma, Rev. Mod. Phys. 76, 323 (2004).
[27] T. Miyazaki and N. Tezuka, J. Magn. Magn. Mater. 139, 94 (1995).
[28] N. Nagaosa, J. Sinova, S. Onoda, A. H. MacDonald, and N. P. Ong, Rev. Mod. Phys. 82, 1539 (2010).
[29] M. Imada, A. Fujimori, and Y. Tokura, Rev. Mod. Phys. 70, 1039 (1998).
[30] R. Yu, W. Zhang, H. Zhang, S.-C. Zhang, X. Dai, and Z. Fang, Science (80-.). 329, 61 (2010).
[31] C.-Z. Chang, J. Zhang, X. Feng, J. Shen, Z. Zhang, M. Guo, K. Li, Y. Ou, P. Wei, L.-L. Wang, Z.-Q. Ji, Y. Feng, S. Ji, X. Chen, J. Jia, X. Dai, Z. Fang, S.-C. Zhang, K. He, Y. Wang, L. Lu, X.-C. Ma, and Q.-K. Xue, Science (80-.). 340, 167 (2013).
[32] C.-Z. Chang, W. Zhao, D. Y. Kim, H. Zhang, B. A. Assaf, D. Heiman, S.-C. Zhang, C. Liu, M. H. W. Chan, and J. S. Moodera, Nat. Mater. 14, 473 (2015).
[33] J. G. Checkelsky, R. Yoshimi, A. Tsukazaki, K. S. Takahashi, Y. Kozuka, J. Falson, M. Kawasaki, and Y. Tokura, Nat. Phys. 10, 1 (2014).
[34] X. Wan, A. M. Turner, A. Vishwanath, and S. Y. Savrasov, Phys. Rev. B 83, 205101 (2011).
[35] Y. Yamaji and M. Imada, Phys. Rev. X 4, 1 (2014).
[36] E. Y. Ma, Y.-T. Cui, K. Ueda, S. Tang, K. Chen, N. Tamura, P. M. Wu, J. Fujioka, Y. Tokura, and Z.-X. Shen, Science (80-.). 350, 538 (2015).
[37] K. Ueda, J. Fujioka, Y. Takahashi, T. Suzuki, S. Ishiwata, Y. Taguchi, and Y. Tokura, Phys. Rev. Lett. 109, 1 (2012).
[38] G. Cordier and H. Sch ä fer, Zeitschrift F ü r Naturforsch. B 32, 383 (1977).
[39] J. K. Wang, L. L. Zhao, Q. Yin, G. Kotliar, M. S. Kim, M. C. Aronson, and E. Morosan, Phys. Rev. B 84, 064428 (2011).
[40] G. A. Papoian and R. Hoffmann, Angew. Chemie Int. Ed. 39, 2408 (2000).

[41] J. Park, G. Lee, F. Wolff-Fabris, Y. Y. Koh, M. J. Eom, Y. K. Kim, M. A. Farhan, Y. J. Jo, C. Kim, J. H. Shim, and J. S. Kim, Phys. Rev. Lett. 107, 126402 (2011).
[42] K. Watanabe, G. Nishijima, S. Awaji, K. Takahashi, K. Koyama, N. Kobayashi, M. Ishizuka, T. Itou, T. Tsurudome, and J. Sakuraba, IEEE Trans. Appl. Supercond. 16, 934 (2006).
[43] H. Masuda, H. Sakai, M. Tokunaga, Y. Yamasaki, A. Miyake, J. Shiogai, S. Nakamura, S. Awaji, A. Tsukazaki, H. Nakao, Y. Murakami, T. Arima, Y. Tokura, and S. Ishiwata, Science Advances **2**, e1501117 (2016).
[44] A. F. May, M. A. McGuire, and B. C. Sales, Physical Review B **90**, 075109 (2014).
[45] Y. F. Guo, A. J. Princep, X. Zhang, P. Manuel, D. Khalyavin, I. I. Mazin, Y. G. Shi, A. T. Boothroyd, Coupling of magnetic order to planar Bi electrons in the anisotropic Dirac metals A MnBi2 (A = Sr, Ca). Phys. Rev. B 90, 075120 (2014).
[46] G. van der Laan, E. Arenholz, A. Schmehl, D. G. Schlom, Weak anisotropic x-ray magnetic linear dichroism at the Eu M4,5 edges of ferromagnetic EuO(001): Evidence for 4f-state contributions. Phys. Rev. Lett. 100, 067403 (2008).
[47] T. Liang, Q. Gibson, M. N. Ali, M. Liu, R. J. Cava, N. P. Ong, Ultrahigh mobility and giant magnetoresistance in the Dirac semimetal Cd3As2. Nat. Mater. 14, 280 – 284 (2015).
[48] L. P. He, X. C. Hong, J. K. Dong, J. Pan, Z. Zhang, J. Zhang, S. Y. Li, Quantum transport evidence for the three-dimensional Dirac semimetal phase in Cd3As2. Phys. Rev. Lett. 113, 246402 (2014).
[49] A. Narayanan, M. D. Watson, S. F. Blake, N. Bruyant, L. Drigo, Y. L. Chen, D. Prabhakaran, B. Yan, C. Felser, T. Kong, P. C. Canfield, A. I. Coldea, Linear magnetoresistance caused by mobility fluctuations in n-doped Cd3As2. Phys. Rev. Lett. 114, 117201 (2015).
[50] S. K. Kushwaha, J. W. Krizan, B. E. Feldman, A. Gyenis, M. T. Randeria, J. Xiong, S. -Y. Xu, N. Alidoust, I. Belopolski, T. Liang, M. Z. Hasan, N. P. Ong, A. Yazdani, R. J. Cava, Bulk crystal growth and electronic characterization of the 3D Dirac semimetal Na3Bi. APL Mater. 3, 041504 (2015).
[51] M. Novak, S. Sasaki, K. Segawa, Y. Ando, Large linear magnetoresistance in the Dirac semimetal TlBiSSe. Phys. Rev. B 91, 041203(R) (2015)
[52] D. P. Druist, P. J. Turley, K. D. Maranowski, E. G. Gwinn, A. C. Gossard, Observation of chiral surface states in the integer quantum Hall Effect. Phys. Rev. Lett. 80, 365 – 368 (1998).
[53] M. Kuraguchi, T. Osada, Temperature dependence of interlayer surface transport in multilayer quantum Hall system. Physica E 6,594 – 597 (2000).
[54] Y. Zheng, T. Ando, Hall conductivity of a two-dimensional graphite system. Phys. Rev. B 65, 245420 (2002).
[55] V. P. Gusynin, S. G. Sharapov, Unconventional integer quantum Hall effect in

graphene. Phys. Rev. Lett. 95, 146801 (2005).
[56] G. P. Mikitik, Y. V. Sharlai, Manifestation of Berry' s phase in metal physics. Phys. Rev. Lett. 82, 2147 – 2150 (1999)
[57] I. A. Luk' yanchuk, Y. Kopelevich, Dirac and normal fermions in graphite and graphene: Implications of the quantum Hall effect. Phys. Rev. Lett. 97, 256801 (2006)
[58] H. Murakawa, M. S. Bahramy, M. Tokunaga, Y. Kohama, C. Bell, Y. Kaneko, N. Nagaosa, H. Y. Hwang, Y. Tokura, Detection of Berry' s phase in a bulk Rashba semiconductor. Science 342,1490 – 1493 (2013).
[59] H. L. Störmer, J. P. Eisenstein, A. C. Gossard, W. Wiegmann, K. Baldwin, Quantization of the Hall effect in an anisotropic three-dimensional electronic system. Phys. Rev. Lett. 56,85 – 88 (1986).
[60] J. R. Cooper, W. Kang, P. Auban, G. Montambaux, D. J é rome, K. Bechgaard, Quantized Hall effect and a new field-induced phase transition in the organic superconductor (TMTSF)2PF6. Phys. Rev. Lett. 63,1984 – 1987 (1989).
[61] S. T. Hannahs, J. S. Brooks, W. Kang, L. Y. Chiang, P. M. Chaikin, Quantum Hall effect in a bulk crystal. Phys. Rev. Lett. 63, 1988 – 1991 (1989).
[62] S. Hill, S. Uji, M. Takashita, C. Terakura, T. Terashima, H. Aoki, J. S. Brooks, Z. Fisk, J. Sarrao, Bulk quantum Hall effect in h – Mo4O11. Phys. Rev. B 58, 10778 – 10783 (1998).
[63] M. Sasaki, N. Miyajima, H. Negishi, S. Negishi, M. Inoue, H. Kadomatsu, G. Machel, Possibility of quantum Hall effect in quasi-two-dimensional h-Mo4O11 crystal. Solid State Commun. 109, 357 – 362 (1999).
[64] H. Cao, J. Tian, I. Miotkowski, T. Shen, J. Hu, S. Qiao, Y. P. Chen, Quantized Hall effect and Shubnikov-de Haas oscillations in highly doped Bi2Se3: Evidence for layered transport of Bulk carriers. Phys. Rev. Lett. 108, 216803 (2012).
[65] S. Borisenko, D. Evtushinsky, Q. Gibson, A. Yaresko, T. Kim, M. N. Ali, B. Buechner, M. Hoesch, R. J. Cava, Time-reversal symmetry breaking Weyl state in YbMnBi2. arXiv:1507.04847 (2015).
[66] G. Lee, M. A. Farhan, J. S. Kim, J. H. Shim, Anisotropic Dirac electronic structures of AMnBi2 (A = Sr, Ca). Phys. Rev. B 87, 245104 (2013)
[67] T. Ando, A. B. Fowler, F. Stern, Electronic properties of two-dimensional systems. Rev. Mod. Phys. 54,437 – 672 (1982)
[68] V. Piazza, V. Pellegrini, F. Beltram, W. Wegscheider, T. Jungwirth, A. H. MacDonald, First-order phase transitions in a quantum Hall ferromagnet. Nature 402, 638 – 641 (1999).
[69] E. P. De Poortere, E. Tutuc, S. J. Papadakis, M. Shayegan, Resistance spikes at transitions between quantum hall ferromagnets. Science 290, 1546 – 1549 (2000).
[70] H. Cho, J. B. Young, W. Kang, K. L. Campman, A. C. Gossard, M. Bichler, W. Wegscheider, Hysteresis and spin transitions in the fractional quantum hall effect. Phys. Rev. Lett. 81, 2522 – 2525 (1998).

[71] J. Eom, H. Cho, W. Kang, K. L. Campman, A. C. Gossard, M. Bichler, W. Wegscheider, Quantum hall ferromagnetism in a two-dimensional electron system. Science 289, 2320 – 2323 (2000).
[72] T. Jungwirth, S. P. Shukla, L. Smr č ka, M. Shayegan, A. H. MacDonald, Magnetic anisotropy in quantum hall ferromagnets. Phys. Rev. Lett. 81, 2328 – 2331 (1998).
[73] Y. J. Jo, J. Park, G. Lee, M. J. Eom, E. S. Choi, J. H. Shim, W.Kang, J. S. Kim, Valley-polarized interlayer conduction of anisotropic Dirac fermions in SrMnBi2. Phys. Rev. Lett. 113, 156602 (2014).
[74] Z. Zhu, A. Collaudin, B. Fauqu é , W. Kang, K. Behnia, Field-induced polarization of Dirac valleys in bismuth. Nat. Phys. 8,89 – 94 (2011).
[75] L. Li, J. G. Checkelsky, Y. S. Hor, C. Uher, A. F. Hebard, R. J. Cava, N. P. Ong, Phase transitions of Dirac electrons in bismuth. Science 321, 547 – 550 (2008).
[76] S. Nandi, A. Kreyssig, Y. Lee, Y. Singh, J. W. Kim, D. C. Johnston, B. N. Harmon, A. I. Goldman, Magnetic ordering in EuRh2As2 studied by x-ray resonant magnetic scattering. Phys. Rev. B 79, 100407(R) (2009).
[77] J. P. Hannon, G. T. Trammell, M. Blume, D. Gibbs, X-ray resonance exchange scattering. Phys. Rev. Lett. 61, 1245 – 1248 (1988).
[78] W. W. Krempa, G. Chen, Y. B. Kim, and L. Balents, Annual Review of Condensed Matter Physics **5**, 57 (2014).
[79] H. Yang, Y. Sun, Y. Zhang, W.-J. Shi, S. S. P. Parkin, and B. Yan, New Journal of Physics **19**, 015008 (2017).
[80] K. Kuroda, T. Tomita, M.-T. Suzuki, C. Bareille, A. A. Nugroho, P. Goswami, M. Ochi, M. Ikhlas, M. Nakayama, S. Akebi, R. Noguchi, R. Ishii, N. Inami, K. Ono, H. Kumigashira, A. Varykhalov, T. Muro, T. Koretsune, R. Arita, S. Shin, T. Kondo, and S. Nakatsuji, Nature Materials **16**, 1090 (2017).
[81] M. Hirschberger, S. Kushwaha, Z. Wang, Q. Gibson, S. Liang, C. A. Belvin, B. A. Bernevig, R. J. Cava, and N. P. Ong, Nature Materials **15**, 1161 (2016).
[82] T. Suzuki, R. Chisnell, A. Devarakonda, Y.-T. Liu, W. Feng, D. Xiao, J. W. Lynn, and J. G. Checkelsky, Nature Physics **12**, 1119 (2016).
[83] K. S. Takahashi, H. Ishizuka, T. Murata, Q. Y. Wang, Y. Tokura, N. Nagaosa, and M. Kawasaki, Science Advances **4**, eaar7880 (2018).
[84] S. Nakatsuji, N. Kiyohara, and T. Higo, Nature **527**, 212 (2015).
[85] H. Sagayama, D. Uematsu, T. Arima, K. Sugimoto, J. J. Ishikawa, E. O' Farrell, and S. Nakatsuji, Physical Review B **87**, 100403 (2013).
[86] S. M. Disseler, Physical Review B **89**, 140413 (2014).
[87] C. Donnerer, M. C. Rahn, M. M. Sala, J. G. Vale, D. Pincini, J. Strempfer, M. Krisch, D. Prabhakaran, A. T. Boothroyd, and D. F. McMorrow, Physical Review Letters **117**, 1 (2016).
[88] H. Guo, C. Ritter, and A. C. Komarek, Physical Review B **94**, 1 (2016).
[89] S. Tomiyoshi and Y. Yamaguchi, Journal of the Physical Society of Japan **51**,

2478 (1982).
[90] P. J. Brown, V. Nunez, F. Tasset, J. B. Forsyth, and P. Radhakrishna, Journal of Physics: Condensed Matter **2**, 9409 (1990).
[91] S. Khmelevskyi, Physical Review B **86**, 104429 (2012).
[92] T. R. McGuire, M. W. Shafer, R. J. Joenk, H. A. Alperin, and S. J. Pickart, Journal of Applied Physics **37**, 981 (1966).
[93] P. C. Canfield, I. R. Fisher, Journal of Crystal Growth **225**, 155 – 161 (2001).
[94] H. Masuda, H. Sakai, M. Tokunaga, M. Ochi, H. Takahashi, K. Akiba, A. Miyake, K. Kuroki, Y. Tokura, and S. Ishiwata, Physical Review B **98**, 161108 (2018).
[95] F. F. Fang and P. J. Stiles, Physical Review **174**, 823 (1968).
[96] K.Vakili, Y. P. Shkolnikov, E. Tutuc, E. P. De Poortere, and M. Shayegan, Physical Review Letters **92**, 226401 (2004).
[97] A. Tsukazaki, A. Ohtomo, M. Kawasaki, S. Akasaka, H. Yuji, K. Tamura, K. Nakahara, T. Tanabe, A. Kamisawa, T. Gokmen, J. Shabani, and M. Shayegan, Physical Review B, **78**, 233308 (2008).
[98] C. Bergemann, A. P. Mackenzie, S. R. Julian, D. Forsythe, and E. Ohmichi, Advances in Physics **52**, 639 (2003).
[99] Jun Xiong, Yongkang Luo, YueHaw Khoo, Shuang Jia, R. J. Cava, and N. P. Ong, Physical Review B **86**, 045314 (2012).
[100] J. P. Perdew, K. Burke, and M. Ernzerhof, Physical Review Letters **77**, 3865 (1996).
[101] G. Kresse and D. Joubert, Physical Review B **59**, 1758 (1999).
[102] G. Kresse and J. Hafner, Physical Review B **47**, 558(R) (1993).
[103] G. Kresse and J. Hafner, Physical Review B **49**, 14251 (1994).
[104] G. Kresse and J. Furthmüller, Computational Materials Science **6**, 15 (1996).
[105] G. Kresse and J. Furthmüller, Physical Review B **54**, 11169 (1996).
[106] A. I. Liechtenstein, V. I. Anisimov, and J. Zaanen, Physical Review B **52**, R5467(R) (1995).
[107] S. L. Dudarev, G. A. Botton, S. Y. Savrasov, C. J. Humphreys, and A. P. Sutton, Physical Review B **57**, 1505 (1998).
[108] L.-L. Jia, Z.-H. Liu, Y.-P. Cai, T. Qian, X.-P. Wang, H. Miao, P. Richard, Y.-G. Zhao, Y. Li, D.-M. Wang, J.-B. He, M. Shi, G.-F. Chen, H. Ding, and S.-C. Wang, Physical Review B **90**, 035133 (2014).
[109] N. Marzari and D. Vanderbilt, Phys. Rev. B **56**, 12847 (1997).
[110] I. Souza, N. Marzari, and D. Vanderbilt, Phys. Rev. B **65**, 035109 (2001).
[111] J. Kuneš, R. Arita, P. Wissgott, A. Toschi, H. Ikeda, and K. Held, Comp. Phys. Commun. **181**, 1888 (2010).
[112] A. A. Mostofi, J. R. Yates, Y.-S. Lee, I. Souza, D. Vanderbilt, and N. Marzari, Comput. Phys. Commun. **178**, 685 (2008).
[113] 増田英俊, 卒業論文 (2014)
[114] D. Shoenberg: Cambridge University Press, Magnetic Oscillations in metals

[115] O. Vafek, A. Vishwanath, Annu. Rev. Condens. Matter Phys. **5**, 83 (2014).
[116] N. P. Armitage, E. J. Mele, and A. Vishwanath, Rev. Mod. Phys. **90**, 015001 (2018).
[117] L. Šmejkal, T. Jungwirth, and J. Sinova, Phys. Status Solidi RRL **11**, 1700044 (2017).
[118] L. Šmejkal, Y. Mokrousov, B. Yan, and A. H. MacDonald, Nat. Phys. **14**, 242 (2018).
[119] A. K. Nayak, J. E Fischer, Y. Sun, B. Yan, J. Karel, A. C. Komarek, C. Shekhar, N. Kumar, W. Schnelle, J. Kubler, C. Felser, and S. S. P. Parkin, Sci. Adv. **2**, e1501870 (2016). and J. G. Checkelsky, Nat. Phys. **12**, 1119 (2016).
[120] W. W.-Krempa, G. Chen, Y. B. Kim, and L. Balents: Annu. Rev. Condens. Matter Phys. **5** (2014) 57.
[121] K. Wang, D. Graf, H. Lei, S. W. Tozer, and C. Petrovic, Phys. Rev. B **84**, 220401(R) (2011).
[122] L.-L. Jia, Z.-H. Liu, Y.-P. Cai, T. Qian, X.-P. Wang, H. Miao, P. Richard, Y.-G. Zhao, Y. Li, D.-M. Wang, J.-B. He, M. Shi, G.-F. Chen, H. Ding, and S.-C. Wang, Phys. Rev. B **90**, 035133 (2014).
[123] L. Li, K. Wang, D. Graf, L. Wang, A. Wang, and C. Petrovic, Phys. Rev. B **93**, 115141 (2016).
[124] Y. Y. Wang, Q. H. Yu and T. L. Xia, Chinese Phys. B **25**, 107503 (2016).
[125] A. Wang, I. Zaliznyak, W. Ren, L. Wu, D. Graf, V. O. Garlea, J. B. Warren, E. Bozin, Yimei Zhu, and C. Petrovic, Phys. Rev. B **94**, 165161 (2016).
[126] S. Borisenko, D. Evtushinsky, Q. Gibson, A. Yaresko, T. Kim, M. N. Ali, B. Buechner, M. Hoesch, and R. J. Cava, arXiv: 1507.04847 (2015)
[127] J. Y. Liu, J. Hu, Q. Zhang, D. Graf, H. B. Cao, S. M. A. Radmanesh, D. J. Adams, Y. L. Zhu, G. F. Cheng, X. Liu, W. A. Phelan, J. Wei, M. Jaime, F. Balakirev, D. A. Tennant, J. F. DiTusa, I. Chiorescu, L. Spinu, and Z. Q. Mao, Nat. Mater. **16**, 905 (2017).
[128] J. Liu, J. Hu, H. Cao, Y. Zhu, A. Chuang, D. Graf, D. J. Adams, S. M. A. Radmanesh, L. Spinu, I. Chiorescu, and Z. Mao, Sci. Rep. **6**, 30525 (2015).
[129] S. Huang, J. Kim, W. A. Shelton, E. W. Plummer, and R. Jin, Proc. Natl. Acad. Sci. USA, **114**, 6256 (2017).
[130] M. A.Farhan, G. Lee, and J. H. Shim, J. Phys.: Condens. Matter **26**, 042201 (2014).
[131] F. J. Teran, M. Potemski, D. K. Maude, T. Andrearczyk, J. Jaroszynski, and G. Karczewski, Phys. Rev. Lett. **88**, 186803 (2002).
[132] Y. Zhang, Z. Jiang, J. P. Small, M. S. Purewal, Y.-W. Tan, M. Fazlollahi, J. D. Chudow, J. A. Jaszczak, H. L. Stormer, and P. Kim, Phys. Rev. Lett. **96**, 136806 (2006).
[133] A. F. Young, C. R. Dean, L. Wang, H. Ren, P. Cadden-Zimansky, K. Watanabe, T. Taniguchi, J. Hone, K. L. Shepard and P. Kim, Nat. Phys. **8**, 550 (2012).
[134] S. Jeon, B. B. Zhou, A. Gyenis, B. E. Feldman, I. Kimchi, A. C. Potter, Q.

D. Gibson, R. J. Cava, A. Vishwanath and A. Yazdani, Nat. Mater. **13**, 851 (2014).

[135] Z. J. Xiang, D. Zhao, Z. Jin, C. Shang, L. K. Ma, G. J. Ye, B. Lei, T. Wu, Z. C. Xia, and X. H. Chen, Phys. Rev. Lett. **115**, 226401 (2015).

[136] Y. Liu, X. Yuan, C. Zhang, Z. Jin, A. Narayan, C. Luo, Z. Chen, L. Yang, J. Zou, X. Wu, S. Sanvito, Z. Xia, L. Li, Z. Wang and F. Xiu, Nat. Commun. **7**, 12516 (2016).

[137] D. P. Druist, P. J. Turley, K. D. Maranowski, E. G. Gwinn, and A. C. Gossard, Phys. Rev. Lett. **80**, 365 (1998).

[138] M. Kawamura, A. Endo, S. Katsumoto, Y. Iye, C. Terakura, and S. Uji, Physica B **298**, 48 (2001).

Acknowledgement

I would like to thank Prof. Shintaro Ishiwata for frequent discussions, valuable comments and kind encouragement through the course of writing the present thesis.

The valuable comments from Prof. Kazushi Kanoda, Prof. Masashi Kawasaki, Prof. Masashi Tokunaga, and Prof. Kyoko Ishizaka are gratefully acknowledged.

I am grateful to Hideaki Sakai and Hidefumi Takahashi for fruitful discussions and experimental supports. I also thank all the other members in Ishiwata Lab. for encouragement.

I would like to thank for the collaborative research and discussions: Prof. H. Sakai, Prof. M. Tokunaga, Dr. Y. Yamasaki, Dr. A. Miyake, Dr. J. Shiogai, Prof. S. Nakamura, Prof. S. Awaji, Prof. A. Tsukazaki, Prof. H. Nakao, Prof. Y. Murakami, Prof. T. Arima, Prof. Y. Tokura and Prof. S. Ishiwata for the work described in Chap.4; Prof. H. Sakai, Dr. H. Takahashi, Dr. Y. Yamasaki, Dr. A. Nakao, Dr. T. Moyoshi, Prof. H. Nakao, Prof. Y. Murakami, Prof. T. Arima, and Prof. S. Ishiwata for the work described in Chap. 5.1; Prof. H. Sakai, Prof. M. Tokunaga, Dr. M. Ochi, Dr. H. Takahashi, Dr. K. Akiba, Dr. A. Miyake, Prof. K. Kuroki, Prof. Y. Tokura, and Prof. S. Ishiwata for the work described in Chaps. 5.2 and 6.

I am grateful to the financial supports provided by MERIT and JSPS.

Lastly, I would like to express special gratitude to my families for their support and encouragement for years.